

**INSTITUT FÜR
ENERGIETECHNIK UND
THERMODYNAMIK**
Institute for Energy Systems and Thermodynamics

Master Thesis

Effect of burner design on characterisation of pulverised biomass flame

A thesis submitted for the degree of Master of Science

under supervision of
Ao.Univ.Prof. Dipl.-Ing. Dr.techn. Andreas Werner

at the Vienna University of Technology,
Faculty of Mechanical and Industrial Engineering

by

Clemens Antretter
e1022771
Purtschellergasse 11
5020 Salzburg

Abstract

In order to handle the ever increasing demand of energy and reduce the dependence on fossil fuels, biomass represents a possible alternative and has been classed as renewable energy source by the European Union and the United Nations. This thesis investigates the influence of different burner designs on characteristics of pulverised biomass flame and more precisely, the impact of swirling motion created by a swirler inlet on the flow field in the combustion chamber. The velocity flow field has been determined for three swirl settings with two different methods: Particle Image Velocimetry (PIV) and Computational Fluid Dynamics (CFD). No-, half- and full-swirl setup were investigated for both methods with further four different velocity ratios as part of the PIV experiment. The experiment was conducted in the university's laboratory and validation shows a maximal deviation of 6% between each run. Issues faced during the experiment and potential improvements (e.g. different seeding particles or recording settings) are stated in the thesis. The velocity fields for the no- and half-swirl setups show reasonable and replicable results, but the full-swirl setup resulted in spurious vector fields. This was caused by exceedingly fast dispersion of the particles, a very fast shift from axial movement to radial movement and consequently, an out-of plane movement of particles out-of the laser sheet.

The CFD simulation of the biomass burner was modelled and simulated using the software ANSYS - Fluent. Validation of the mesh shows very good to perfect mesh elements and result validation confirm reasonable results. The length of the resulting velocity fields shows a strong dependence on the swirl-setting as well as the change in radial movement becomes evident. The comparison between PIV and CFD shows very good convergence of the velocity for the first 2-10cm after the outlet. Afterwards, the velocity values of both methods diverge with considerably faster convergence to lower values for the PIV experiment.

Acknowledgements

Firstly, I would like to express my gratitude to my supervisor Werner Andreas at the Vienna University of Technology for his support and guidance.

Most parts of this thesis have been completed through the work done at the Laboratory of energy conversion processes (ECO-lab) at Luleå University of Technology during my stay as an exchange student. I would like to express my special thanks to Kentaro Umeki of the Division of Energy Sciences for giving me the opportunity to work on this project as well as for his constant supervision, the valuable contributions and also the support in completing this thesis.

I owe special gratitude to Lu Ding who not only worked with me on the experiment but also for our special friendship during the time we spent in the laboratory.

To my fellow students Clemens Oppeneiger, Matthias Kowatsch, Lukas Zehentner, Valentin Unger, Christian Ortbauer and Philipp Schröckmair for their support during the study and making my life enjoyable in Vienna.

Finally, I express my profound gratitude to my family for their continuous support and encouragement throughout my years of study. This accomplishment would not have been possible without them.

Contents

1	Introduction	1
2	Objective	2
3	Theory	3
3.1	Flame Stability due to swirling motion	3
3.2	Computational Fluid Dynamics (CFD)	6
3.2.1	Turbulence modelling	6
3.2.2	The k- ϵ Model	8
3.3	Particle Image Velocimetry (PIV)	12
3.3.1	General Setup of a PIV System	12
3.3.2	Particle Properties and Seeding	13
3.3.3	Cross-Correlation	15
4	Method	16
4.1	Calculation of Swirl Number	16
4.2	Flow Rate Calculation	20
4.3	CFD Simulation Procedure	22
4.3.1	Meshing	24
4.3.1.1	Mesh Validation	26
4.3.2	Simulation Setup	28
4.3.3	Result Validation	29
4.3.3.1	Residual Convergence	29
4.3.3.2	Monitoring Points	30
4.3.3.3	Grid Independence Study	32
4.4	PIV Experiment	34
4.4.1	Setup	34
4.4.1.1	Smoke Seeding	35
4.4.1.2	Camera	35
4.4.1.3	Laser	36
4.4.2	Procedure	37
4.4.2.1	Calibration	38
4.4.2.2	Acquisition	40
4.4.2.3	Analysis Sequence	42
4.4.3	Validation	43
5	Results	45
5.1	CFD Results	45
5.1.1	Velocity Fields	45
5.1.2	Radial Velocity	46
5.2	PIV Results	51
5.2.1	No Swirl	51

5.2.2	Half Swirl	58
5.2.3	Full Swirl	63
5.3	Comparison of CFD and PIV Results	67
6	Conclusion	70
7	References	72
8	List of Figures	75
9	List of Tables	76

1 Introduction

The growing awareness for climate change and rising energy demand as two of the most important challenges facing the world in the 21st century call for research on affordable, clean and renewable energy sources. The Renewable Energy Directive established by the European Union sets a binding target of 20% final energy consumption from renewable sources by 2020. In order to achieve this EU countries committed to reaching their own national renewables targets ranging from 10% in Malta to 49% in Sweden [1]. One such alternative is the use of bio-based fuels instead of fossil fuels as the balance between emitting and extracting CO_2 from the atmosphere can be equilibrated. Biomass is derived from organic material such as trees, plants, and agricultural and urban waste. Particularly woody biomass can be used in different ways to generate heat and/or electricity. Wood can be used as a fuel for direct combustion in a wood fired burner or as a fuel to pyrolyse it to combustible pyrolysis oil. A third way of using wood as fuel is gasification, i.e. wood is gasified into syngas which in the end replaces natural gas [2].

As part of the project 'NoFo ungare forskare' currently conducted at the Division of Energy Science, Luleå University of Technology, a new technique is under development with the aim of reducing emission (e.g. soot, NO_x) from pulverised biomass burners by forcing particle dispersion with flow manipulation technique. Previous findings so far revealed that particle interactions do affect tar and soot formation which can be reduced by forced particle dispersion. An important goal of this project is the use of a combination of advanced optical methods and numerical modelling in order to improve the understanding of effects of flow manipulation technique on flame dynamics and particle conversion. Scaled-up results are often not straight-forward and before conducting the experiment in the 30kW flame reactor in the university's laboratory another step of development is necessary for scale-up. Hence, experiments will be performed in a glass chamber with and without flow manipulation under cold flow conditions.

2 Objective

The aim of this thesis is to investigate how different burner designs affect characteristics of pulverised biomass flame with a special focus on gas and particle flow fields. In corporation with a post-doctoral researcher my task was the operation of a time-resolved PIV (particle image-velocimetry) experiment in order to measure velocity fields of cold flows; and in more exact terms, the response of the flow field to the change of flow parameters, especially swirling motion of the flow based on different burner designs, and various flow rates. Experiments were carried out in a glass chamber with three different swirl settings and four flow ratios. Cold flow conditions were applied to avoid the difficulties associated with actual burner testing (e.g. reaction, interference from wall radiation, soot, and gas; change in optical pathway at high temperature), and to extract the information of gas and particle flows without reactions. The PIV experiment had three major tasks:

- To construct, assemble and establish a laboratory experiment
- To learn how to operate and perform a PIV technique
- To carry out PIV using smoke particle-laden flow for different burner designs and flow parameters

During the experiment it was decided to also numerically simulate the experiment using Computational Fluid Dynamics - CFD. This was mainly done because of unexpected delays of the PIV experimental setup. Nevertheless, the objective to study the influence of the swirling motion caused by different burner designs stayed the same and a comparison of PIV and CFD results was performed.

This thesis represents the very early stage of an overall project to understand flow manipulation on pulverised biomass burners. Therefore, another aim is to provide a first understanding, aid and information for further PIV experiments and the following steps of this project.

3 Theory

3.1 Flame Stability due to swirling motion

Swirl-stabilised combustion is widely used in many different combustion applications, including gas turbines, burners, and even internal combustion engines. A spiral motion of the flow in tangential direction in addition to its axial and radial direction is commonly regarded as a swirling flow. Subsequently, the swirl flow can influence all the downstream processes in the combustion chamber in a direct manner and therefore provide an aerodynamic mechanism for flow field manipulation and flow control. There are three factors known to add a swirling motion to a flow[3]:

- Rotating mechanical devices
- Use of turning vanes
- Tangential plus radial entry of fluid stream

Generally, almost all these systems share the same two main goals of a swirling flow: Firstly, stabilisation of the flame in the combustion chamber, and secondly, improvement fuel-air mixing behaviour. Both these goals are mainly achieved by formation of recirculation zones and high rates of entrainment. [3, 4]

In order to compare the magnitude of the swirling motion different studies use various approaches, e.g. the angle of turning vanes. However, the extent of the swirl is most commonly characterised by the dimensionless swirl number S . It represents axial flux of swirl momentum divided by the product of the axial flux of axial momentum and the nozzle equivalent radius:

$$S = \frac{G_{\Theta}}{RG_z} = \frac{\int_0^{\infty} \rho u_z u_{\theta} r^2 dr}{R \int_0^{\infty} [\rho u^2 + (\rho - \rho_{\infty})] r dr} \quad (1)$$

with u_z the axial and u_{θ} the azimuthal velocity components. $\rho - \rho_{\infty}$ indicates the pressure difference between the swirling flow and the fluid with no motion. The pressure term is in most cases usually too small to measure and therefore, the swirl number is generally expressed without it. By neglecting this term it is possible to define the function of the swirl number with only the swirler geometry [5]. The Swirl Number for the swirler used in the experiment will be calculated in chapter 4.1.

The effect of the swirl on the flow field generated by these systems is determined by many factors, such as the quantity and exit velocity of the swirling air, swirler and nozzle geometry as well as the size of the combustion chamber. Despite all these factors, it is possible to show typical characteristic flow features that most swirling systems have in common. Figure 1 is the result of an experiment performed with an atomised fuel spray flame sandwiched in two co-swirling air streams [6]. It shows precisely the characteristic flow pattern in the combustion chamber for a dual swirl injector, although it is a special

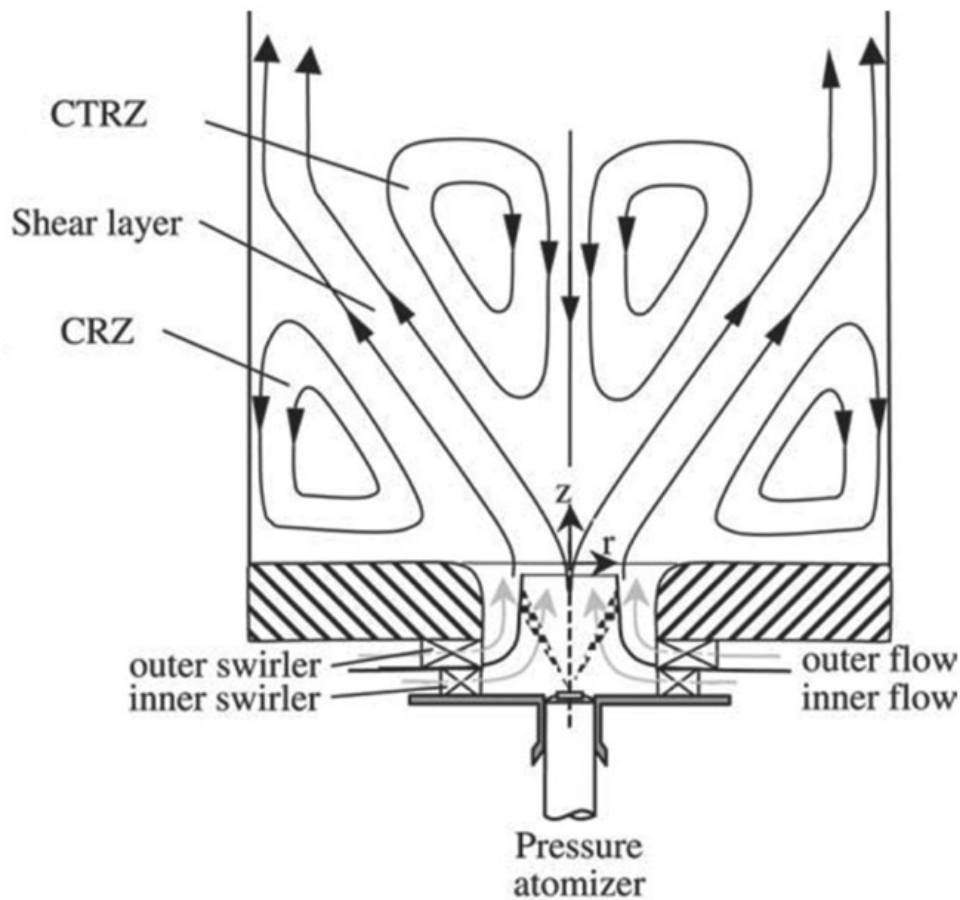


Figure 1: Characteristic flow pattern in a combustion chamber for dual swirl injector [6]

application, it displays the streamlines and flow pattern which can be expected in most swirling air combustion systems. Not just the swirler design but also the flow field can vary from the figure and show different shapes depending on the swirling intensity, Reynolds number and combustion chamber geometry. In order to achieve high swirling intensity, a central toroidal recirculation zone (CTRZ) is generated downstream. Also called vortex breakdown bubble it refers to a disturbance characterised by the formation of an internal stagnation point on the vortex axis, followed by reversed flow in a region of limited axial extent [7]. Surrounding the bubble is a three-dimensional spiral flow pattern. This recirculation zone RZ can be quite compact and an averaged long time view shows an almost fixed position. The position of the CTRZ results in a significantly shorter flame length compared to a non-swirl inlet. The compact flame usually does not even touch the surface of the combustion chamber which leads to longer lifetime and reduced maintenance of the burner. The swirling motion plays an important role in the complete combustion of the fuel, too. The recirculation also provides a constant heat source due to the burnt products. Furthermore, the rate of entrainment is higher compared to a straight-line jet.

Depending on the swirl intensity and the geometry of nozzle and combustion chamber, corner recirculation zones (CRZ) can occur in the flow field. This effect is not so important for engineers as it has less impact on the flame stabilisation. In between these two recirculation zones exist shear layers, which together with the shear stress inside the RZs, decrease the velocity to balance flame speed and flow velocity. [G“**IeC** –“”o”ktepe15, 8, 9]

The studies [10, 11] investigate the effect of flame stability and entrainment on emissions due to swirling motion. [10] shows the decrease of NOx emissions when increasing the swirl number in the burner. The NOx was measured at $S=0.05$, $S=1.5$ and $S=1.9$ and an equivalence ration of 0.83. A reduction of 26% was obtained at $S=1.5$ compared to $S=0.05$. This marked a turning point as further increase of the swirl number also led to higher NOx emissions. Therefore, it can be seen that swirling helps in mixing fuel an air to a certain degree. Afterwards, the higher vane angle causes more recirculation leading to a reduction in combustion stability. The carbon dioxide emissions decreased continuously for higher swirling numbers. A reduction in CO_2 of 11.7% was measured for $S=1.5$ compared to $S=0.05$.

3.2 Computational Fluid Dynamics (CFD)

Computational Fluid Dynamics, short CFD, is a synonym for numerical analysis of fluid flows. Like all problems in the classical mechanics, flows and their related phenomena can also be characterised by conservation laws. Mass, momentum and energy are mathematically described through partial differential equations and their boundary conditions. It is usually not possible to solve these equations analytically except for some special case exceptions. CFD programs are able to achieve an approximate solution numerically with the help of a discretization method. There are many different approaches to this method but the most common ones are the finite difference (FD), finite volume (FV) and the finite elements (FE) method. The preference is determined by the demands of the developer, i.e. ANSYS Fluent is based on a finite volume solver. The whole geometric domain in which the flow has to be solved, is divided into a high number of discrete cells, the so-called mesh. These cells can consist of tetrahedral, hexahedral, prismatic or pyramidal elements and approximations are made in these control volumes (CV). Integration of the governing equations on the discrete control volumes gives a system of algebraic, non-linear equations for the unknown variables, such as velocity or pressure. These systems of algebraic equations can then be numerically solved by a computer. As they are non-linear, many iterations which are repeated calculation of these procedures are used to increment the accuracy of the final solution. [12, 13]

3.2.1 Turbulence modelling

Most flows in nature and technical applications are turbulent and require a different approach than laminar flows. Turbulence can be any fluid motion characterised by seemingly random chaotic changes in flow velocity and pressure. Before introducing mathematics of turbulent flows it is justifiable to discuss a few physical aspects of this phenomenon.

- Turbulent flows are highly transient. A graphical illustration of the velocity over time would appear random to a viewer unfamiliar with these flows. That is why turbulence is usually treated statistically rather than deterministically.
- They have a high amount of vorticity and a strong three-dimensional vortex stretching. This stretching is one of the main mechanisms of turbulence intensity.
- Mixing and transfer of mass, momentum and energy can be described as turbulent diffusion. It does not have a true physical meaning but it is one of the most important aspects of turbulence from an engineering point of view.
- Turbulent flows dissipate rapidly. This is due to the kinetic energy transforming into internal energy by viscous shear stress.

Although these are only a few characteristics, it is important to show the complexity of turbulence. In order to approximate this complicated phenomenon with an appropriate model one can follow the spirit of Taylor, Prandtl and von Kármán: *'... an ideal model should introduce the minimum amount of complexity while capturing the essence of the*

relevant physics'. [13–15]

As already mentioned above, due to the random fluctuations of all the properties of the flow, it is common to use a statistical approach. To approximate the Navier-Stokes equations, we use the idea of decomposition, first introduced by Osborne Reynolds in 1895. For stationary turbulence the variables, in this case the instantaneous velocity $u_i(\mathbf{x}, t)$, can be expressed as the sum of a mean $\overline{u_i(\mathbf{x})}$ and a certain fluctuating part $u'_i(\mathbf{x}, t)$

$$u_i(\mathbf{x}, t) = \overline{u_i(\mathbf{x})} + u'_i(\mathbf{x}, t) \quad (2)$$

The averaging method takes the mean values at a certain place and averaged over a time period. This time period has to be large in contrast to the time span of the fluctuations.

$$\overline{u_i(\mathbf{x})} = \lim_{T \rightarrow \infty} \frac{1}{T} \int_0^T u_i(\mathbf{x}, t) dx \quad (3)$$

This decomposition can be analogously done for other variables and applied to the Navier-Stokes equations. The Navier-Stokes equations for an incompressible Newtonian Fluid follow as:

$$\frac{\partial u_i}{\partial t} + u_j \frac{\partial u_i}{\partial x_j} = f_i - \frac{1}{\rho} \frac{\partial p}{\partial x_i} + \nu \frac{\partial^2 u_i}{\partial^2 x_j} \quad (4)$$

with p the pressure, f_i a vector representing external forces, ρ the density and ν the kinematic viscosity. By splitting each instantaneous quantity into time-averaged and fluctuating parts, the resulting Reynolds-averaged Navier–Stokes equations, or RANS equations, follow as:

$$\frac{\partial \overline{u_i}}{\partial t} + \overline{u_j} \frac{\partial \overline{u_i}}{\partial x_j} = \overline{f_i} - \frac{1}{\rho} \frac{\partial \overline{p}}{\partial x_i} + \nu \frac{\partial^2 \overline{u_i}}{\partial^2 x_j} - \frac{\partial \overline{u'_i u'_j}}{\partial x_j} \quad (5)$$

Further manipulation and eliminating the time derivative due to integration in time removes the time dependence of the resultant terms, the equation yields:

$$\rho \overline{u_j} \frac{\partial \overline{u_i}}{\partial x_j} = \rho \overline{f_i} + \frac{\partial}{\partial x_j} (-\overline{p} \delta_{ij} + 2\mu \overline{S_{ij}} - \rho \overline{u'_i u'_j}) \quad (6)$$

where S_{ij} is the mean rate of strain tensor and the quantity $\overline{\rho u'_i u'_j}$ of the last term of equation (6) is commonly known as the Reynolds-stress tensor $\tau_{ij} = -\overline{\rho u'_i u'_j}$. This appearance of the Reynold stress is the reason which makes the turbulence problem so challenging. It represents an added stress on the fluid and describes the diffusive nature of turbulence. As this tensor τ_{ij} is symmetric, it has six independent components, and so it produces six more unknown variables as a result of Reynolds averaging. Beside the Reynolds-stresses, in a three-dimensional flow, there are also three velocity components u_i , viscosity μ and pressure p . That means in total 10 unknowns. The three components of the RANS equations and also the mass conservation bring in only a total of four equations. The system is therefore not closed. As the Navier-Stokes equations are non-linear, it is not possible to

balance the equations/unknown scale. The closure of the RANS-equations can be done by approximations of turbulence modelling. The role of these models is to approximate the unknown correlations based on known flow characteristics in order for enough numbers of equations to exist. [15, 16],

It is a good and proven assumption that the event of turbulence can be expressed due to increased viscosity. This is based on the fact that in laminar flows, energy dissipation and the transport of mass, momentum and energy across the streamlines are also regulated by viscosity. Using the Boussinesq approach, this eventually leads to the definition of the Reynolds stress:

$$\tau_{ij} = 2\mu_T S_{ij} - \frac{2}{3}\rho k \delta_{ij} \quad (7)$$

with μ_T the eddy-viscosity and k the turbulent kinetic energy defined as:

$$k = \frac{1}{2}\overline{u'_i u'_i} = \frac{1}{2}(\overline{u'^2} + \overline{v'^2} + \overline{w'^2}) \quad (8)$$

The turbulent kinetic energy k determines the energy in the turbulence. One way to model k is by deriving the eddy-viscosity, in such case, additional transport equations are required. The mechanism of transport in flows are convection (transport with the flow) and diffusion (transport through mixing). This is based on the perception that turbulence is produced in certain areas of the flow, transported to other areas and drained there by friction. One of the transport models which describes turbulent flows is the two-equation k - ϵ model. [17], [18]

3.2.2 The k - ϵ Model

Standard k - ϵ Model: The k - ϵ Model was first introduced in 1968 by Harlow and Nakayama. The equations include many unmeasurable and unknown terms, therefore, the paper [19] published by Launder and Spalding in 1974 is the more reasonable approach and often referred to as the standard k - ϵ Model. It is a robust, efficient, reasonable and hence one of the most common turbulence models. [20]

Two transport equations (PDEs) represent the turbulent properties of a flow.

The first transport variable is the turbulent kinetic energy k which is derived from the following transport equation:

$$\frac{\partial}{\partial t}(\rho k) + \frac{\partial}{\partial x_i}(\rho k u_i) = \frac{\partial}{\partial x_j}[(\mu + \frac{\mu_t}{\sigma_k})\frac{\partial k}{\partial x_j}] + G_k + G_b - \rho\epsilon - Y_M + S_k \quad (9)$$

The second transported variable is the rate of dissipation of turbulence energy ϵ , it determines the scale of the turbulence and can be derived from the following equation:

$$\frac{\partial}{\partial t}(\rho\epsilon) + \frac{\partial}{\partial x_i}(\rho\epsilon u_i) = \frac{\partial}{\partial x_j}[(\mu + \frac{\mu_t}{\sigma_\epsilon})\frac{\partial \epsilon}{\partial x_j}] + C_{1\epsilon}\frac{\epsilon}{k}(G_k + C_{3\epsilon}G_b) - C_{2\epsilon}\rho\frac{\epsilon^2}{k} + S_\epsilon \quad (10)$$

In these equations u_i represents the velocity components in the corresponding directions. G_k stands for the production of turbulent energy due to mean velocity gradients and is defined as:

$$G_k = -\overline{\rho u'_i u'_j} \frac{\partial u_j}{\partial x_i} \quad (11)$$

G_b is the generation of turbulent kinetic energy which arises due to buoyancy and Y_M represents compressibility effects in turbulence flows through dilation dissipation. S_k and S_ϵ are user defined terms. The constants $C_{1\epsilon}$, $C_{2\epsilon}$ and C_μ and the turbulent Prandtl numbers for k and ϵ , σ_k and σ_ϵ , have been determined experimentally for fundamental turbulent flows and are defined as follows:

$$\begin{aligned} C_{1\epsilon} &= 1.44 \\ C_{2\epsilon} &= 1.92 \\ C_\mu &= 0.09 \\ \sigma_k &= 1.0 \\ \sigma_\epsilon &= 1.3 \end{aligned}$$

The turbulent viscosity is computed by combining the turbulent kinetic energy with the dissipation rate:

$$\mu_t = \rho C_\mu \frac{k^2}{\epsilon} \quad (12)$$

with C_μ being the same constant as defined above.

Therefore, the physical meaning of the terms in the equations (9) and (10) can be seen as:

$$\begin{aligned} & \text{Rate of change of } k \text{ or } \epsilon + \text{Transport of } k \text{ or } \epsilon \text{ by convection} \\ &= \text{Transport of } k \text{ or } \epsilon \text{ by diffusion} + \text{Rate of production by } k \text{ or } \epsilon \\ & \quad - \text{Rate of destruction of } k \text{ or } \epsilon \end{aligned}$$

The standard k- ϵ model is the most commonly used turbulence model for a wide range of applications in CFD. Although it delivers good results and predictions for many flows, it can be considered the simplest turbulence model. The standard k- ϵ model is inappropriate for more complex problems and performs poorly for applications such as:

- Flows with boundary layer separation
- Flows over curved surfaces
- Unconfined flows
- Flows with sudden changes in the mean strain rate
- Flows in rotating fluids

For these reasons the realizable k- ϵ model was introduced as it differs from the standard model and brings superior ability in solving turbulent flows of more complex structures. [17]

Realizable k- ϵ Model: The realizable k- ϵ model developed by Shih et al [Paper einfügen [shih 1995]] has two major changes compared to the standard k- ϵ model:

- Alternative formula for the turbulent viscosity μ_t
- Modified transport equation for the dissipation rate ϵ , derived from the dynamic equation of the mean-square vorticity fluctuation.

The transport equation for the turbulent kinetic energy k of the realizable k- ϵ model stays the same as in the standard model, except for some model constants:

$$\frac{\partial}{\partial t}(\rho k) + \frac{\partial}{\partial x_j}(\rho k u_j) = \frac{\partial}{\partial x_j}[(\mu + \frac{\mu_t}{\sigma_k}) \frac{\partial k}{\partial x_j}] + G_k + G_b - \rho \epsilon - Y_M + S_k \quad (13)$$

However, the equation for the rate of dissipation ϵ changes a lot in comparison to the standard model. Especially the production term of ϵ , the second term on the right side of the equation (14), does not involve the production of k , in this case G_k .

$$\begin{aligned} \frac{\partial}{\partial t}(\rho \epsilon) + \frac{\partial}{\partial x_j}(\rho \epsilon u_j) = \\ \frac{\partial}{\partial x_j}[(\mu + \frac{\mu_t}{\sigma_\epsilon}) \frac{\partial \epsilon}{\partial x_j}] + \rho C_1 S \epsilon - \rho C_2 \frac{\epsilon^2}{k + \sqrt{\nu \epsilon}} + C_1 \frac{\epsilon}{k} C_{3\epsilon} G_b + S_\epsilon \end{aligned} \quad (14)$$

where C_1 is defined by the form:

$$C_1 = \max[0.43, \frac{\eta}{\eta} + 5], \eta = S \frac{k}{\epsilon} \quad (15)$$

with S the modulus of the mean rate-of-strain tensor:

$$S \equiv \sqrt{2 S_{ij} S_{ij}} \quad (16)$$

The second major change of the realizable model is that C_μ of the turbulent viscosity

$$\mu_t = \rho C_\mu \frac{k^2}{\epsilon} \quad (17)$$

is no longer constant and computed by the relation:

$$C_\mu = \frac{\epsilon}{A_0 \epsilon + A_s k S} \quad (18)$$

With the constants defined as:

$$A_0 = 4.04 \quad (19)$$

$$A_s = 6^{1/2} \cos \Theta \quad (20)$$

$$\Theta = (1/3) \cos^{-1}(6^{1/2} S^2) \quad (21)$$

The other constants are set as followed and defined to perform well for different turbulent flows:

$$\begin{aligned}C_{1\epsilon} &= 1.44 \\C_{2\epsilon} &= 1.9 \\ \sigma_k &= 1.0 \\ \sigma_\epsilon &= 1.2\end{aligned}$$

The realizable k - ϵ model modifies the dissipation rate ϵ and thus improves one of the weaknesses of the standard k - ϵ model. Additionally, the important coefficient C_μ in the turbulent viscosity equation is not assumed to be constant. Instead it is dependant on the mean rotation and turbulent properties. These improvements make the model more consistent with the physics of turbulent flows and superior for a wide range of flows, including flows involving rotation, channel and boundary layers, free flows including jets and recirculation. [21, 22]

3.3 Particle Image Velocimetry (PIV)

Particle Image Velocimetry (PIV) is a measuring technique for flow visualisation providing instantaneous velocity vectors. Trace particles are added to the flow and illuminated at least twice between a short time interval Δt . The light scattered by the particles is recorded on a frame to determine the displacement. Consequently, the distance covered by the particle Δx and the time interval Δt gives the velocity.

3.3.1 General Setup of a PIV System

Figure 2 shows a general and simplified setup for a PIV system. In most applications lasers are predominant for illuminating the particles due to their high power light beams at a short pulse duration. Specialised, high repetition rate lasers, specifically designed for PIV are used as they also provide a steady beam profile and stability. A light sheet optic inside the laser produces a planar light sheet to illuminate the particles. Then, a high-quality camera records the light scattered by the particles at two different times and the output is transferred to a computer. The recording is usually divided into small subareas called “interrogation areas”. Following this, the displacement vector of the particles in each of these small areas is determined using statistical methods. It is estimated that all particles within one interrogation area have moved homogeneously during this time interval. With these values the velocity vector for the flow can be calculated. [23]

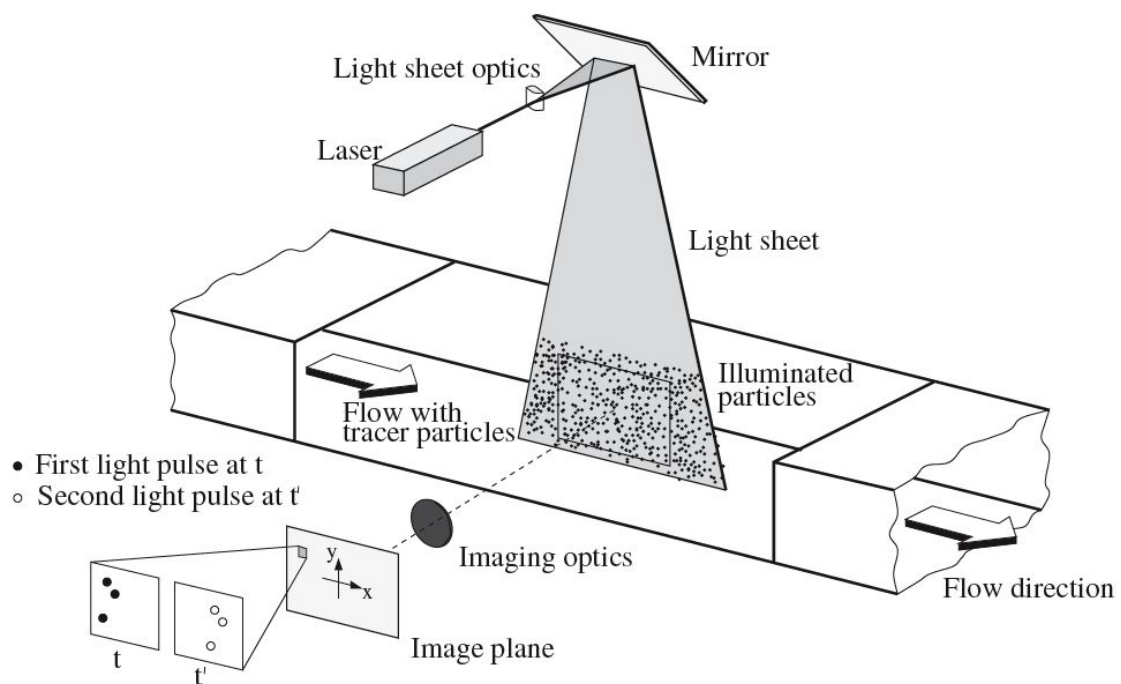


Figure 2: Experimental arrangement for a typical PIV system [23]

3.3.2 Particle Properties and Seeding

As the PIV is only measuring the tracer particle velocity instead of the fluid velocity, the fluid mechanical properties of the particles need to be examined. For instance, particles that are too big can change the original flow and cause for velocity lags. On the other hand, particles that are too small - especially in gaseous fluids - require a high-power light source in order to be illuminated enough to then record the scattered light. Therefore, it is important to find an acceptable compromise for each application.

One major source of error is the difference between the density of the tracer particles ρ_P and the fluid ρ due to the influence of gravity. Considering the Stokes Law - an expression for small - spherical objects in a viscous fluid, it is possible to derive the gravitationally induced velocity lag for a particle in a continuously accelerating fluid.

$$\mathbf{U}_s = \mathbf{U}_P - \mathbf{U} = d_p^2 \frac{\rho_P - \rho}{18\mu} \quad (22)$$

If the density of the tracer particle is much bigger than the fluid density, the step response of U_p follows an exponential law:

$$U_P(t) = U(1 - \exp(-\frac{t}{\tau_s})) \quad (23)$$

with the relaxation time τ_s :

$$\tau_s = d_p^2 \frac{\rho_P}{18\mu} \quad (24)$$

In order to accelerate fluids or high flow velocities, the Stokes Law does not apply anymore, and the particle motion equations are no longer a simple exponential function. Nevertheless, τ_s gives a good proximity if the particles attain velocity equilibrium with the fluid. Figure 3 shows the time response of oil particles with different diameters in a decelerating air flow. Bigger particles lead to a higher velocity lag. It also displays the fact that particles beyond the size of $1\mu\text{m}$ do not make much sense. This evidence was also confirmed when calculating a theoretical approach, considering compressibility, deformation and high Reynolds numbers. [4, 23]

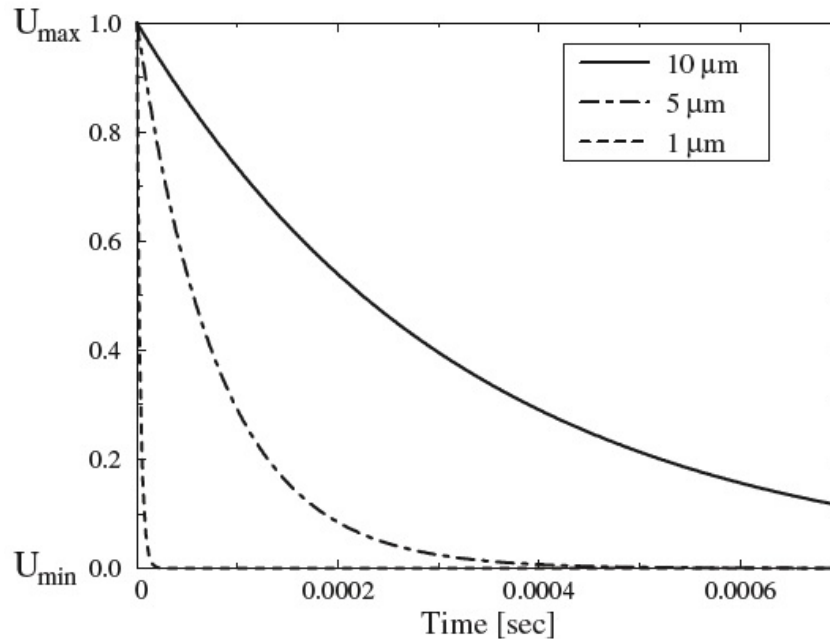


Figure 3: Time response of oil particles with different diameters [23]

Seeding of liquids is usually very easy in comparison to seeding of gases, sometimes it is not even necessary. For most liquid flows it is enough to suspend solid particles into the fluid and mixing them to achieve homogeneous distributions. Different oils, hollow glass spheres or aluminium flakes are the most common tracer particles for liquid flows. Seeding of gases is more complex and health risks must be taken into considerations. For instance, experimentalists may inhale the harmful seeded air in open test sections. For most of the PIV experiments in air flows oil droplets have been used. However, in cases where the stability of the tracer particles is not guaranteed (e.g. increased temperatures, reactive environments) droplet-based seeding is no longer possible. Metal oxide powders, such as aluminium oxide or titanium dioxide, show high melting points, and inertness at low cost. Yet these particles for gaseous fluids tend to agglomerate and are hard to disperse. A common approach is the use of a fluidised bed seeding device to de-agglomerate and to ensure homogenous distribution of the particles with the gas. However, the main issue of solid particles is the difference in density, which can lead to a velocity lag. Therefore, smoke particles are sufficient for most air flows, especially for the experiment performed in this thesis. Smoke particles are produced by heating up specific non-toxic oils. These particles are usually easy to disperse and their size does not change during the experiment. However, the lower scattering efficiency compared to solid particles are a disadvantage. [23, 24]

3.3.3 Cross-Correlation

The cross-correlation is the backbone of each PIV experiment. It is a statistical analysis tool which in general determines the relationship between two functions. In the context of PIV it finds the "most probable" displacement within two reference areas. The process steps of this analysis are: 1) division of the image into small interrogation areas (IA). A broad rule is that at least $N > 10$ particles should be visible in the IA. 2) cross-correlation analysis of two IAs at time t and $t + \Delta t$. Within each IA the average displacement is calculated. It can be seen as 'moving area 1 over area 2 until the best match of the particles is found'. Perfect matching is usually not possible as particles enter and leave the IAs. Therefore, the maximum displacement of particles should not exceed 25% of the length of the IA in order to make sure that enough particles stay in a single IA. The cross-correlation is very time-consuming due to the large number of particles. A more efficient way is the use of fast Fourier transforms (FFT), reducing the computations from $\mathcal{O}(N^4)$ to $\mathcal{O}(N^2 \log_2 N)$ 3) determination of the displacement peak: the result of the cross-correlation is the highest correlation peak whereby its location is also the average displacement in the IA 4) calculation of the velocity vector. The displacement is in pixel and can then be transformed into metric units with the information obtained by the calibration 5) repetition for all IAs. The repetition of all steps for each IA results in a complete vector field representation of the flow field. [23, 25]

4 Method

Figure 4 shows the burner inlet, an assembly of swirler parts and centre and outer tube. It was built in the workshop for the PIV experiment and parts were designed in CAD for the CFD simulation. For the experiment, the centre and outer tubes were inserted into a glass tube and fixed with another component to the burner flange. The glass tube represents the 'real' combustion chamber and was also modelled with the same dimensions for the CFD simulation.

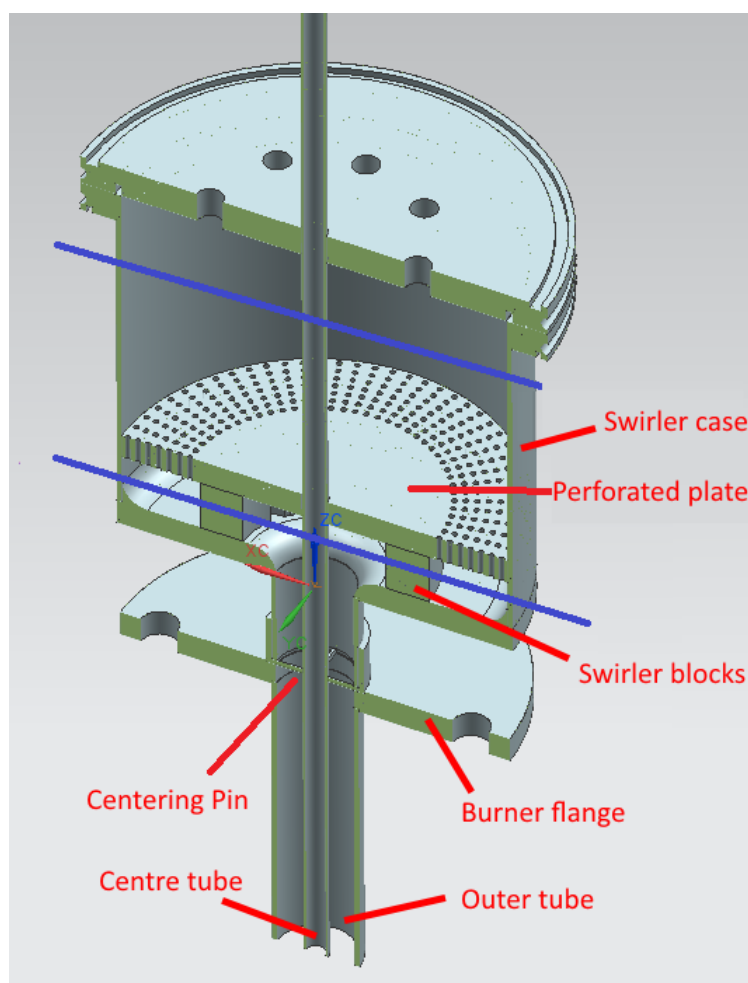


Figure 4: Cross-section geometry of swirl generator

4.1 Calculation of Swirl Number

The swirler used in the experiment is shaped 5. It consists of 16 blocks, half of them are mounted on the bottom of the swirler case. Further eight blocks are attached on the perforated plate which is inserted into the casing. By moving this top part, it is possible to set different positions of the moveable blocks to each of the fixed blocks at the bottom of the casing. Hence, it is possible to achieve

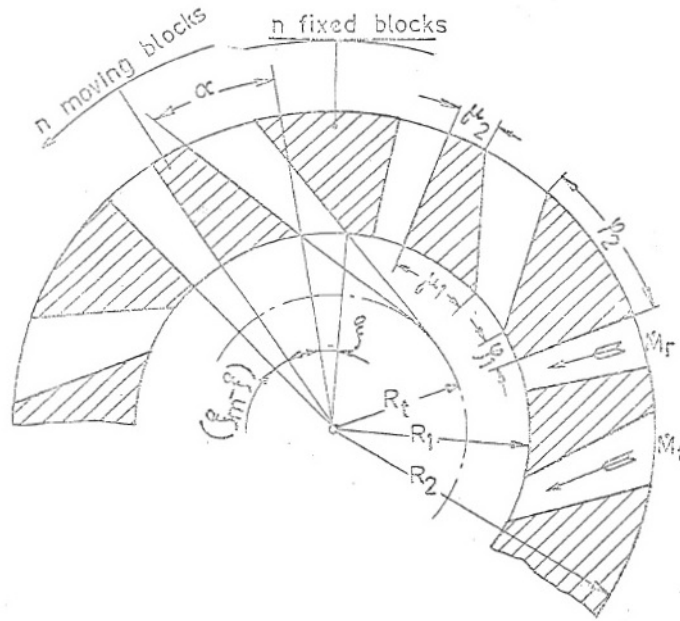


Figure 5: Cross-section geometry of the swirl generator

different magnitudes of tangential and radial flows through the vanes. If the swirler is fully closed $\xi = 0$, it means that air only flows through the radial vanes and the swirl number is $S=0$. By opening the swirler and thereby increasing the angle ξ , more air flows through the tangential vanes until the limit $\xi_m = 12^\circ$ and full swirl is reached.

The equation for the swirl number, as defined in equation (1) is very general. This is due to a lot of different types of swirl generators and calculation can be very difficult for complex swirl geometries. Therefore, it is necessary to refer to W. Leuckel [26] who calculated the swirl number for the moveable block swirler as seen in figure (5) as followed:

The exit area of all n radial channels with the adjustment angle ξ and height B is determined as:

$$A_r = (\xi_m - \xi) \cdot n \cdot R_1 \cdot B \quad (25)$$

The exit area of all 'tangential' channels with the adjustment angle ξ and height B is determined as:

$$A_t = \xi \cdot n \cdot R_1 \cos \alpha \cdot B \quad (26)$$

Consequently, the total exit area for the adjustment angle ξ follows as:

$$A = [(\xi_m - \xi) + \xi \cdot \cos \alpha] \cdot n \cdot R_1 \cdot B \quad (27)$$

By neglecting the pressure term as mentioned after equation (1) we can assume that the exit velocity is the same for the radial and 'tangential' channels and determine the velocity

as followed:

$$v = \dot{m} \cdot \rho \cdot A \quad (28)$$

and for the angular momentum flux G_t :

$$G_t = \dot{m}_t \cdot V \cdot \sin\alpha \cdot R_1 \quad (29)$$

and for the ratio of mass flow:

$$\frac{\dot{m}_t}{\dot{m}} = \frac{A_t}{A} \quad (30)$$

The last three equations combined lead to:

$$G_t = \frac{\dot{m}_t \cdot A_t}{\rho \cdot A^2} \cdot \sin\alpha \cdot R_1 \quad (31)$$

By substituting the exit areas from above we obtain:

$$G_t = \frac{\dot{m}^2 \cdot \sin\alpha}{\rho \cdot n \cdot \xi_m \cdot B} \cdot \frac{\cos\alpha \cdot \frac{\xi}{\xi_m}}{[1 - (1 - \cos\alpha) \cdot \frac{\xi}{\xi_m}]^2} \quad (32)$$

Leuckel [26] furthermore expresses the angular momentum flux G_t by a dimensionless number, the swirl number, which represents the ratio between the mean tangential velocity and the mean radial velocity at the swirl generator exit (radius R_1).

$$S = \frac{\frac{G_t}{\dot{m} \cdot R_1}}{\frac{\dot{m}}{\rho \cdot 2\pi R_1 \cdot B}} = \frac{G_t \cdot \rho 2\pi B}{\dot{m}^2} \quad (33)$$

By substituting G_t into the above equation we finally get:

$$S = \frac{2\pi}{n \cdot \xi_m} \cdot \tan\alpha \cdot \frac{\cos^2\alpha \cdot \frac{\xi}{\xi_m}}{[1 - (1 - \cos\alpha) \cdot \frac{\xi}{\xi_m}]^2} \quad (34)$$

This equation of the swirl number as a function of the angle of adjustment ξ is displayed in figure (6) and in table (1). For the PIV experiment and CFD simulation it was decided to investigate three different swirl settings. No-swirl at 0° , half-swirl at 6° and full swirl at 12° .

Angle of adjustment [$^{\circ}$] ξ	Swirl number S
0	0
1	0.11
2	0.24
3	0.38
4	0.54
5	0.73
6	0.93
7	1.15
8	1.40
9	1.67
10	1.97
11	2.30
12	2.65

Table 1: Angle ξ and swirl number S

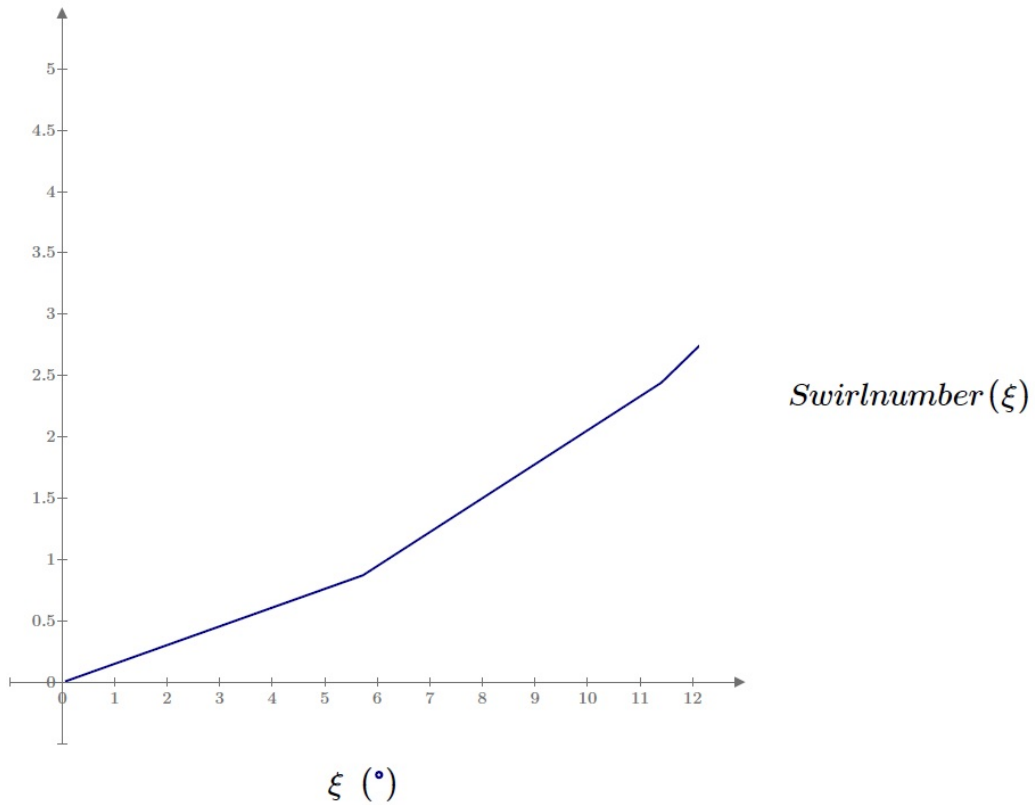
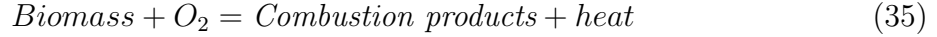


Figure 6: Swirl number as function of angle ξ

4.2 Flow Rate Calculation

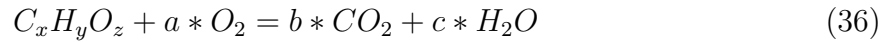
In order to set the air flow rate for the experiment the calculation was performed as if biomass was being burnt in the real burner. Burning biomass with oxygen lead to a combustion reaction which liberates heat and combustion products. This heat could then be used for various objectives, however, they will not be further discussed here. The combustion products are mainly the most common oxides such as carbon dioxide and sulphur dioxide, and water.



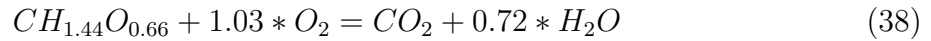
For the following calculation we will use the simplified assumption that biomass consists only of carbon, hydrogen and oxygen with the following mass fraction:

- C = 50%
- H = 6%
- O = 44%

The combustion reaction will follow as:



From this equation we can calculate for 1 mol carbon the correct stoichiometric coefficients a, b and c :



Therefore, 1 mol carbon needs 1.03 mol O_2 and together with the molar mass of carbon ($M_C = 12.01g/mol$) we obtain the molar flow rate of O_2 as followed:

$$\dot{n} = \frac{0.5\%}{12.01 \frac{g}{mol}} * 10^3 * 1.03 mol = 42.917 \frac{mol}{kg \text{ biomass}} \quad (39)$$

As the molar volume at 'Normal Temperature and Pressure' (NTP) at $T=20^\circ C$ and $p=1atm$ is 24.04 L/mol we obtain the flow rate of O_2 per kg biomass for complete combustion:

$$42.917 \frac{mol}{kg \text{ biomass}} * 24.04 \frac{L}{mol} = 1111.54 \frac{L}{kg \text{ biomass}} \quad (40)$$

Parameters of burner and inlet

- Amount of biomass flow rate: 2 kg/hr
- Air-fuel ratio λ :
 - $\lambda=0.4$ for gasification

- $\lambda=1.3$ for combustion (with excess air)
- Inner diameter of centre tube $d_{i,CT}$: 7.747mm
- Outer diameter of centre tube $d_{a,CT}$: 9.525mm
- Inner diameter of outer tube $d_{i,OT}$: 36.576mm
- Minimum velocity of centre tube for pneumatic transport: 3 m/s
- Percent of minimum velocity: 120%
- Composition of air: 21% O_2 , 79% N_2

With the information of the list above as well as calculating from (40) and considering the biomass flow rate and the composition of air, we can obtain a stoichiometric air flow of 176.4 L/min.

By setting 120% of the minimum velocity in the centre tube and together with the area of the centre tube and the area of the annulus of the outer tube we can finally obtain the volume flow rates for the two tubes. In addition, four different velocity ratios between centre and outer tube were set. For VR1, the most minimal velocity of the centre tube was set and from this value, the volume flow rate for both tubes were calculated. For VR2 and VR3, the exit velocity of the centre tube were each time doubled. For VR4, the volume flow rate was calculated for $\lambda=0.4$ which is used for gasification. Figure 7 shows the velocity and volume flow rate for each velocity ratio. The PIV experiment was performed for all velocity ratios but due to time limitations, the CFD was only simulated for VR1.

Flow rate setup for experiments:					
Lambda λ	-	1.3			0.4
Velocity ratio	-	1	2	3	4
Velocity at center tube	m/s	3.7	6.6	12.2	3.7
Flow rate Primary air at center tube	L/min	10.2	18.6	34.4	10.5
Velocity at outer tube	m/s	3.7	3.6	3.4	0.9
Flow rate secondary	L/min	202.0	193.9	178.2	54.8

Figure 7: Flow Rate and Velocity Ratios for the Experiment

4.3 CFD Simulation Procedure

Computational simulation was done using ANSYS, Inc. - Fluent, Version 19.0. ANSYS - Fluent is a computational fluid dynamics (CFD) tool to model and solve flow, turbulence, heat and reaction applications. The software is among other things capable of modelling three-dimensional flow structures of laminar, turbulent, steady, transient, compressible or incompressible flow patterns. ANSYS Workbench is the main interface and combines all the available add-on modules. In the context of this simulation, the modules 'Design Modeler', 'Meshing' and 'Fluent' were used and linked together in the workbench interface. The procedure of the CFD Simulation can be seen in figure 8 and each step is then described in the following chapters.

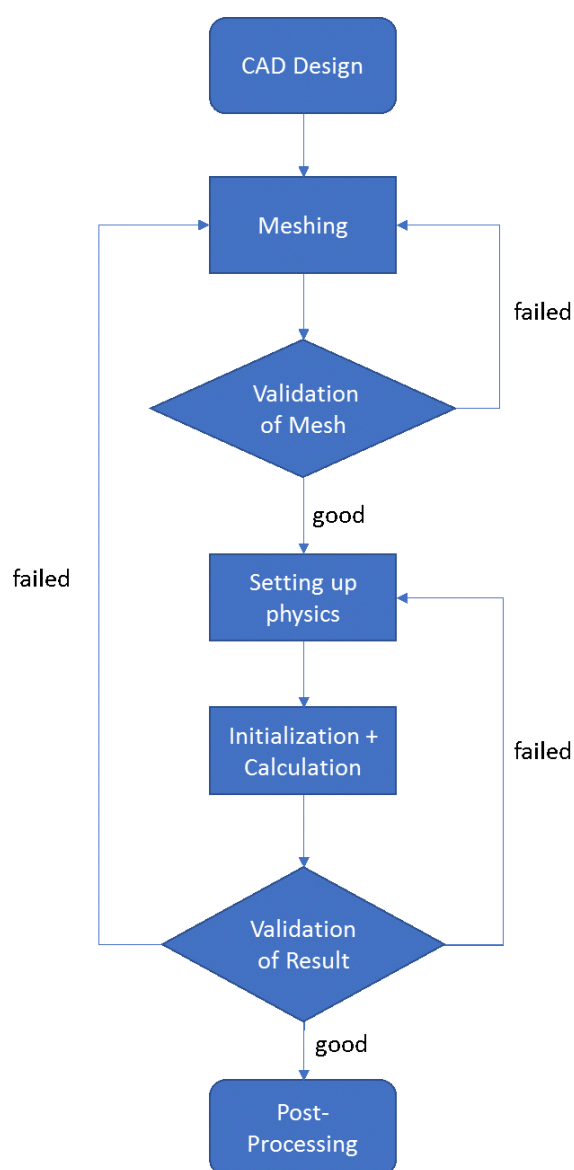


Figure 8: Procedure of CFD Simulation

The first step was the CAD modelling of the fluid domain for the different swirl setups. As the position of the tangential and radial vanes change for the three swirling setups, each one had to be modelled and meshed in ANSYS individually. The 3D-CAD model of the structure including inlets, swirler and tubes was first created in the CAD-software CATIA V5R20, then transferred via the Initial Graphics Exchange Specification (IGES) file format to ANSYS and eventually generated in the 'DesignModeler'. Due to limited computer performance I did not model the eight inlets for the swirling air at the top and also omitted the perforated plate. The meshing of all 2mm holes on the plate would produce a lot of elements. Furthermore, the purpose of the perforated plate is to homogeneously distribute the air before entering the swirl vanes. In ANSYS the velocity magnitude defined on the inlet area is already homogeneously distributed and hence, the function of the plate for the CFD simulation would end up being meaningless. Therefore, I set the exit area of the little holes on the perforated plate as the air inlet for the simulation. This adjustment would immensely reduce the number of elements for the grid. Since the calculation time is generally proportional to the number of cells, the time for simulation could also be cut down hugely. The final model can be seen in Figure 9.

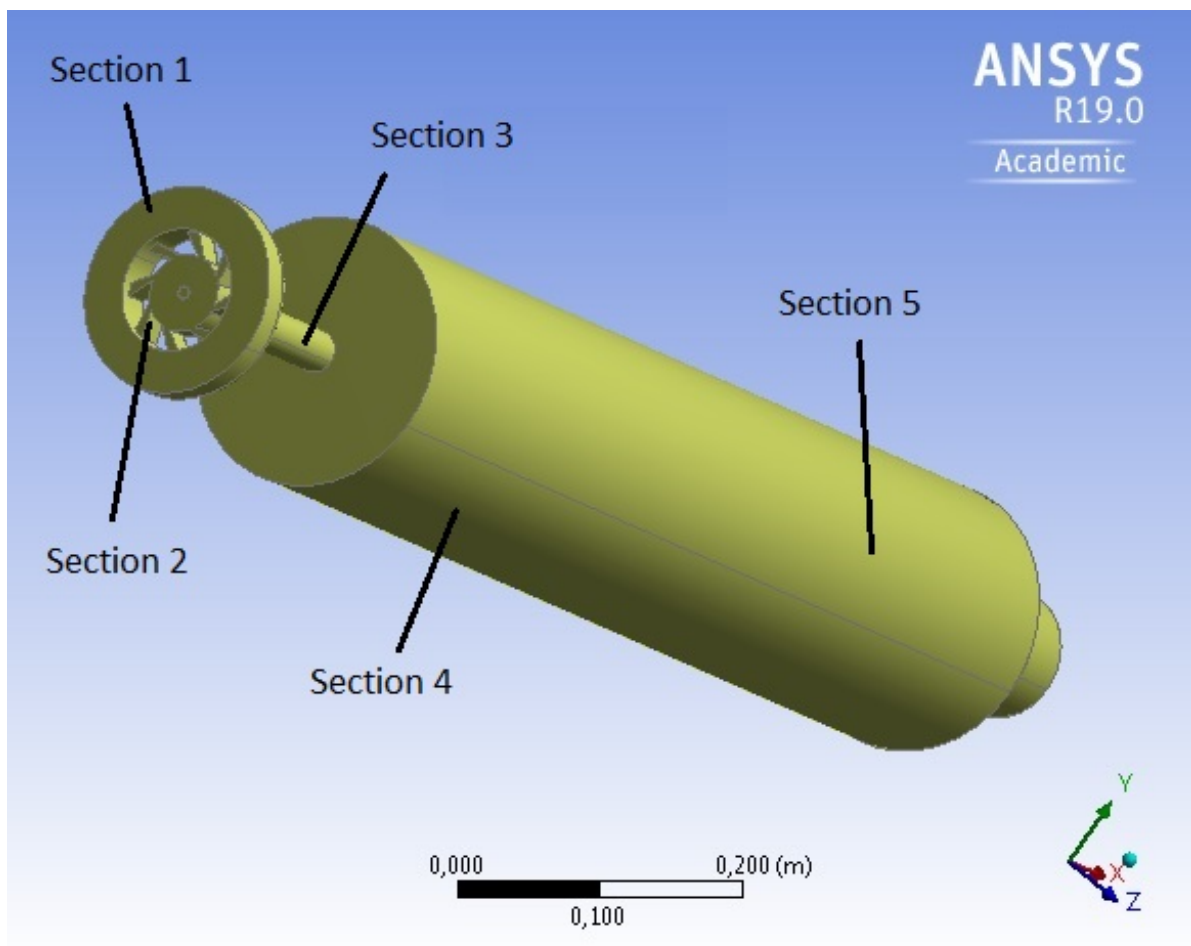


Figure 9: CAD-Model

4.3.1 Meshing

After the model was loaded into the meshing module, the first step was to define the inlets for centre and swirling air as well as the outlet of the system. Following this, a suitable and feasible mesh had to be applied to the model. I identified five separate sections (Sections 1-5) in the system which needed different mesh management as follows: Inlet (Section 1), swirling section (Section 2), connection tube to the combustion chamber (Section 3), upper (Section 4) and lower (Section 5) part of the combustion chamber (see Figure 9). To begin with, initial tests and information found in adequate literature [18, 27, 28] allowed to determine the approximate length of the velocity field inside the combustion chamber. As the longest possible flow field in the combustion chamber was around 40cm, it was possible to apply a much coarser mesh in the lower part (section 5) of the chamber in comparison to the upper part (section 4). Further attention had to be set on section 2 as, especially the little vanes needed to be meshed precisely. Regarding the inlet area as well as the connection tube between the swirler and the combustion chamber, I also set different mesh sizes always with an eye on mesh quality and total number of elements. The mesh for the full-swirl setup can be seen in Figure 10. Due to the even smaller radial and tangential vanes for the half swirl setup, the sizing for this section in the half swirl model was even more refined. This is the reason why the number of elements for the half swirl setup is almost doubled in comparison to the other swirl setups. Details and Sizing of the meshes can be found in Table 2 and Table 3. For the size function which defines how the mesh is spread and distributed over the surface and volume of the model, I chose the curvature function. It is defined by the Min/Max Size of the elements, growth rate and normal angle.

Details and Sizing of the Mesh	
Cell shape	Tetrahedron
Element order	linear
Size Function	Curvature
Growth Rate	1.20
Curvature Normal Angle	18°
Element Size Section 1	2,e-003m
Element Size Section 2 for Full/No Swirl	8,e-004m
Element Size Section 2 for Half Swirl	5,e-004m
Element Size Section 3	2,e-003m
Element Size Section 4	5,e-003m
Max. Element Size Section 5	6,1e-002m

Table 2: Details and Sizing of the Mesh

No Swirl	#
Number of Nodes	731,245
Number of Elements	4,113,890
Half Swirl	#
Number of Nodes	1,371,052
Number of Elements	7,852,398
Full Swirl	#
Number of Nodes	805,250
Number of Elements	4,539,145

Table 3: Number of Nodes and Elements

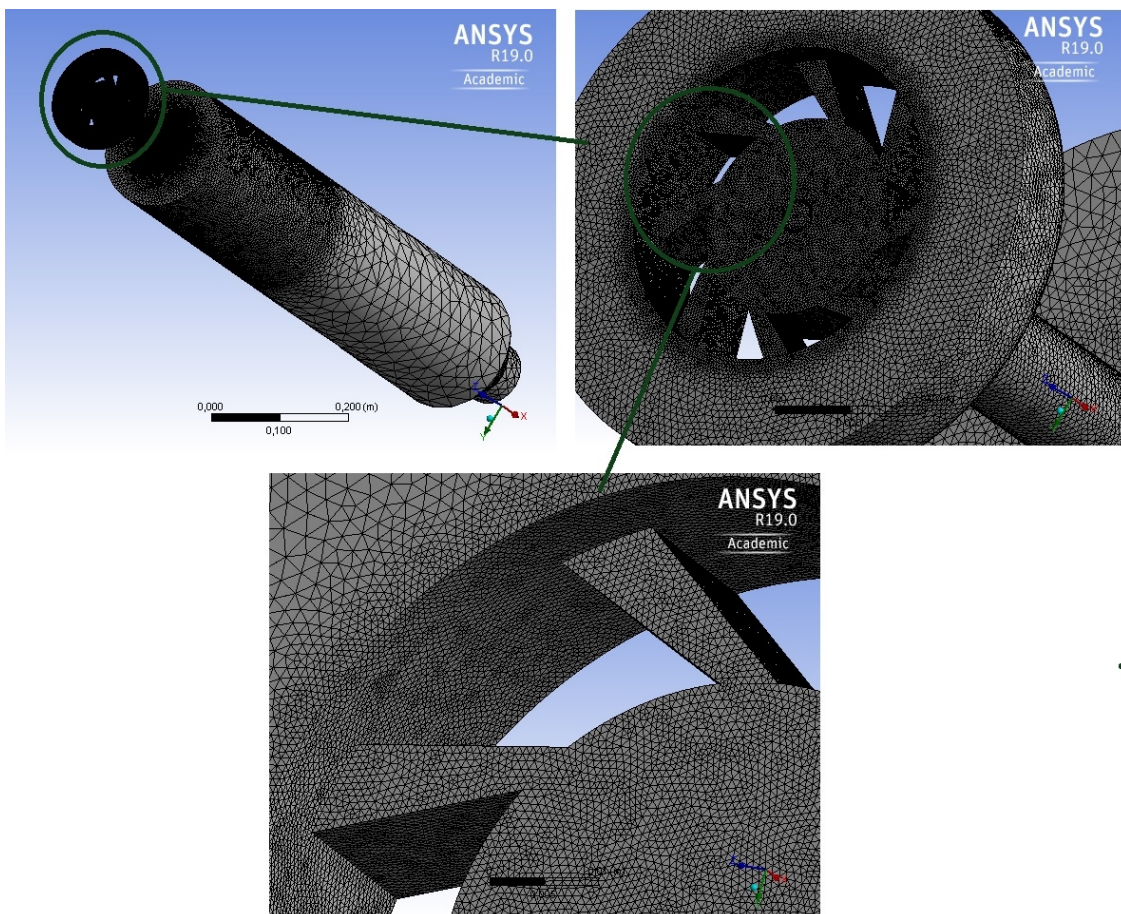


Figure 10: Mesh for Full-Swirl Setup

4.3.1.1 Mesh Validation

The quality of the mesh greatly influences the accuracy, convergence, stability and speed of the solution. A bad mesh leads to convergence difficulties, poor physics description and diffusive solution. The reason for this is very complex due to the fact that mesh-quality is relative and the solution is an approximation. Therefore, checking and validating the quality of the mesh is essential. The perfect shape for the tetrahedron element is a cell with four equilateral triangle faces. Most of the quality criteria check how far a given cell deviates from this ideal shape. Two parameters have been examined to determine and analyse the quality of the mesh:

- Skewness
- Orthogonal Quality

Skewness will help to determine the quality inside the cell itself and orthogonal quality gives information regarding the quality of adjacent cells. The validation of results will be discussed in chapter 4.3.3.

Skewness: This factor is defined as the volume deviation between the ideal cell which consists of all angles at 60° , and the actual cell with the same radius (see Figure 11).

$$Skewness = \frac{OptimalCellSize - CellSize}{OptimalCellSize} \quad (41)$$

The distribution of the skewness for all elements of the mesh can be seen in figure 14. The heat map which was taken from [29] shows the allocation for cells with value 0 (perfect) to 1 (unacceptable). The average skewness value for the whole mesh was 0.203.

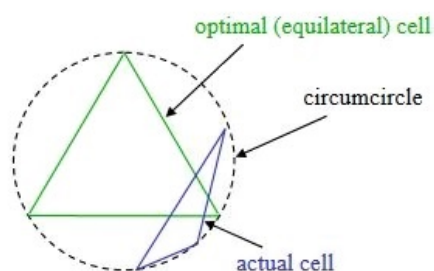


Figure 11: Skewness Definition

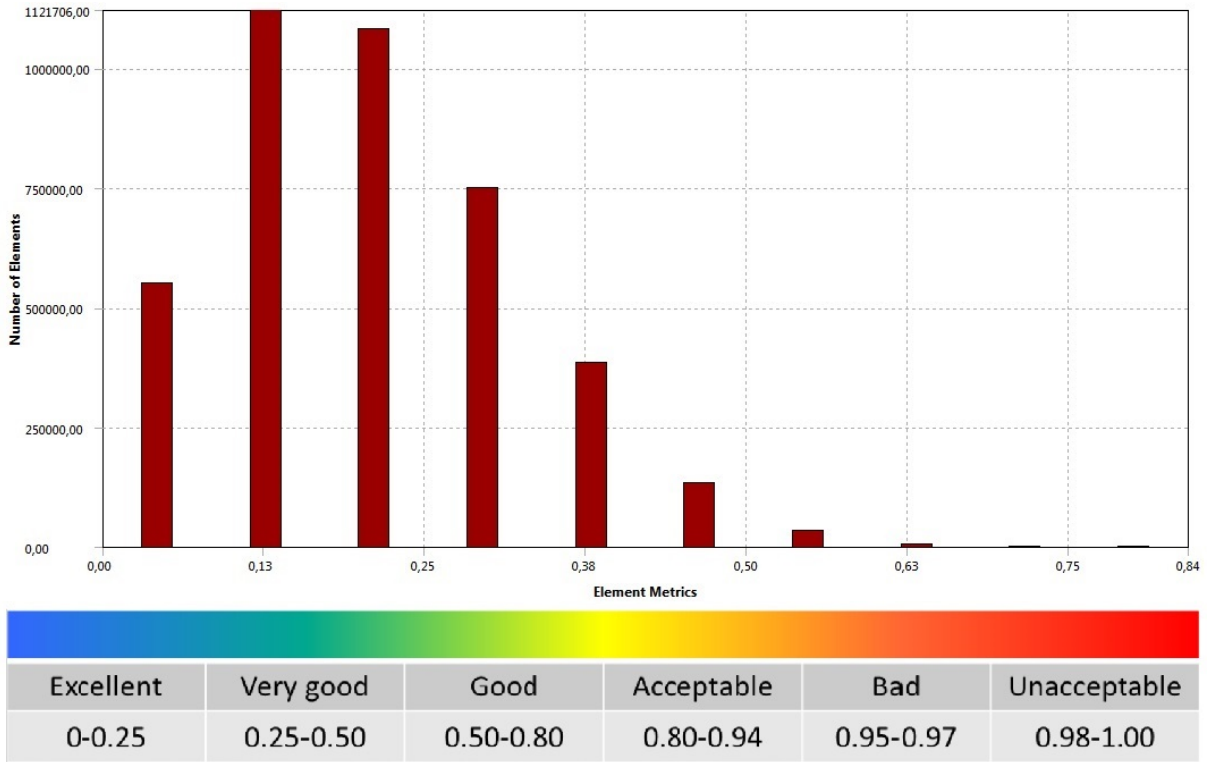


Figure 12: Skewness Distribution

Orthogonal Quality: The orthogonal quality is calculated for elements using the face normal vector \vec{A}_i , \vec{f}_i being the vector from the centroid of the cell to the centroid of that face and \vec{c}_i , which is the vector from the centroid of a cell to centroid of the adjacent cell that shares the same face. The orthogonal quality is then defined as the minimum of the following equations:

$$\frac{\vec{A}_i * \vec{f}_i}{|\vec{A}_i| * |\vec{f}_i|} \text{ and } \frac{\vec{A}_i * \vec{c}_i}{|\vec{A}_i| * |\vec{c}_i|} \quad (42)$$

The orthogonal quality of all cells of the model can be seen in Figure 14 with the heat map again taken from [29]. The worst cells will have an orthogonal quality closer to 0, with the best cells closer to 1. The average value for all cells is 0.81.

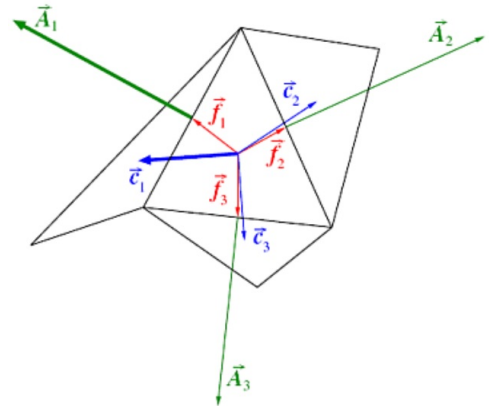


Figure 13: Orthogonal Quality Definition

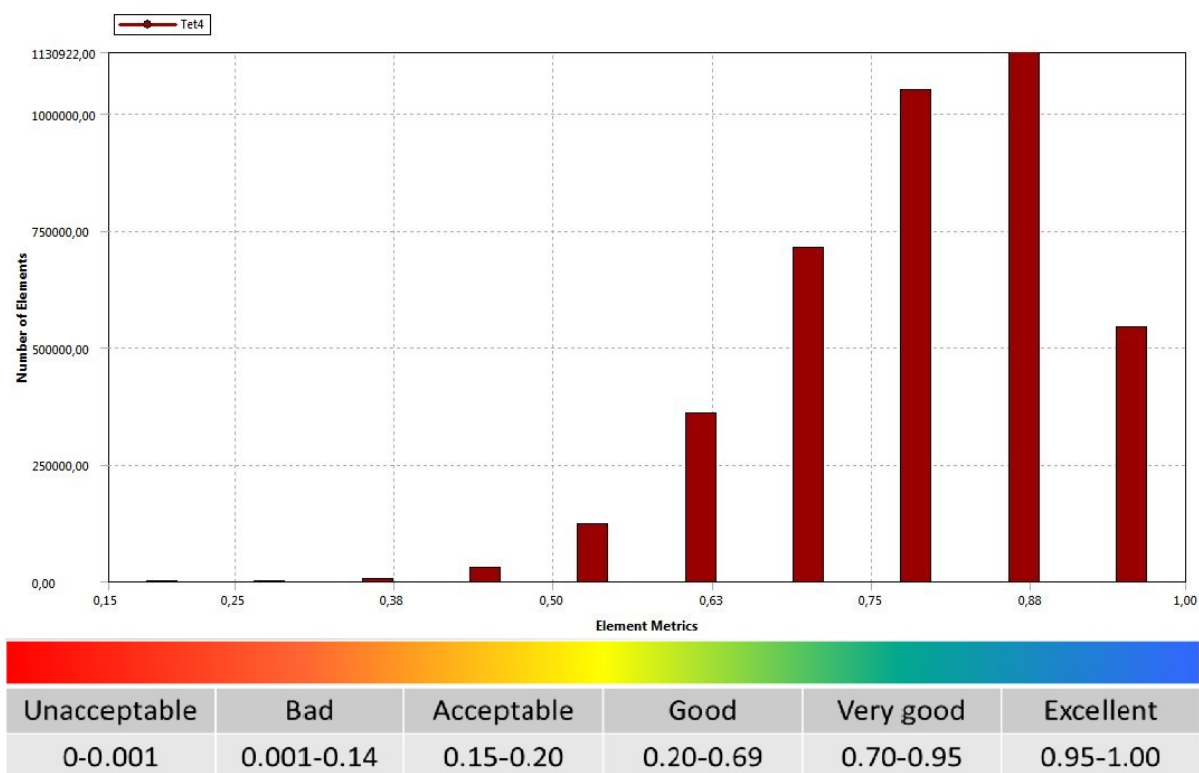


Figure 14: Orthogonal Quality Distribution

4.3.2 Simulation Setup

After the quality of the mesh was checked, the next step was to load the model into the *Fluent* environment. There, the boundary conditions were applied to the model. The velocity at the inlets were set for the centre and swirling air as calculated in chapter 4.2. Air was chosen as the main fluid with density at $1.225 \frac{kg}{m^3}$ and the dynamic viscosity at $1.789 \cdot 10^{-5} \frac{kg}{m \cdot s}$. No-slip walls for the model were defined with the material aluminium. Furthermore, a pressure-outlet was specified as the exit.

Regarding the solver I chose to use the steady-state pressure-based solver. Although ANSYS FLUENT has two solvers, the pressure-based and the density-based solver, the pressure-based solver was considered to be the preferred option for this simulation as it is applicable for a wide range of flow regimes. The pressure-based solver employs a solution where the governing equations are solved sequentially. This is done by deriving a pressure equation from the continuity and the momentum equation in a way that the velocity field satisfies the continuity. As a result of the non-linearity of the governing equations and the coupling to one another, the solution procedure requires iterations. All the governing equations are solved repeatedly until the solution converges.

As an initialisation, I ran the simulation for 200 iterations. The discretisation scheme for turbulent kinetic energy k and the turbulent dissipation rate ϵ was resolved at 'First Order Upwind' scheme. Subsequently, another 800 iterations followed, this time with a 'Second Order Upwind' discretisation scheme for k and ϵ . This procedure was not only done to decrease calculation time, but the solutions also converged slightly better than running the simulation only for 1000 iterations at 'Second Order Upwind'.

4.3.3 Result Validation

Before results can be analysed, the CFD simulation has to be validated as it is a major part in any CFD project. There are several methods to determine simulation convergence. Current research, especially [14, 30, 31], recommends a combination of holistic (e.g. specific residuals which represent the error across all control volumes in the simulation) and an amount of local quantities to ensure a correct and converged solution. For this simulation I additionally applied a grid independence study to make sure that the solution does not change with further grid refinement. The mesh itself was already checked in chapter 4.3.1.1. This chapter is about certifying the solution results and for that purpose I use in total three different methods:

- Residual Convergence
- Monitoring Points
- Grid Independence Study

4.3.3.1 Residual Convergence

Residuals are probably the best-known measurements of an iterative simulation's convergence. They directly quantify the imbalances (or errors) in the solved equations for each variable between two iterations. Therefore, at the end of each solver iteration, the residual sum is calculated out of every control volume in the model for each equation being solved. For infinite iterations steps with infinite precision, the residual will reach at some point zero but for an ordinary computer, the residuals decay to some small value. The smaller the value, the more numerically accurate the final solution. The default convergence to stop the calculations in Fluent is 10^{-3} , this was changed to 10^{-6} as most literature recommend this value for a better, more converged solution. The following Figure 15 shows the behaviour of the residuals for the full swirl setup on a logarithmic axis. The continuity and velocity variables reach values of $5 - 9 * 10^{-6}$ and the k and ϵ variables around $1 - 3 * 10^{-5}$, depending on the no-, half- or full-swirl setup.

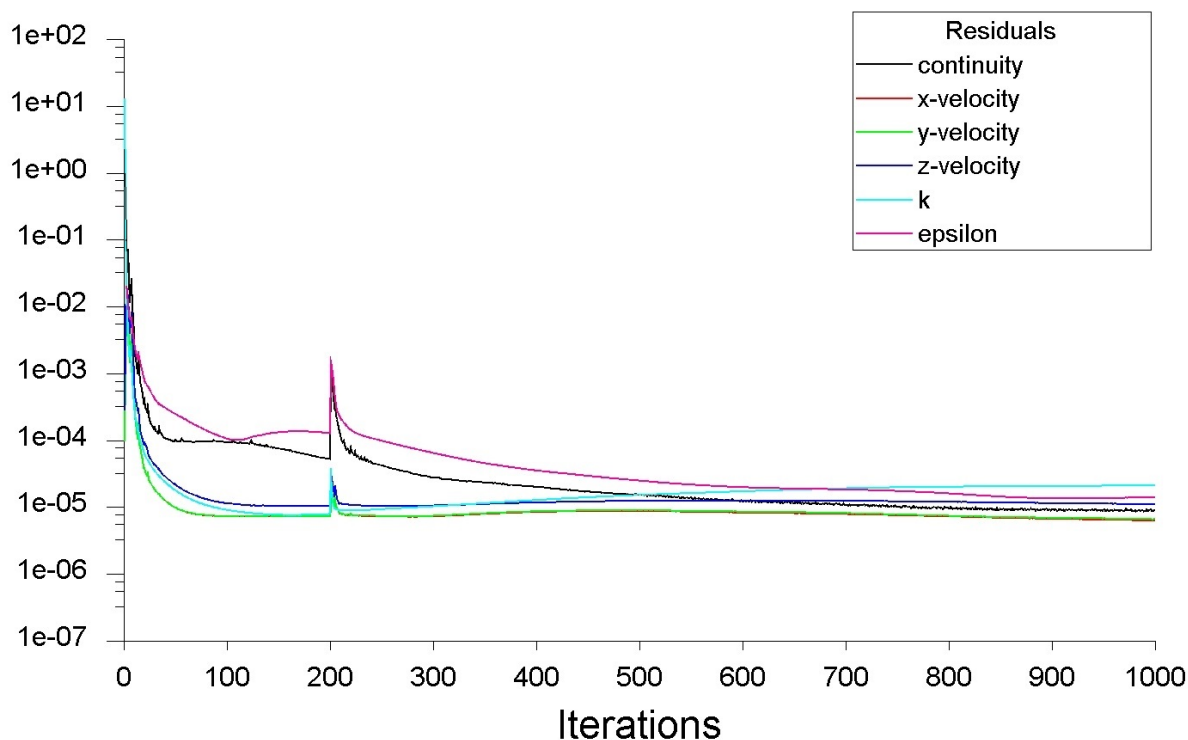


Figure 15: Convergence of Residuals for Full Swirl Simulation

4.3.3.2 Monitoring Points

Beside the convergence of the residuals, another main indicator for convergence of the simulation is the change of 'local quantities' throughout the calculation domain. This means for a steady state analysis, variables should no longer change from iteration to iteration for a simulation to be deemed acceptable. For this method, three monitor points were set in the model at different locations. The position of the points in the model can be seen in Figure 16. Two points were set at 5cm , and respectively 10cm after the entry into the combustion chamber. Another monitor point was set in the outer tube. This third point was set to check the progression of the velocity but also to look at the convergence of the swirling velocity in the narrow tube.

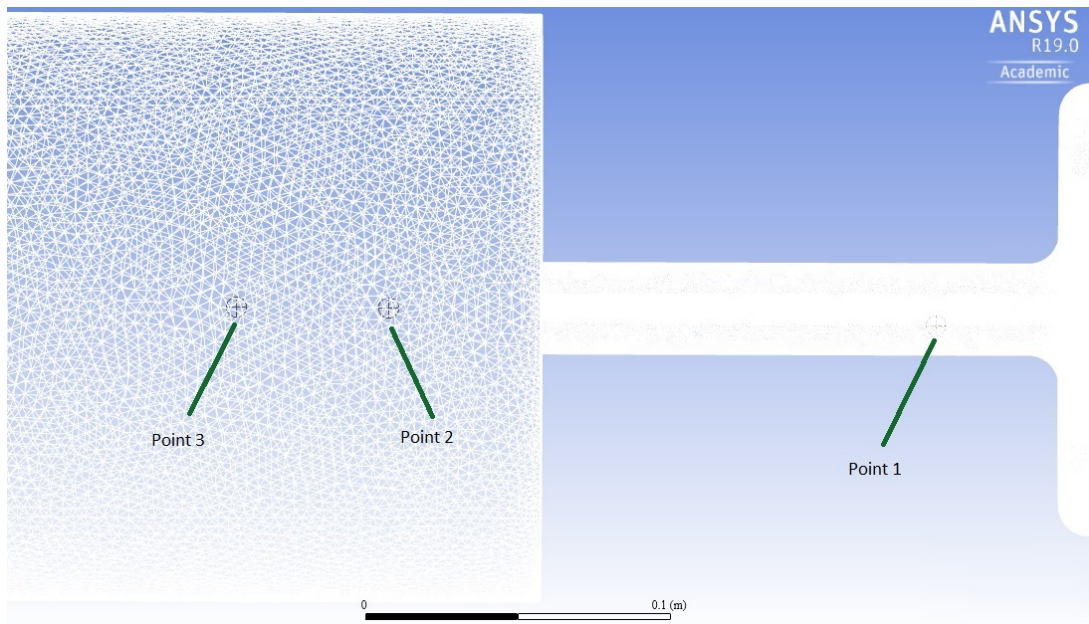


Figure 16: Position of Monitor Points

The results for the monitor points can be seen in Figure 17. It shows the velocity over the number of iterations for the three different monitor points in the full swirl setup. The two different colours for each graph show the progress of first and second order discretisation scheme. An acceptable convergence to a certain value is given for all three monitor points and a simulation for more than 1000 iterations was deemed surplus.

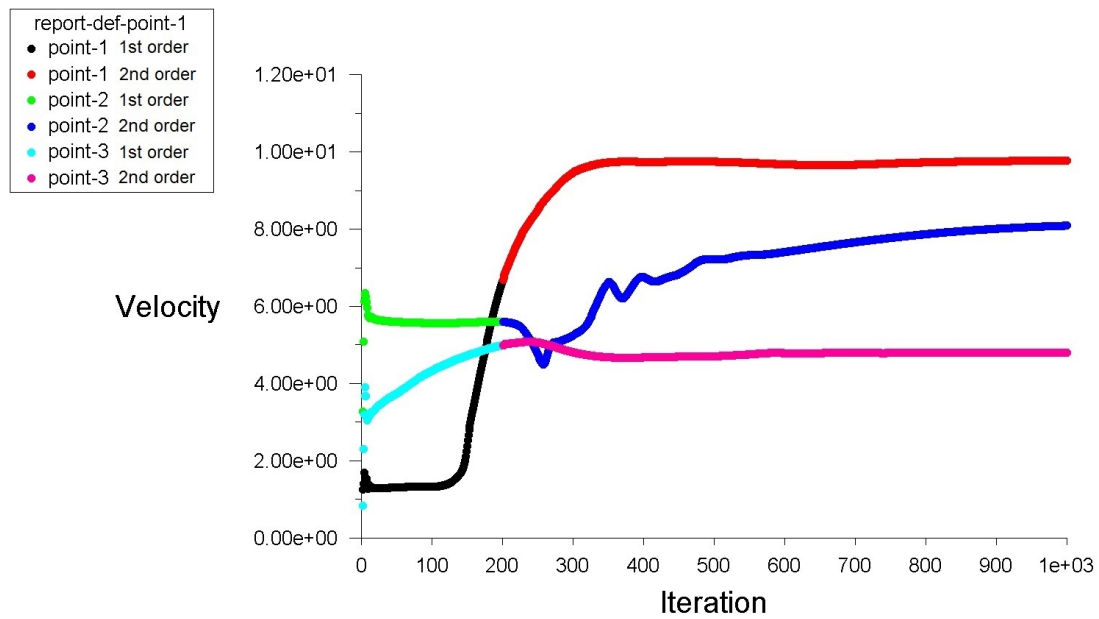


Figure 17: Velocity over Iterations for the Monitor Points

4.3.3.3 Grid Independence Study

In order to ensure that the solution is mesh-independent, a finer grid was created. Due to high time-consumption of the calculation, only the grid for the full swirl setup was modified. To compare the coarser with the finer mesh, the same monitor points as in the previous chapter were used. The sizing of the initial mesh can be seen in Table 2 and 3 and the position of the sections in Figure 9 . The element size for section 1, 3 & 4 was decreased by 50%. Due to the very large number of cells in section 2, the element size for this section was only reduced by 25%. The maximum element size for section 5 was not changed, as finer cells in this area would not have a significant impact on the final solution and would only raise the number of cells. This would unnecessarily increase the simulation time. A detailed listing of the new and finer mesh can be seen in Table 4. It also shows that the number of elements and nodes in the new mesh compared to the initial mesh almost quadrupled.

Details and Sizing of the finer Mesh	
Element Size Section 1	1,e-003m
Element Size Section 2	6,e-004m
Element Size Section 3	1,e-003m
Element Size Section 4	2.5,e-003m
Max. Element Size Section 5	6,1e-002m
Number of Nodes	3,102,254
Number of Cells	17,594,531

Table 4: Details and Sizing of the finer Mesh

Figure 18 shows the velocity at the monitor points over the iterations for the two different meshes, the initial grid 1 (G1) and the finer grid 2 (G2). After around 500 iterations the difference of the solution between the two meshes becomes very small. The final difference in velocity after 1000 iteration for G1 and G2 is for every point below the value of 0.6%.

Summarising all validation methods, it can be stated that the results are based on acceptable and sufficient CFD simulations. The mesh analysis in chapter 4.3.1.1 showed an excellent value for the skewness of the average cell according to the ANSYS Fluent guide. The orthogonal quality predicted the quality of adjacent cells and the average value displayed a very good distribution. For the calculation, the residuals of all variables converged towards acceptable values as well as the velocity magnitudes in the monitor points that showed a sufficient trend. The grid refinement resulted in a very small error of 0.6% between the coarse and fine mesh which made a Richardson extrapolation redundant.

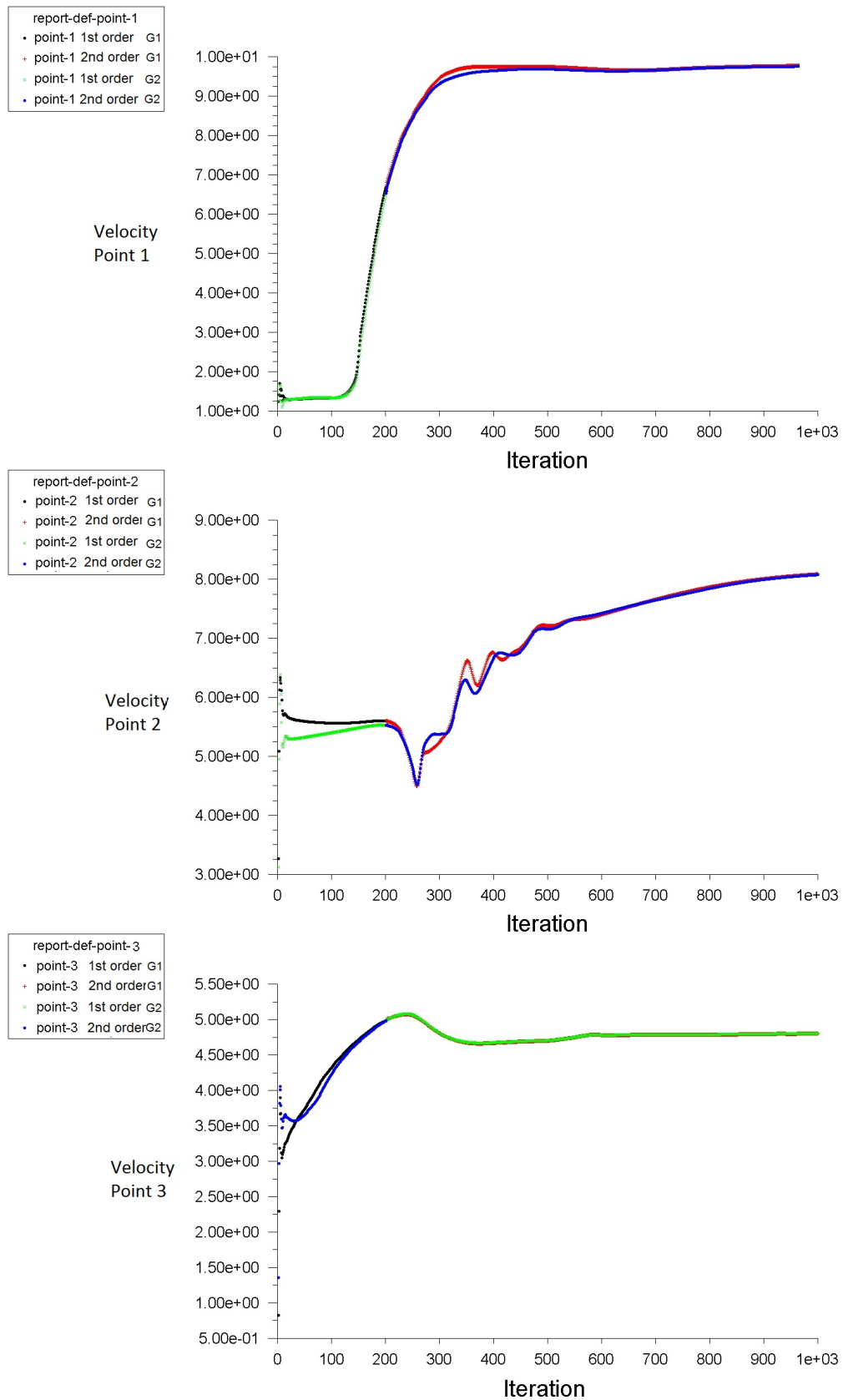


Figure 18: Monitor Points for Grid Independence Study

4.4 PIV Experiment

4.4.1 Setup

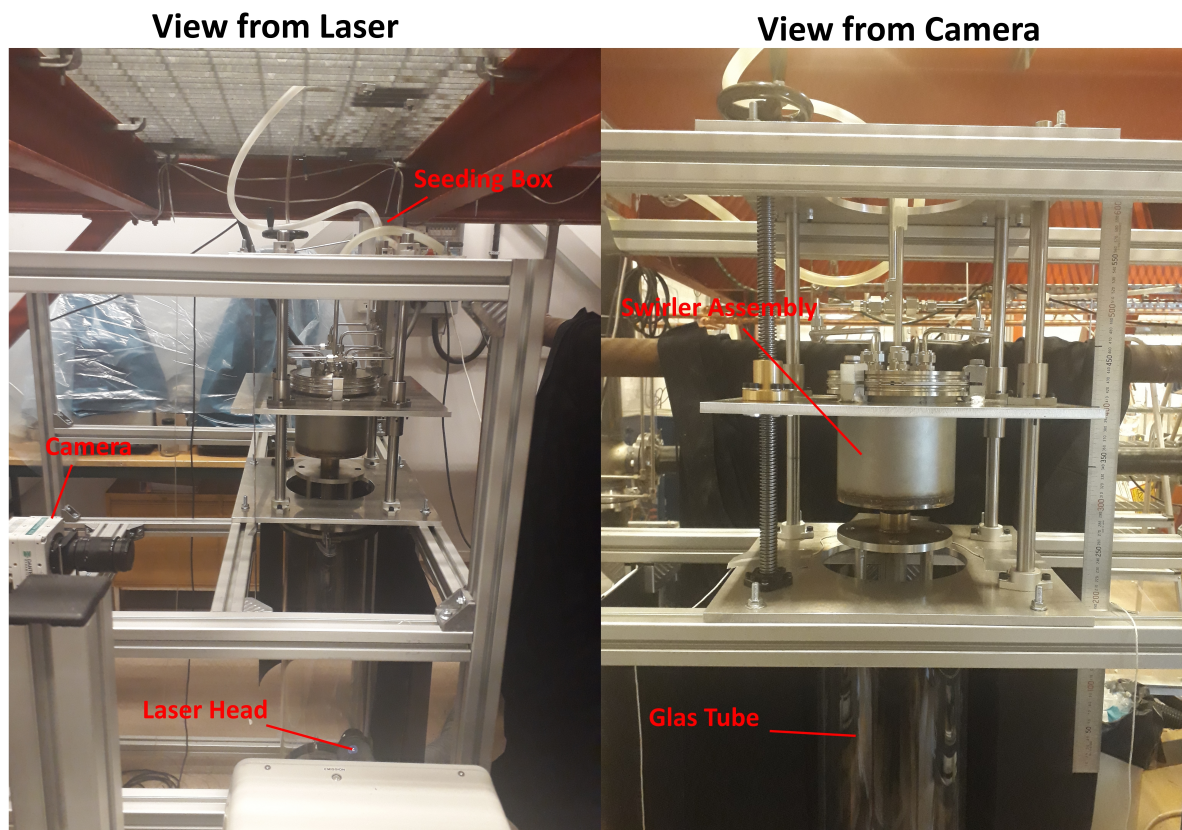


Figure 19: Setup of PIV Experiment - left) view from the laser, right) view from the camera

Figure 19 shows the experimental setup of the PIV system used in the experiment. All important parts are marked in the image. The whole structure with all the metal beams was specifically built for this experiment. The camera was mounted on the horizontal beam and in a central position focussing on the glass tube. The glass tube represents the combustion chamber. The laser pointed orthogonally to the camera at the glass tube. The process to determine the exact position of camera and laser will be further discussed in chapter 4.4.2.1. The swirler assembly was mounted on a lift in order to allow for height adjustment. By turning the black wheel on the top, it was possible to move the swirler assembly up and down. Therefore, by changing the height of the swirler, the nozzle exit could also move up and down inside the glass tube because the glass tube was attached to the beam structure. The advantage of this system was to allow for easy changes to the position of the nozzle outlet by moving the lift up and down. This made it possible to look at different areas of the flow field by keeping the camera and the laser always at the same position. Hence, it was also only ever necessary once to calibrate the camera.

An air compressor supplied the air for the experiment and the air flow rate was controlled and regulated on a laptop with the software FlowmasterTM. It was possible to set different volume flow rates for the centre and swirling air which were connected via plastic pipes to the metal tubes. The outlet of the glass tube was connected with a pipe to the ventilation system.

The software used for the PIV experiment was DynamicStudio 6.0 by Dantec Dynamics which was particularly designed for the PIV technique. The software provides setup and control of hardware and the device connections. Calibration, data acquisition, storage and analysis were all performed with DynamicStudio. Connected to the PC was also the synchroniser Model 575 by Berkeley Nucleonics Corp. Its task was to synchronise the pulses from the laser and the recording of the camera. The laser was connected with two and the camera with one trigger cable to the synchroniser. The camera was also connected with an ethernet-cable connection to the computer. The connection setup can be seen in Figure 20.

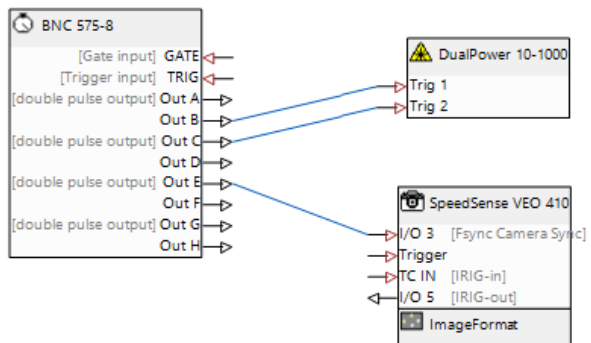


Figure 20: Connection Setup of Synchronizer with Camera and Laser

4.4.1.1 Smoke Seeding

For air flows, the particles are usually small oil droplets in the range $1\mu\text{m}$ to $5\mu\text{m}$ as recommended by the manufacturer of the PIV system, Dantec Dynamic, and the following literature [24, 32]. The particle seeding was achieved with an 'Aerotech Smoke Generator'. It produces smoke by pumping white oil from the control unit to the tip of the wand, where a low voltage electrical coil heats it to produce a dense plume of smoke. The wand was placed inside an acrylic box, the seeding box, which also had an air in- and outlet. Clean air from the compressor entered inside the box with a certain flow rate controlled by the software and got seeded with small smoke particles. It then leaves the box via a plastic pipe to the central metal tube.

4.4.1.2 Camera

For recording the PIV experiment, a SpeedSense VEO 410 from Dantec Dynamics was used as seen in Figure 21. It is a high-speed, high image quality camera particularly designed for special requirements of experiments including PIV, LIF and spray characterisation. Attached to it was a ZEISS Milvus2/100M optical lens with manual focus. More detailed specifications can be seen in the table below:



Figure 21: SpeedSense VEO 410

Technical Specifications	
Speed (fps)	5,200
Resolution (MP)	1
Sensor Resolution (Pixel x Pixel)	1,2800 x 800
Interframe time (ns)	480
Pixel Size (μm)	20
Pixel depth (bit)	12
Memory Storage (GB)	36

Table 5: Technical Specifications of the Camera

4.4.1.3 Laser

The laser used for the experiment was the Nd:YLF LDY303 by Litron Lasers and can be seen in Figure 22. LDY-PIV series lasers are a dedicated configuration primarily in use as illumination source for Particle Imaging Velocimetry. The system uses two CW Q-switched Nd:YLF DPSS laser resonators producing infrared laser light at 1053nm which is converted to visible 527nm laser light by an intra-cavity Harmonic Generation Assembly (HGA). The harmonic generator produces a laser output at 527nm (green). To ensure that both laser outputs can be used with a single set of external optics the 527nm laser beams are combined using polarisers and exit through a single port of the laser head. The use of two independently pulsed and controlled resonators allows the generation of

a double pulse output with inter-pulse separation times of less than 10 nano-seconds where required. This ultra-short inter-pulse separation cannot be achieved using a single resonator laser fitted with an electronic double pulse option. The short pulse duration achieved by acousto-optic Q-switching the laser resonator allows the motion of fast-moving particles to be frozen in the image. [33]

As the laser is very powerful and can be harmful, it was very important to follow laser safety measures. This included attaching laser barriers to the windows, laser safety shields behind the glass tube and wearing safety goggles at all time when the laser was in use.



Figure 22: Litron Laser LDY300 PIV Laser

4.4.2 Procedure

The following figure 23 shows the process of the PIV experiments. The steps will be described more in detail in the following chapters. For each velocity ratio and each swirl number, it was necessary to look at three different positions. This was done due the length of the flow field compared to the relative small height of 7cm of the recorded image. For this, the swirler-outlet was moved upward 7cm to the 2nd position with the help of the lift and then another time to the 3rd position. Resulting from this 3 swirl numbers x 4 velocity ratio x 3 positions = a total of 36 runs had to be recorded.

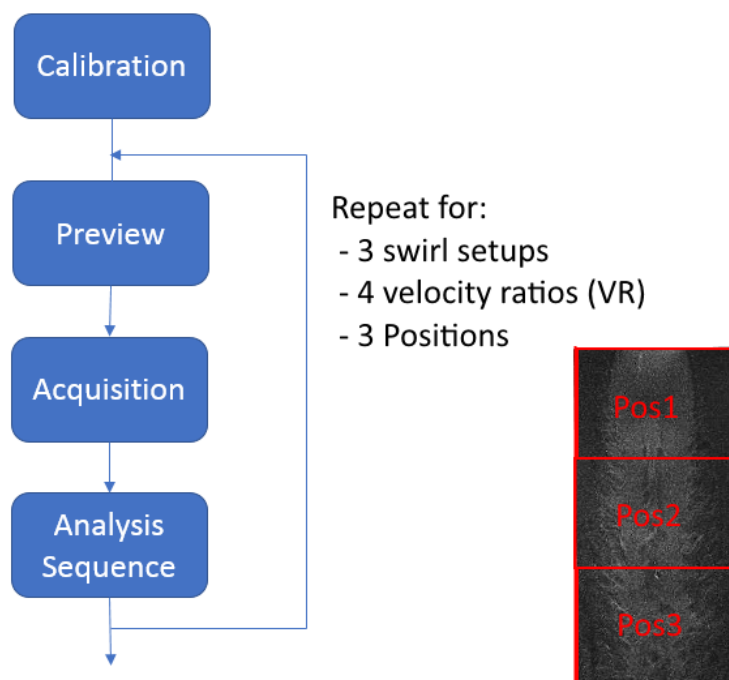


Figure 23: PIV Experiment Procedure

4.4.2.1 Calibration

First of all, it had to be ensured that the laser was positioned orthogonal to the camera and its beam pointing centrally towards the glass tube. The position of the laser is very important as even small deviations can influence the result. This was done applying the following method: A white sheet was inserted into the glass tube with the position of the axial centre line marked on the sheet. It was essential for the line to be placed exactly in the middle of the tube and the laser beam had to overlap the drawn line. Furthermore, the laser beam was also focused and the laser sheet thickness was around 2mm. A second step had to be done to guarantee the orthogonal position of the laser to the camera. The axial centre line of the glass tube was 'projected' on the black laser safety shield which was mounted around 50cm behind the tube. The axial centre line was precisely measured and marked on a white sheet and applied on the laser safety shield. Then, the laser was rotated in a way that the laser beam went through the glass tube and overlapped the projection of the axial centre line marked on the laser safety shield. If the laser beam then overlapped the centre line in the glass tube as well as the projection on the safety shield, the laser was correctly positioned.

The next step was the calibration the camera. First, the calibration-target was inserted into the glass tube and fixed in a central and horizontal position. With the help of a strong LED lamp mounted on the camera, the target plate was illuminated. 'Dynamic-

4 Method

Studio' allows the user to choose between three different modes: 'Free Run', 'Preview' and 'Acquire'. In 'Free Run'-mode only the camera is running to adjust the aperture and focus in a way that the target plate was well visible and focused on the centre dot of the target plate. 'Preview' and 'Acquire' will be described in chapter 4.4.2.2. Figure 24 shows the image of the target plate with the big, white centre dot in the middle. The feature 'Measure Scale Factor' provides the software with the size-correlation between the recorded image and the 'real' dimensions. The real distance between each dot was 10mm, by setting the dots 'A' and 'B' we know the distance of 40mm and the software then calculated the magnification of the image. This software tool is called 'Scale Factor' and resulted in 3.962. The dot 'Origo' determined the origin of the image which is later used for the vector fields.

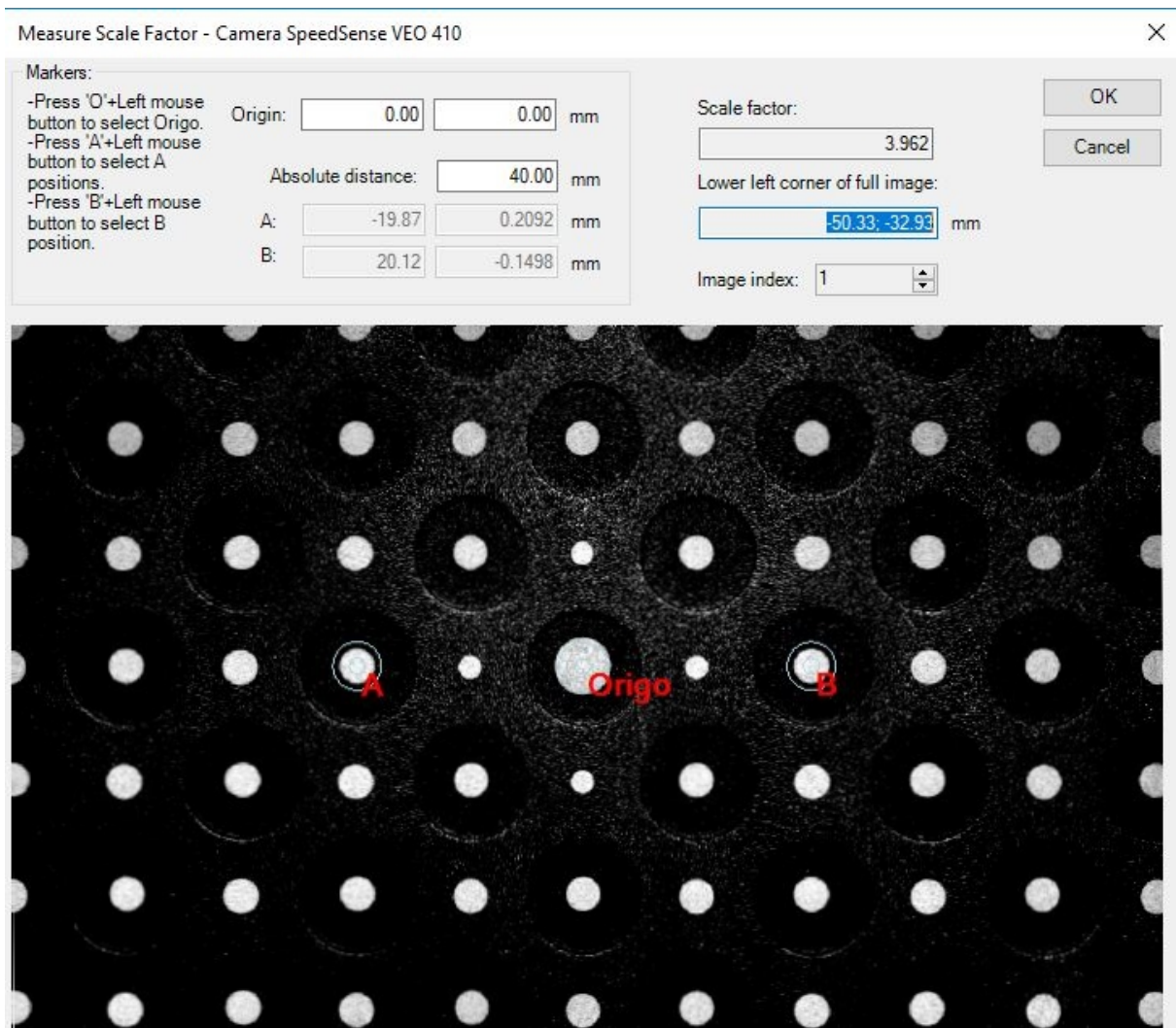


Figure 24: Measure Scale Factor for Calibration of the Camera

4.4.2.2 Acquisition

After the 'Measure Scale Factor' was calculated and the calibration accepted by the software, it was possible to run the PIV experiments. First, the laser main switch together with the pump for the coolant was activated. The Q-switching mode was set on 'TRIG' which triggered the laser now externally by the synchroniser. The laser shutter was still set on 'closed', so no light was emitted by accident. The next step was switching on the smoke generator as the electrical coil needed some minutes to heat up. Only then it was possible to switch on the pump of the generator and smoke filled the seeding box. Next, the volume air flow was set on the right values for centre and swirling air and the laser shutter was opened. From now on, it was possible to control the next steps of the experiment only from the software on the computer. By running the system in 'preview' mode all

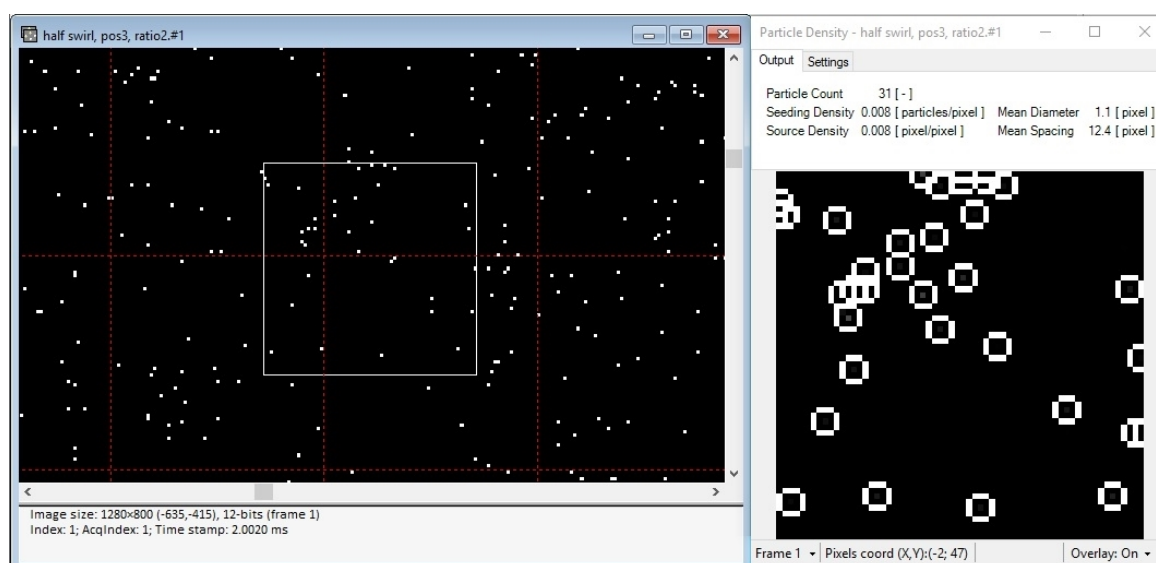


Figure 25: Particle Density in the Interrogation Windows

devices were synchronised, the laser was flashing and the trigger of the camera acquired images at the rate specified in the system control panel. In 'preview' mode, the camera did not stop acquiring images when the requested number of images was acquired, but simply overwrite the oldest image with the most recent one. The instantaneous particle flow could be seen on the screen. This mode was to adapt the camera by changing the aperture to the much brighter light of the laser compared to the LED lamp used for the calibration. The amount of smoke was also adjusted by changing the production rate of the oil pump of the smoke generator. It was important to check the particle density N_i , i.e. the number of particles in the interrogation area (IA). At least $N_i > 10$ per IA should be detected by the software. Figure 25 illustrates the preview-window and the particles detected by the software. The window on the right shows exactly the particles encircled by the white square. The red squares in the left image are the IAs. The contrast and brightness were changed in a way so that the particles are very well visible as white dots, because without the changes the image would have been considerably darker.

Once the 'preview' images were satisfying it was time for recording. The 'Acquire' function did almost exactly the same as 'preview' with the exception that it stopped recording when the requested number of images had been acquired. Table 6 shows the recording, camera and laser settings the experiments was based on. It means effectively that the camera records one double frame image every 1ms. The time between the frames is $30\mu s$. After 4000 images the laser stops automatically and for analysis it is necessary to transfer all images from the camera to the hard disk of the computer. Figure 26 shows the timing diagram with the trigger signals for the laser and the exposure of the camera over the time used for the experiments.

Recording settings	
Time between pulses (μs)	30
Trigger rate (Hz)	1000
Number of images	4000
Camera settings	
Mode (μs)	Double frame mode
Delay to open (μs)	0.2
Delay to open (μs)	0.35
Exposure time frame 1 (μs)	500.00
Laser settings	
Q-switch activation delay (μs)	5
Light pulse duration (ns)	9

Table 6: Settings for recording, camera and laser

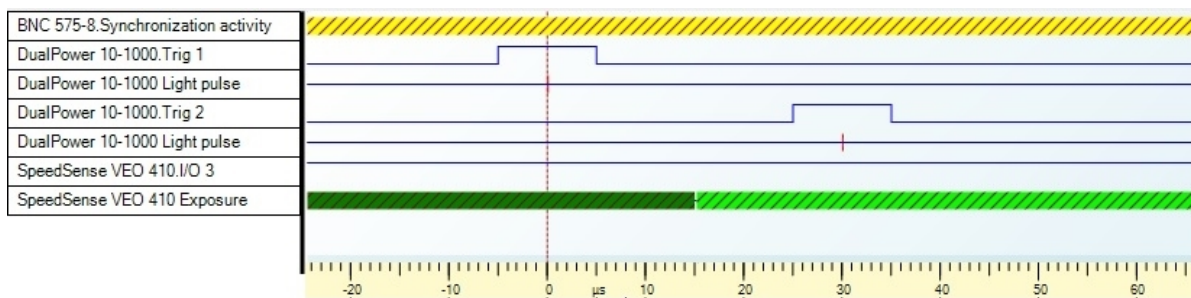


Figure 26: Timing Diagram

4.4.2.3 Analysis Sequence

Once all the images were transferred to the database, a analysis sequence was applied to all the runs to calculate the final velocity fields. The following sequence was applied to all runs:

- ⇒ Cross-Correlation
 - ⇒ Average Filter
 - ⇒ Vector Statistics
 - ⇒ Profile Plot

Cross-Correlation: First, it was necessary to estimate the size of the interrogation area. As stated in chapter 3.3.3 the in-plane movement of the particles should be below 25%. The maximum velocity calculated in chapter ?? is at the outlet of the centre tube at volume ratio 3 and 12.2m/s. With the time between pulses of $30\mu s$ this leads to following maximal displacement of a particle:

$$12.2 \frac{m}{s} * 30\mu s = 366\mu m \quad (43)$$

With an interrogation area of 32x32 pixel this accounts to a metric size of:

$$32Pix * 20 \frac{\mu m}{Pix} * 3.962 = 2,535\mu m \quad (44)$$

$20 \frac{\mu m}{Pix}$ is the size of each pixel and 3.962 the image magnification. This means that the displacement at maximum velocity is around 14% of the interrogation area. This is according to literature [23, 34] an optimal value for PIV.

Furthermore, the cross-correlation was done with 50% overlap on all four lateral edges on each IAs. The motivation behind this method is increased quality of result because the particle pairs near edges usually contribute less to the outcome. With the help of the overlaps between adjacent interrogation areas, these pairs contribute to the result and lead to a better accuracy. The downside of this method was the notable longer calculation time.

Average Filter: This method filters and smooths the vector maps calculated by the cross-correlation. A weighted arithmetic averaging inside a defined area was applied to every vector on each of the 4000 vector maps. For this experiment the area size was chosen as 3x3 pixel and the result showed vector maps with clearly less spurious vectors.

Vector Statistics: As indicated by the name, this method calculates different statistics for multiple vector maps. For this experiment, the method calculated the mean velocity vector map out of the 4000 vector maps which will be seen in the result chapter 5.2.

Profile Plot: The last step of the analysis sequence is the profile plot method. It allows to draw an arbitrary line across the mean vector map and extract the value along this line. This method was used for the velocity along a horizontal line in chapter 4.4.3 and along a vertical line in chapter 5.2.

4.4.3 Validation

Before starting with the experiments, a validation of the whole PIV system was necessary. By running several tests with the exact same settings it was possible to predict the reproducibility of the system. As the trigger frequency of the laser was already at the lowest available value of 1000Hz, it was not possible any more to extend the time interval between the images. The only chance to prolong the recording time was to increase the number of images. The following graphs in Figure 27 show the velocity over a horizontal line 5cm after the outlet for three different recording settings. They were all taken for the same swirl number, same camera and laser setting and same outlet position. The only difference was the number of images recorded. The top diagram shows the graphs for tests with 500, 1000 and 4000 images. For 500 images, with the laser trigger at 1000Hz, this means 0.5s recording time. The figure also shows that at only 4000 images recorded, the deviation has an acceptable dimension. As one image takes around 4000kB this means around 16GB data storage is required for one run of 4000 images. It has to be said at this place that a longer recording time would probably improve the quality of the experiments but due to the limited storage on the camera, the extensive time to transfer the images from the camera to the computer and also the time for post-processing this high amount of images, it was recommended to run the experiment with 4000 images. The maximal deviation for 4000 images occurred at 14mm on the x-axis. The mean value at this position was 0.848 with 0.049 being the largest deviation at 5.78%. This is the reason for the error which still occurred for each run and the little 'jumps' between the different positions in the result chapter. An improvement of the deviation and more accurate results would require a longer recording time of the flow. This can be either achieved with a laser which has a trigger frequency below 1000Hz or more recorded images. Although the camera has a storage limit and the question, the question would still arise if the very long time of post-processing due to the larger number of images would justify the outcome.

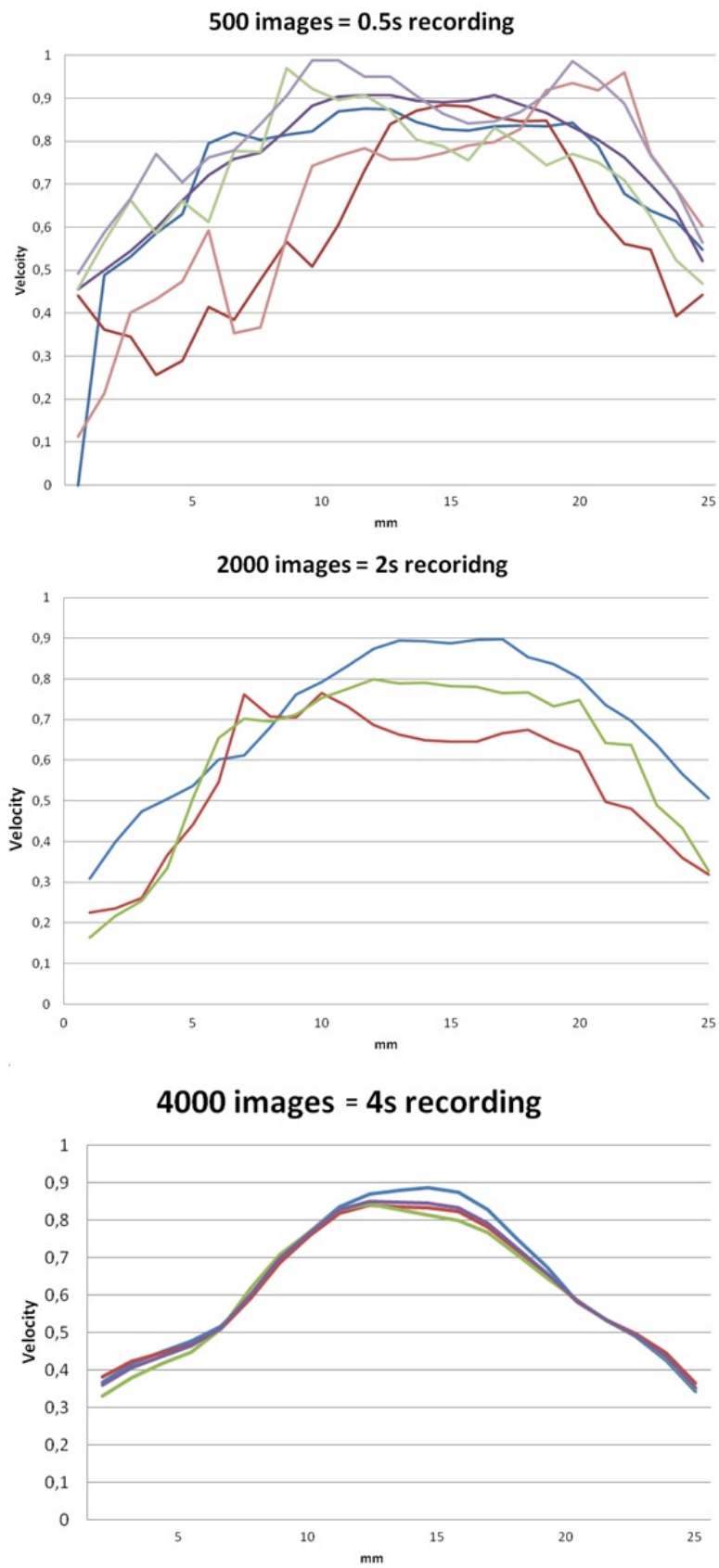


Figure 27: PIV reproducibility tests with 500, 2000 and 4000 images

5 Results

5.1 CFD Results

5.1.1 Velocity Fields

Figure 28 shows the velocity magnitude profiles generated by the CFD simulation for the three different swirler settings: no, half and full swirl. In exact terms, it is the velocity on the plane located in the centre of the combustion chamber. Most noticeable is the reduced length of the flow pattern. Especially the change from half swirl to full swirl varies considerably with a smaller shift between no and half swirl. The no-swirl jet reaches a length of approximately 40cm and the half-swirl jet around 33cm. Both have in common that the velocity pattern stops rather abruptly. This is not the case for the full-swirl setup which shows a slower reduction. Therefore, it makes no sense to identify a certain flow length in this case. A more valid comparison regarding the flow length has been made in figure 29 where the axial velocity of all swirl-setups is analysed. In contrast to the length of the velocity field which reduces with a higher swirl number, the width increases. This effect can be better seen in the next figure 29 or in chapter 5.1.2 showing the radial velocity distributions.

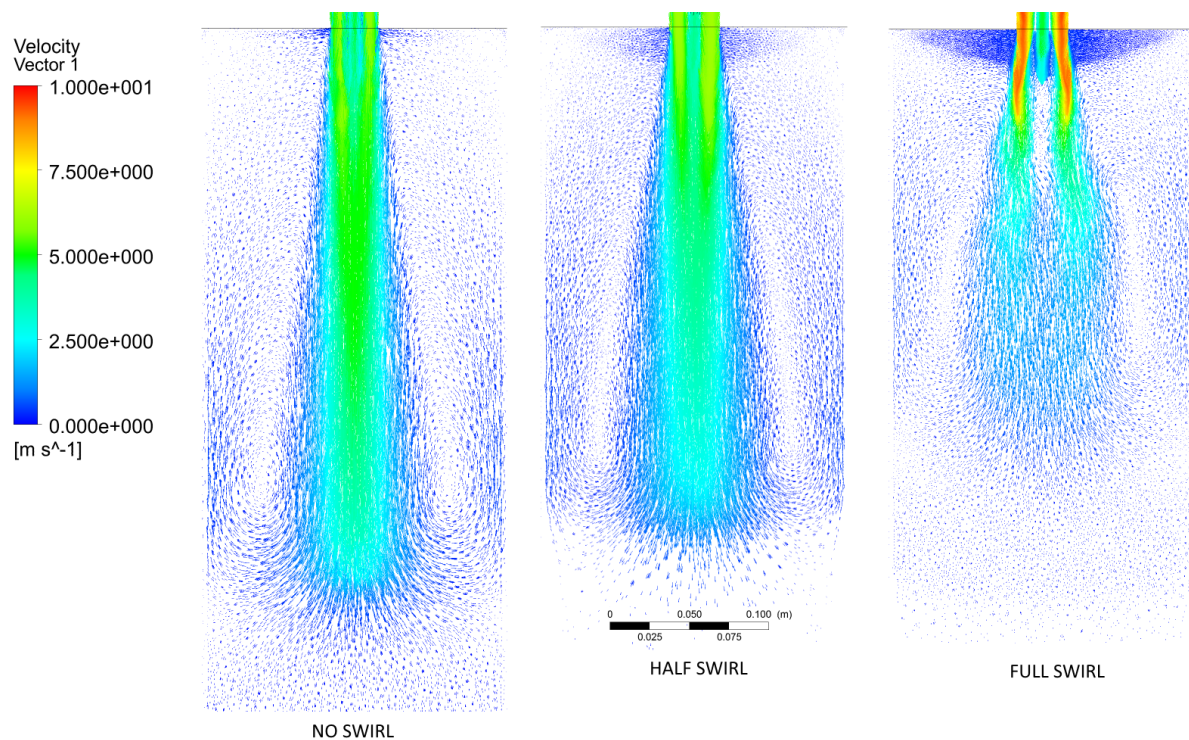


Figure 28: Velocity Fields for No, Half and Full Swirl

Figure 29 shows the velocity profiles of the tube for different positions in the centre after the nozzle exit. The first horizontal line is 3cm after the nozzle exit with the following lines each at 5cm distance. The figure displays in a detailed way the progress of size and shape of the velocity. Compared to figure 28 it illustrates very well the spread of the velocity field: the more the swirl number increases, the more the width grows. It also dissipates a lot faster for higher swirl.

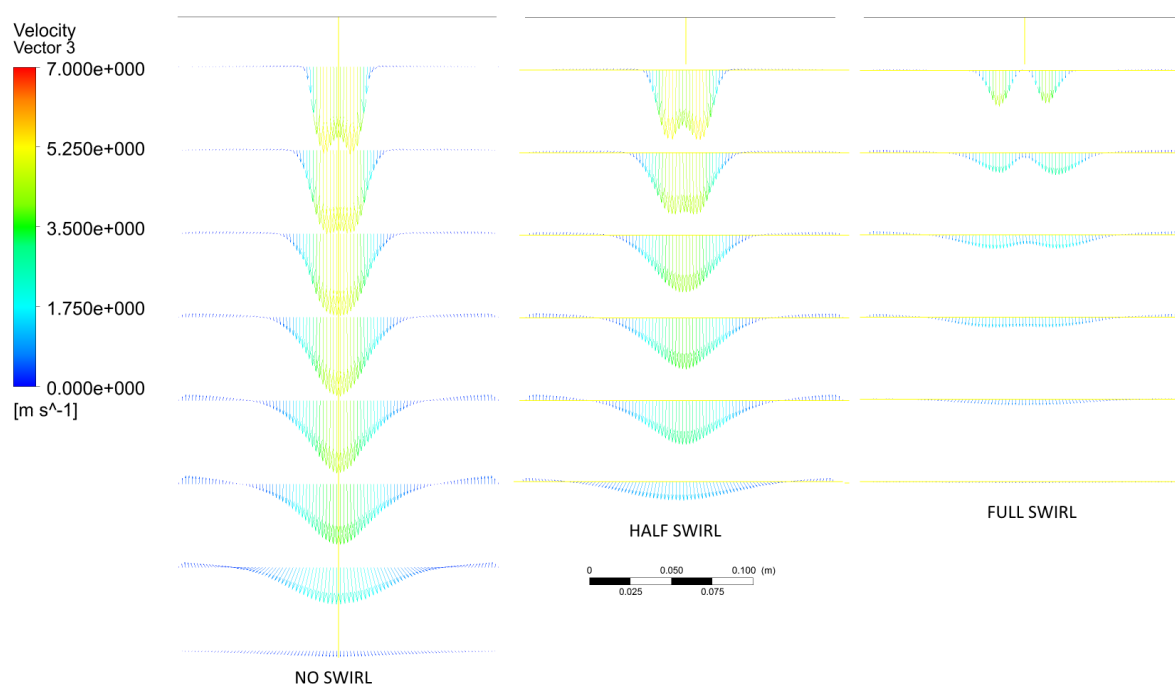


Figure 29: Velocity Profile at different Positions after the exit for No, Half and Full Swirl

5.1.2 Radial Velocity

Figures 30 and 31 display the radial velocity field in the combustion chamber using different positions. The full-swirl setup is on the left side of the images and the half-swirl on the right side. The circular planes are of the same diameter as the combustion chamber and are set every 5cm after the nozzle exit. The figures demonstrate that the velocity at full swirl located already 5cm after the exit is significantly higher than the half swirl setup. At 10cm after the exit, the full swirl velocity profile has a peculiar shape as it is not a circular form as expected. This phenomenon does not appear for the half swirl setup and also vanishes for the following positions. A reason for this effect could be the $k-\epsilon$ model which to a good extent is able to compute swirling flows. However, due to restrictions and assumptions, it is limited in certain calculation procedures which can cause this anomaly. At the position 10cm after the exit the full swirling vortex reaches around 10cm in diameter, whereas the half swirling vortex has a diameter of 5.5cm. Figure 28 shows that the half swirl setup has a much longer velocity field. This is also the case for

the radial velocity, because at 20cm after the exit it shows - in opposite to the full swirl setup - still a noticeable swirling motion.

The exact velocity distribution at every position is illustrated in figure 32. It shows the velocity magnitude of the two radial axes at different positions in the tube. On the left side is the full swirl setup, on the right side the half swirl setup. At 5cm after the nozzle exit, the full-swirling velocity is 40% higher than the one in the half swirl setup at 1cm radial distance. The longer radial distance and the higher velocity are also noticeable for the following positions although to a smaller extent. At the position 20cm after the outlet, the velocity at the full swirl setup is only 21% bigger than for half swirl. For 25cm, the radial size and the velocity have inverted and are now larger for the half swirl setup.

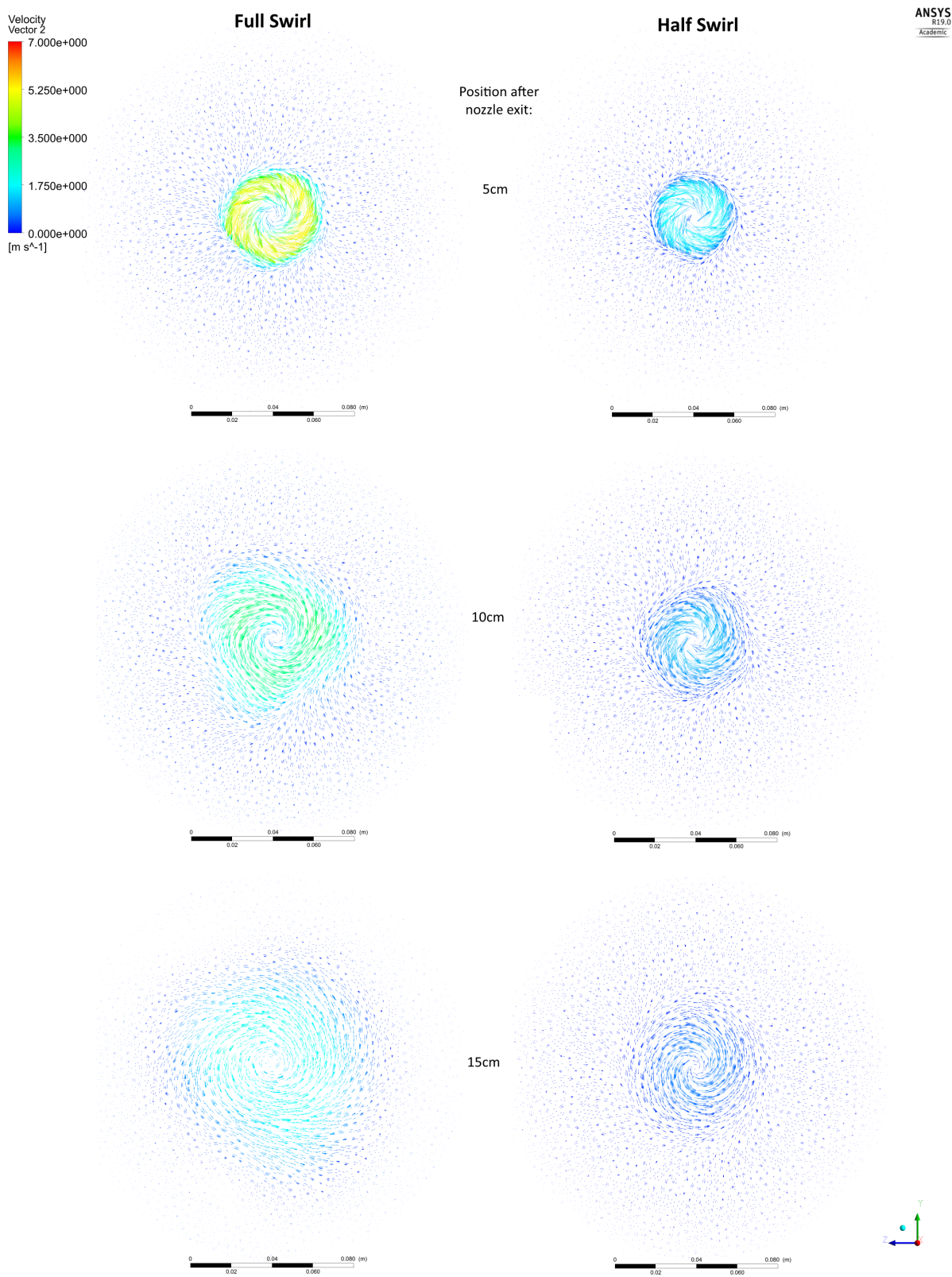


Figure 30: Radial Velocity at different Positions after the exit for Half and Full Swirl

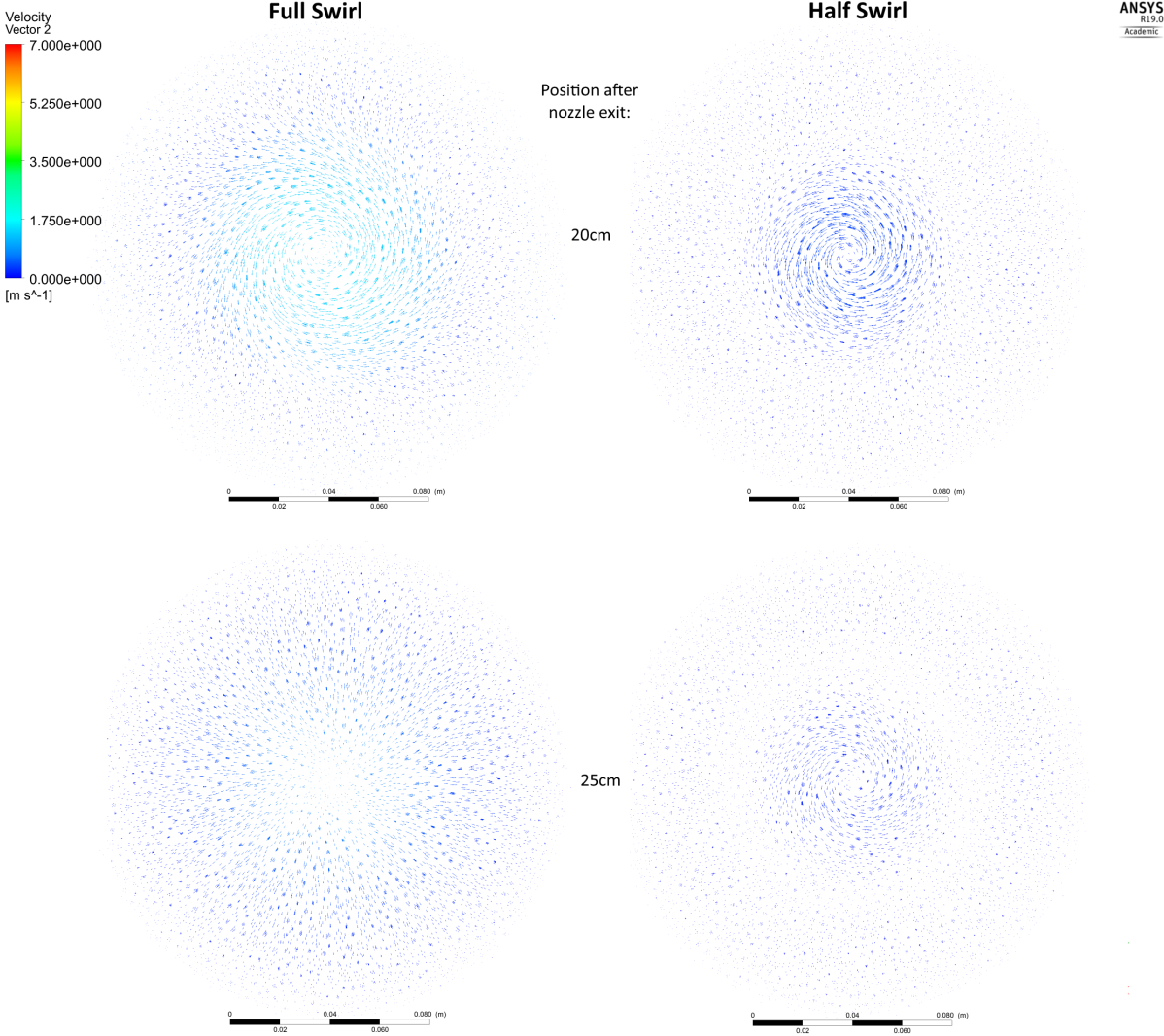


Figure 31: Radial Velocity at different Positions after the exit for Half and Full Swirl

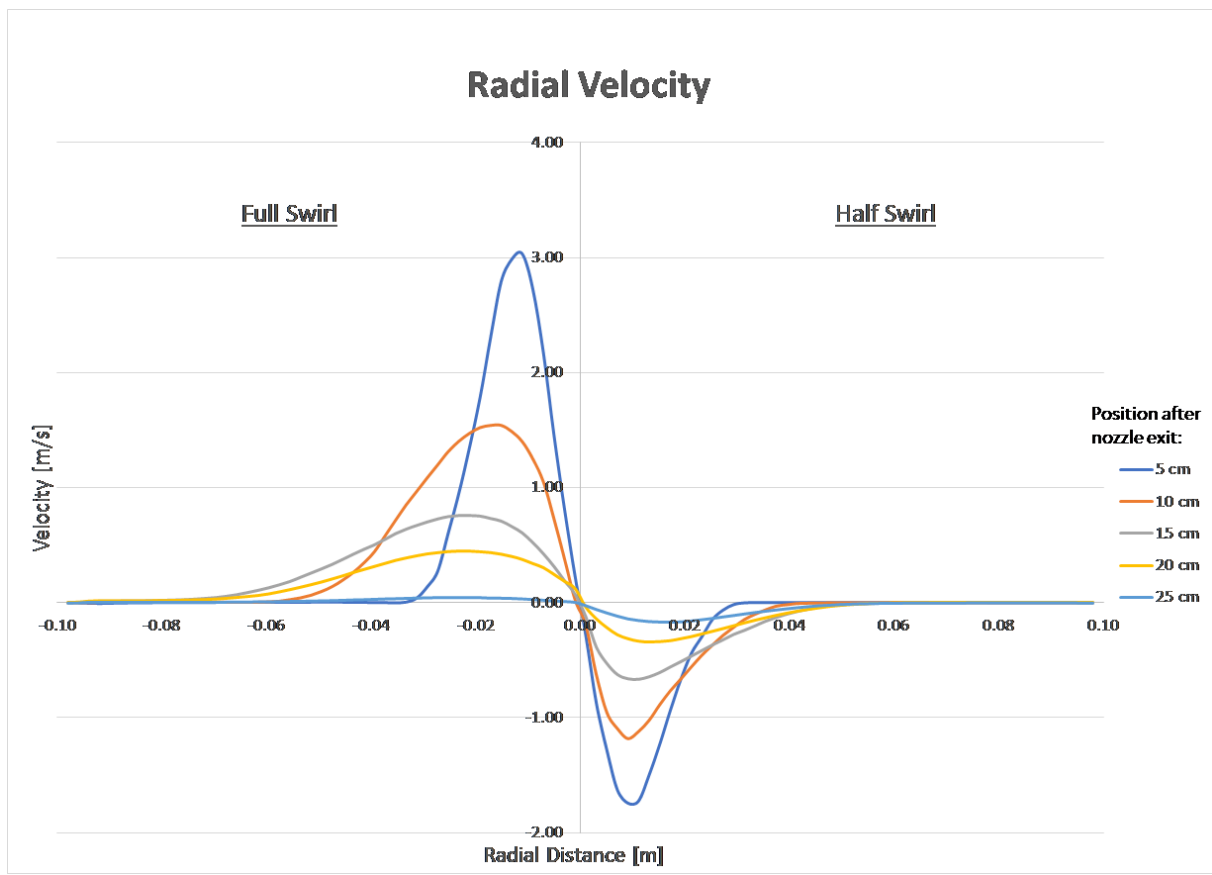


Figure 32: Radial Velocity Distribution at different Positions after the exit for Full and Half Swirl

5.2 PIV Results

This chapter not only presents the results obtained by the PIV experiments but also includes the obstacles and challenges faced during the experiments. As they mostly occur in different ways for each swirl setup, it is best to include and discuss these problems in their respective chapter. The size of the following velocity vector fields is 21cm in height and 10.5cm in width.

5.2.1 No Swirl

The main challenge for the no-swirl setup was the very low dispersion of the smoke particles especially for the first position. This effect is shown in figure 33 where it is also recognisable in the resulting vector fields. Before describing the problem it is advantageous to first describe the image: Figure 33 displays three different flow regimes: The smoke jet in the middle coming from the centre tube is very dense and the dispersion of the particles is very low. On each side of the centre jet is the outer 'swirling'-air which in this setup is not swirling. The air is not seeded with smoke and therefore dark. Next to the 'swirling' stream particles can be seen. These particles are useless 'noise' without any specific flow direction, because the smoke particles are not leaving the glass tube immediately. Instead most of them flow back along the edge of the glass tube and are slowly filling the tube.

The effect of the low dispersion of the seeded centre air occurs primarily for the no-swirl setup and most notably for higher velocity ratios (VR), ratio 2 and especially ratio 3, as they have higher velocities and therefore the dispersion is even worse. VR 1 & 4 have lower velocities and single particles can be detected more easily. Modifications such as changing the image recording settings, the image depiction or a different aperture did not solve the issue. One method which helped, was to move the camera closer. By reducing the distance to the laser sheet by one third to the original distance, single particles could be seen already 1cm after the outlet. The big drawback was the considerable reduction of the size of the recorded image. This would have meant an intolerable reduction of image- and flow field width and therefore was eventually discarded. Nevertheless, the software can detect and calculate the particle displacement even in a very low dispersed smoke jet as seen in figure 33. Especially the occurrence of 'smoke clouds', small areas of dispersed particles in the flow, can easily be detected by the software. Comparing the displacement of the smoke clouds to the displacement of the rest of the particles inside the jet helped to verify the outcome. It became obvious that the further away from the outlet, the better the dispersion got and it was not an issue anymore for position 2 and 3. As already mentioned above, the problem of the low dispersion also occurred mainly for the no-swirl setup and even inverted for the full-swirl setup as particles got dispersed too quickly due to the swirling air.

Figure 34 to 37 show the velocity fields for the no-swirl setup for the velocity ratios 1-4. Each figure exists of three images merged together for the three positions. To allow for a better comparison the velocity magnitude map had the same values for every veloc-

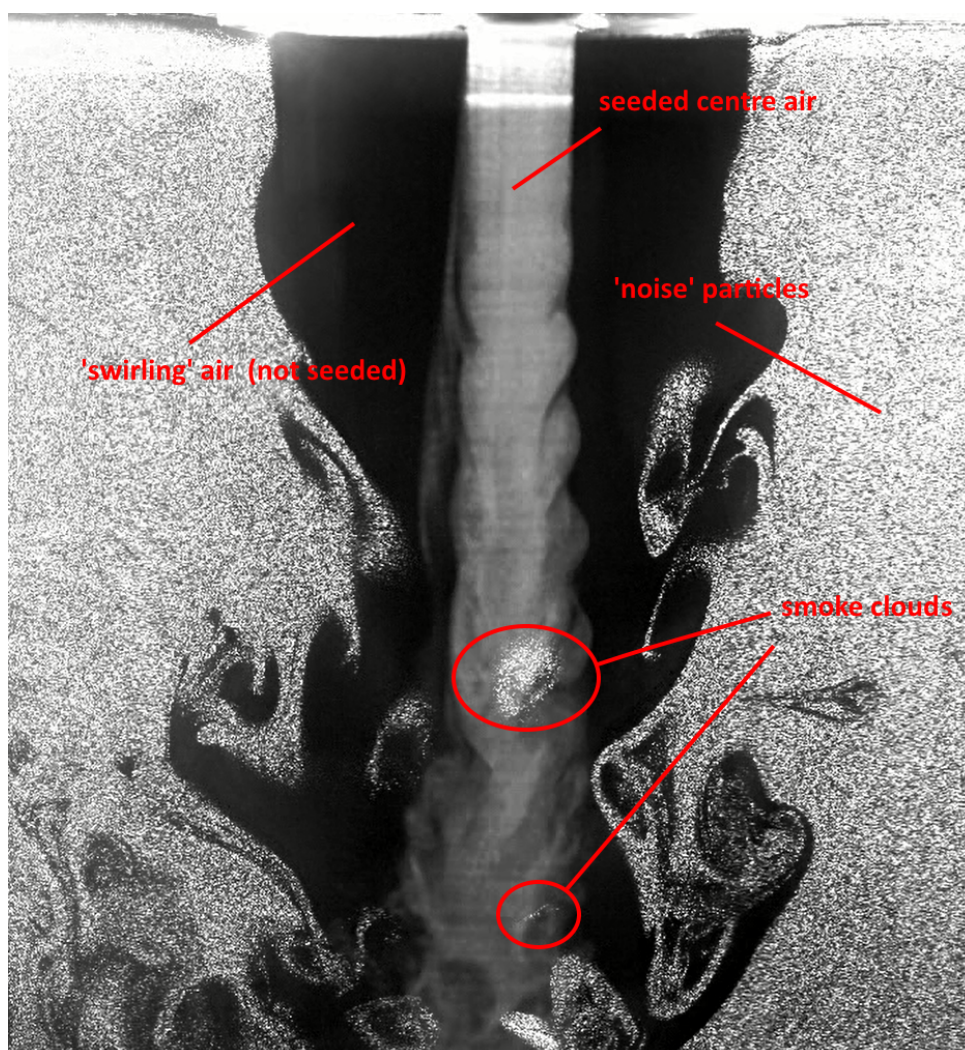


Figure 33: No Swirl Image for Ratio 3 and 1st Position

ity ratio. As stated and described in chapter 4.3.3, there is still a relatively small error between each run. This is the reason for the little but considerable 'jump' of the velocity field between adjacent positions. This effect is present for all velocity fields and all swirl setups. The reason for this has already been discussed in chapter 4.3.3 and suggestions to counteract this issue will be stated in chapter 6.

The resulting vectors just after the outlet are mostly not correct and point in almost every direction. The reason is described above and can be seen in figure 33 as the smoke particles are not dispersed and the software cannot detect correct particle displacement between two images. Furthermore, the white 'holes' at the top are also noticeable. This is due to the not-seeded, swirling air where the software cannot detect any particles. 1-2cm behind the outlet this problem does not occur anymore and the vectors are calculated out of useful and true particle displacements. Also, the vectors outside the main jet are for

some positions (e.g. figure 34 1st Position or 36 Position 3) not based on true particle displacements and point in different directions, too. The reason for this is wrong cross-correlation of 'noise'-particles which results in wrong vectors. It would have been possible to exclude them but it was decided against it. An effect which affected the amount of 'noise' particles was the time between switching on the pump of the smoke generator and acquiring the images. The longer the time the more particles filled the glass tube. However, this would not have any effect on the main jet in the middle.

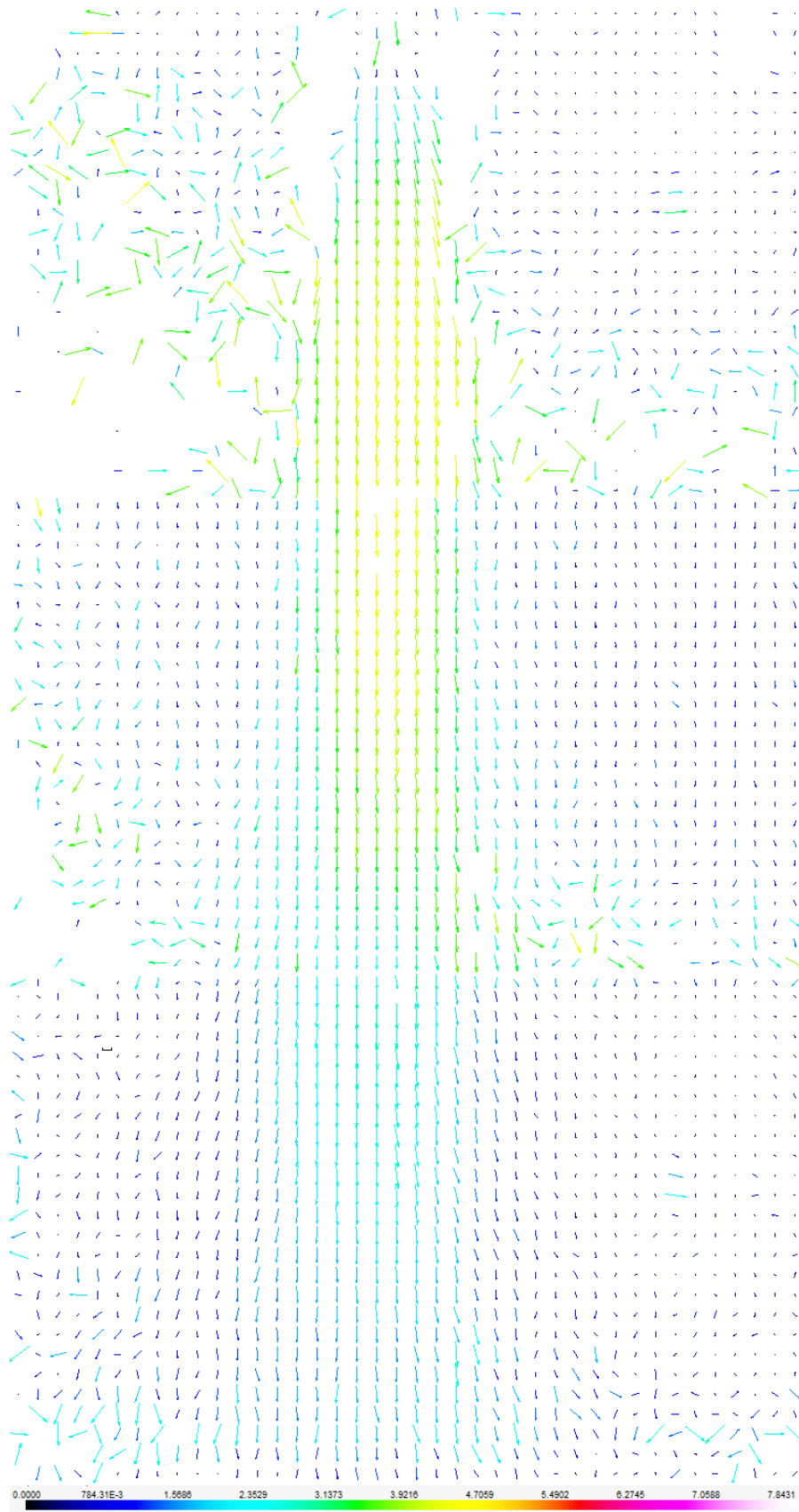


Figure 34: Velocity Field for No Swirl and Velocity Ratio 1

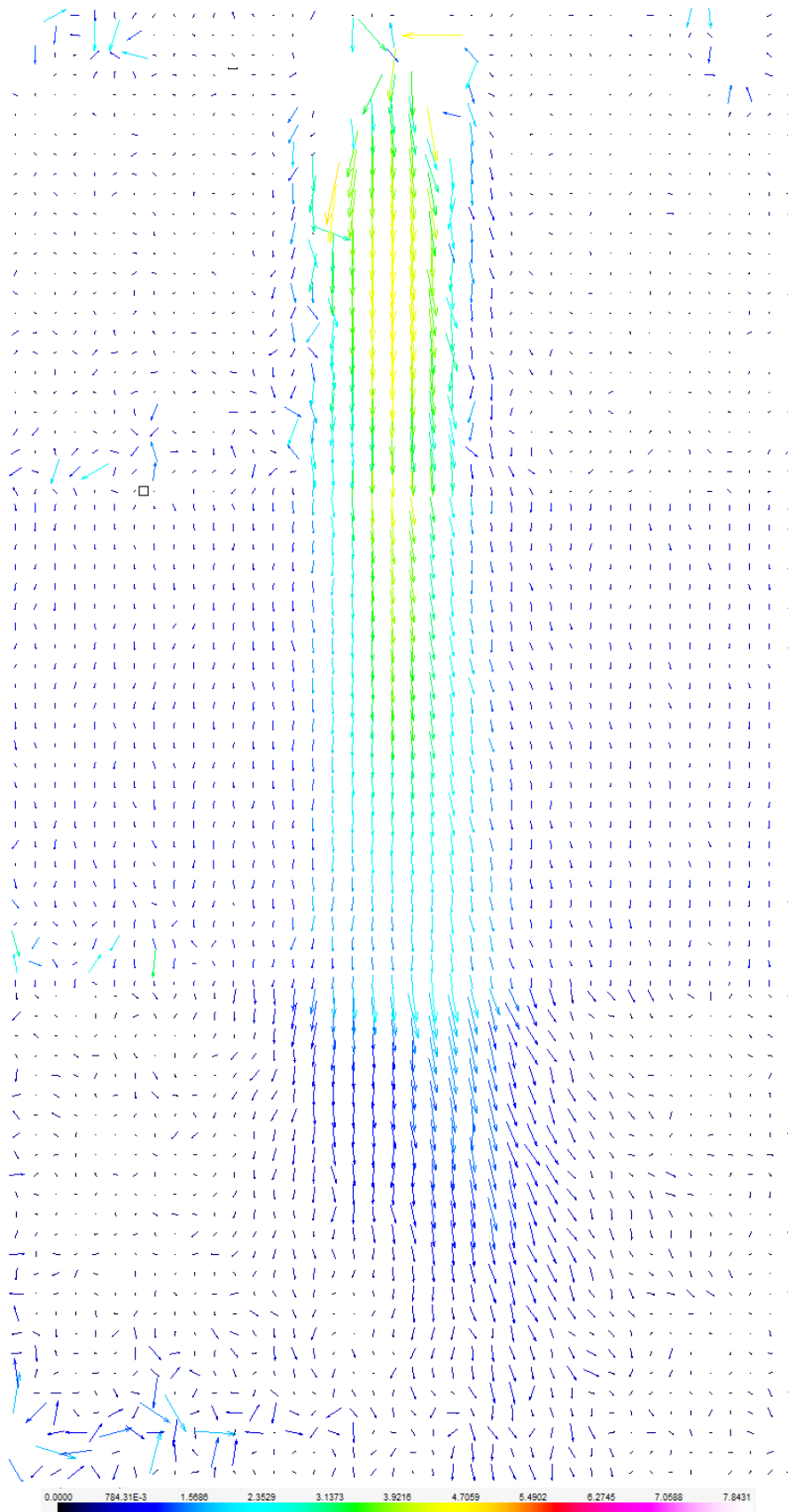


Figure 35: Velocity Field for No Swirl and Velocity Ratio 2

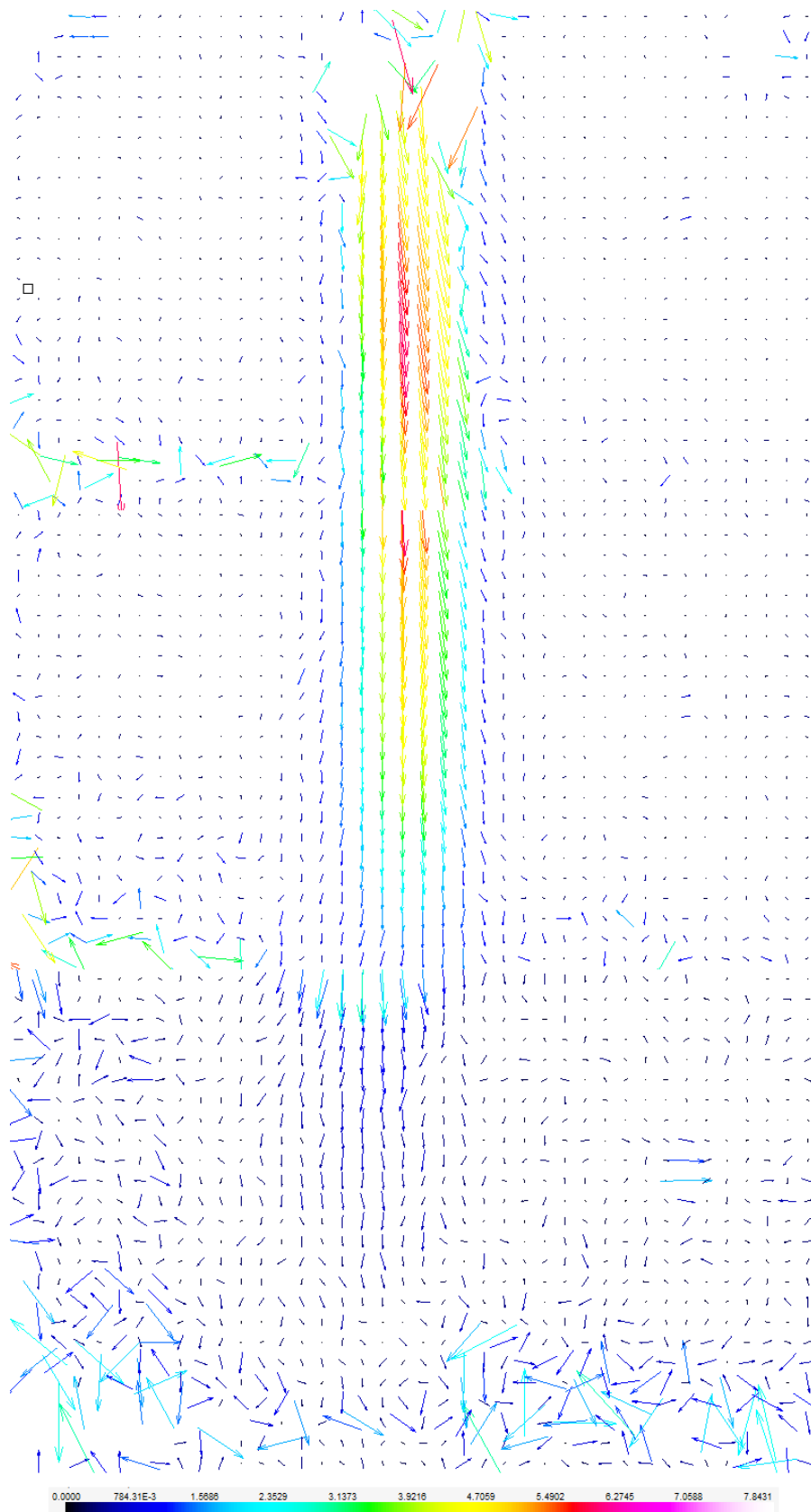


Figure 36: Velocity Field for No Swirl and Velocity Ratio 3

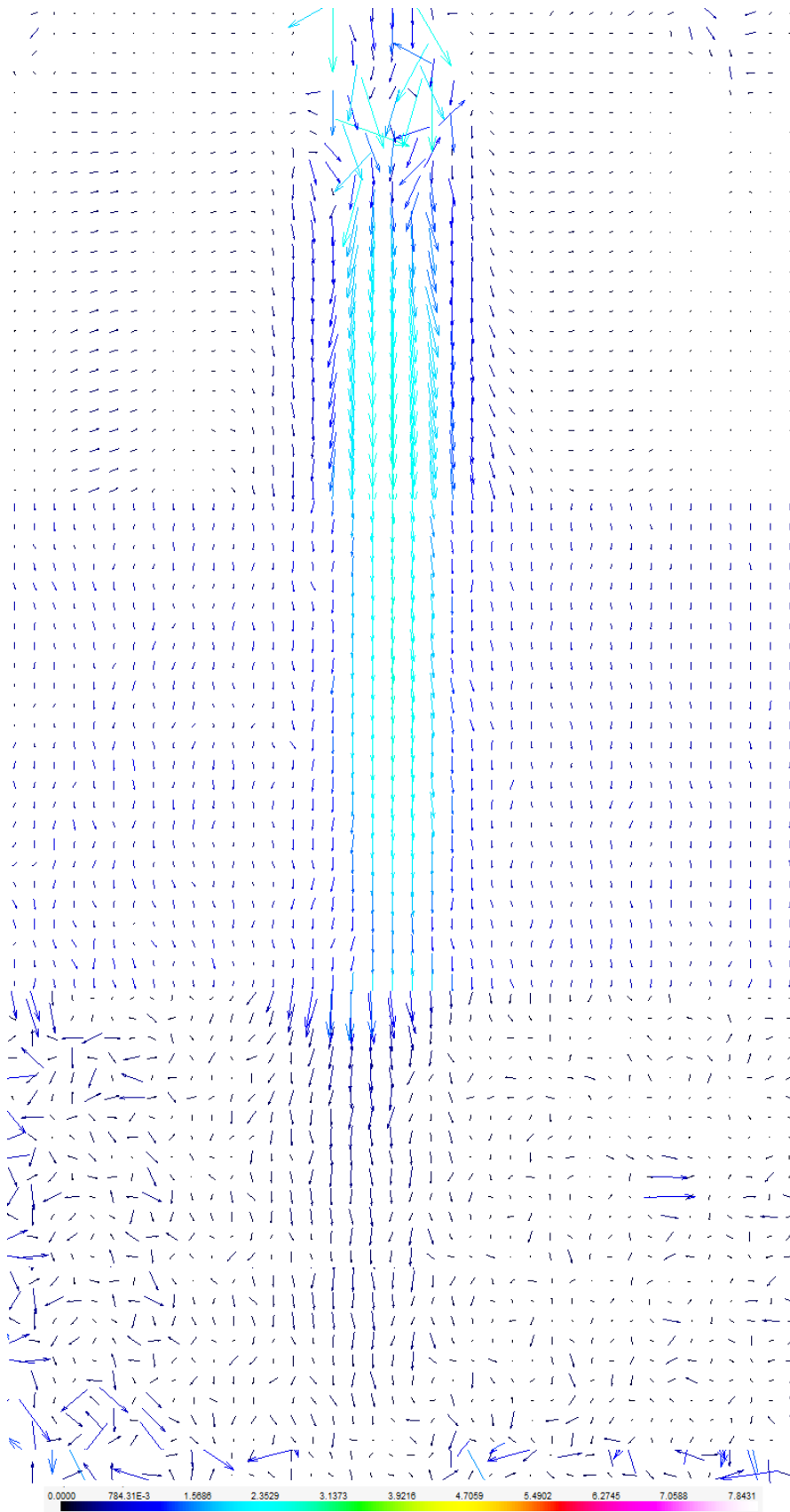


Figure 37: Velocity Field for No Swirl and Velocity Ratio 4

5.2.2 Half Swirl

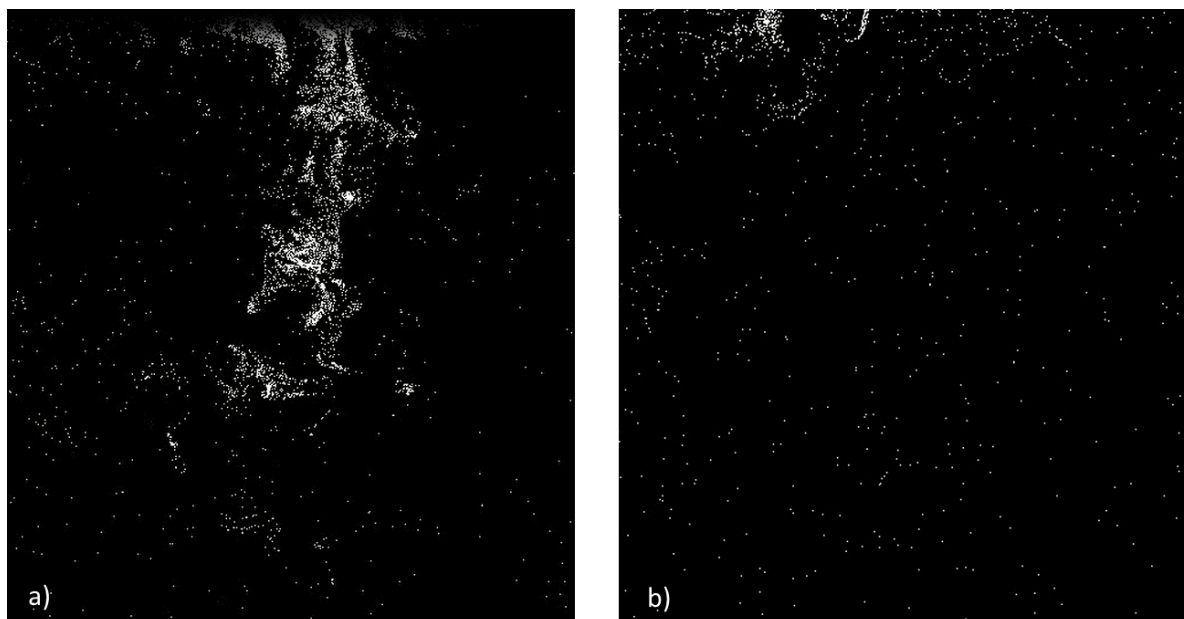


Figure 38: Smoke vortices for two different time points a) and b) at Position 3

Figure 38 shows another issue we faced during the experiments: Pictures a) and b) were taken at two different moments during the same run. The image position for both pictures is the same. Picture a) shows smoke vortices with a high number of particles in a downward movement. In picture b) there are no vortices and the displayed particles are mostly considered 'noise'. During the run it could have happened that no smoke vortices reach the lowest position 3. Due to the turbulence, the vortices appear and evolve randomly. If during the 4 seconds acquiring time no or only one or two of these vortices reached position 3, the resulting vectors would have been wrong or amiss. The experiments show that the higher the swirl and the slower the centre air, the shorter the vortices travel. The result of this effect can be seen in the figures 39 and 42 as only position 1 and 2 exists. For position 3, no significant particle movement was recorded. A possibility to include more flow vortices is to extend the recording duration. Yet, this option was discarded as already stated in chapter 4.4.3.

Figures 39 to 42 show the resulting vector fields for the half-swirl setup. For a better comparison the velocity magnitude map is the same as for the no-swirl setup. The much shorter length of the velocity field compared to the no-swirl experiments is noticeable. Furthermore, the slight left sided drift of the vector field for VR 1,2 and 4 is striking. This phenomenon occurred only for the half-swirl setup and intensified for lower velocities. It was even visible with the naked eye. However, it was not possible to find a trigger for this effect, a possible explanation could be a manufacture inaccuracy of the swirler components by the workshop. This would require further testing in future experiments.

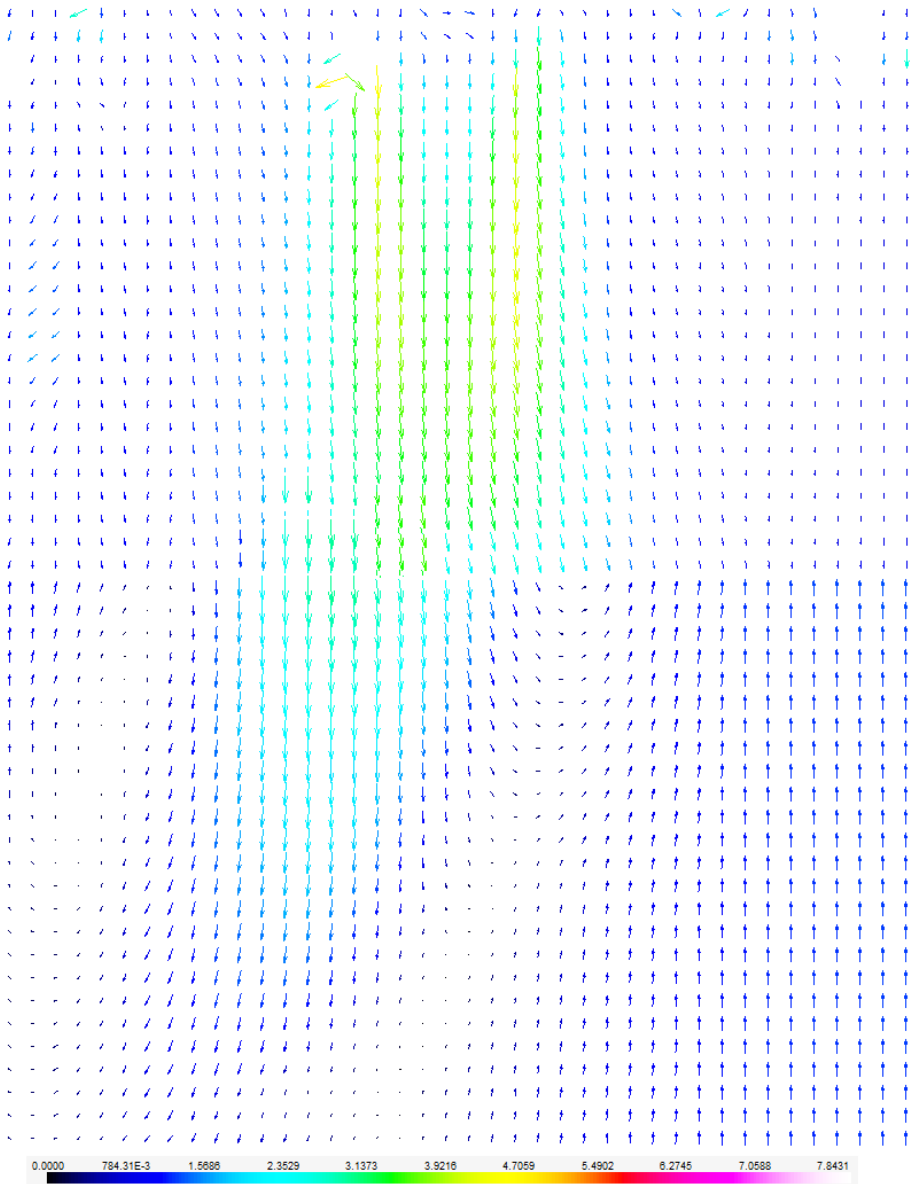


Figure 39: Velocity Field for Half Swirl and Velocity Ratio 1

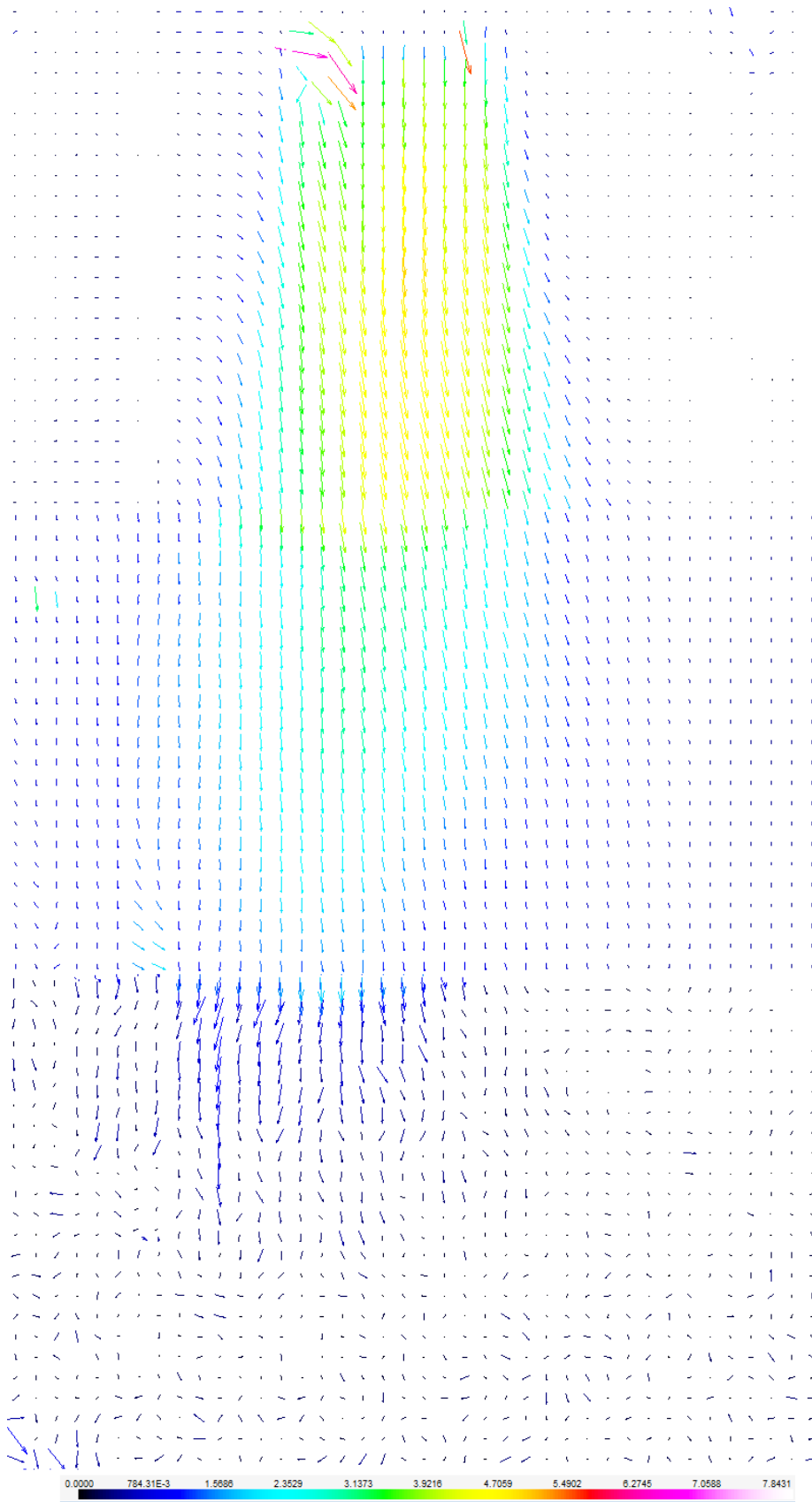


Figure 40: Velocity Field for Half Swirl and Velocity Ratio 2

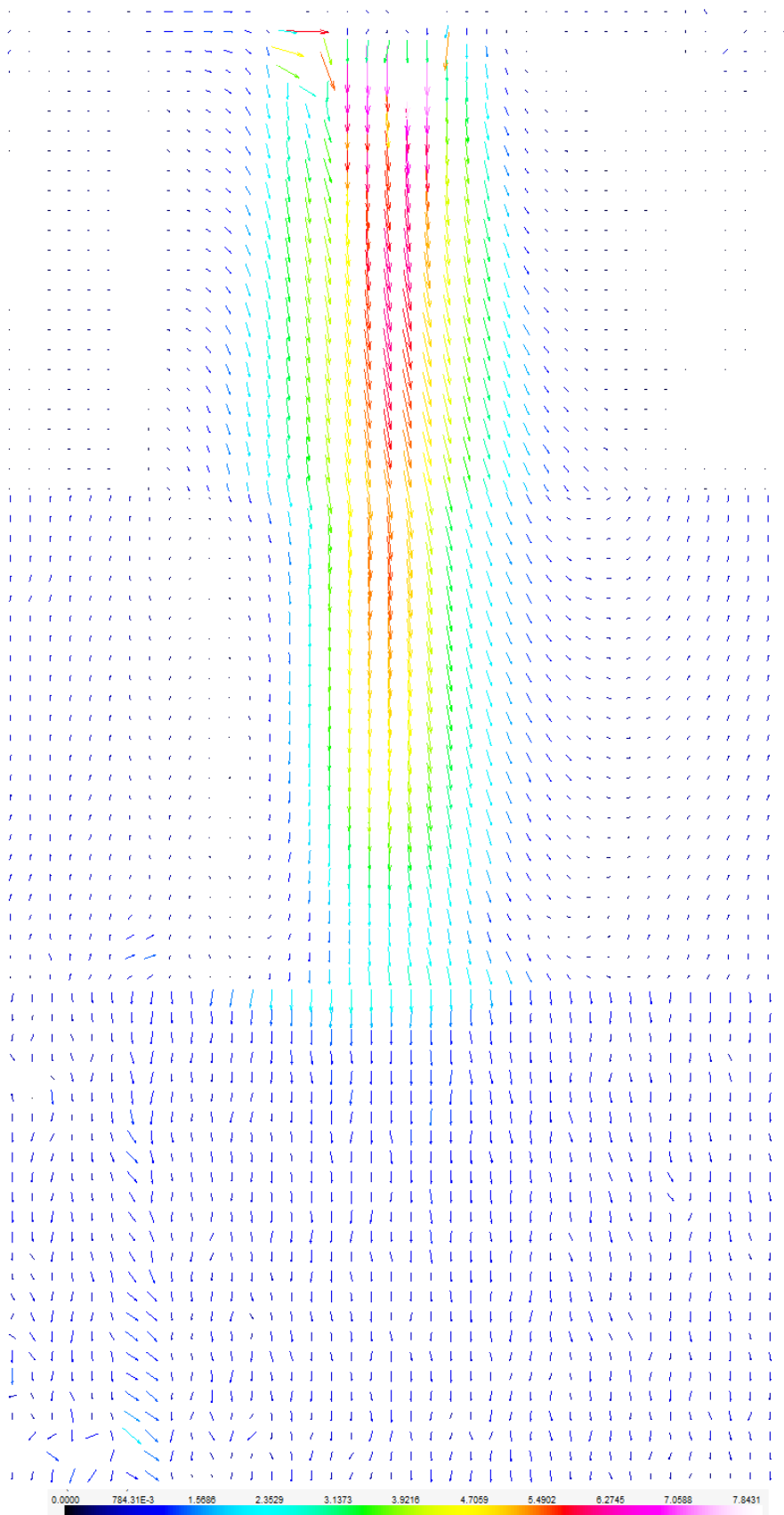


Figure 41: Velocity Field for Half Swirl and Velocity Ratio 3

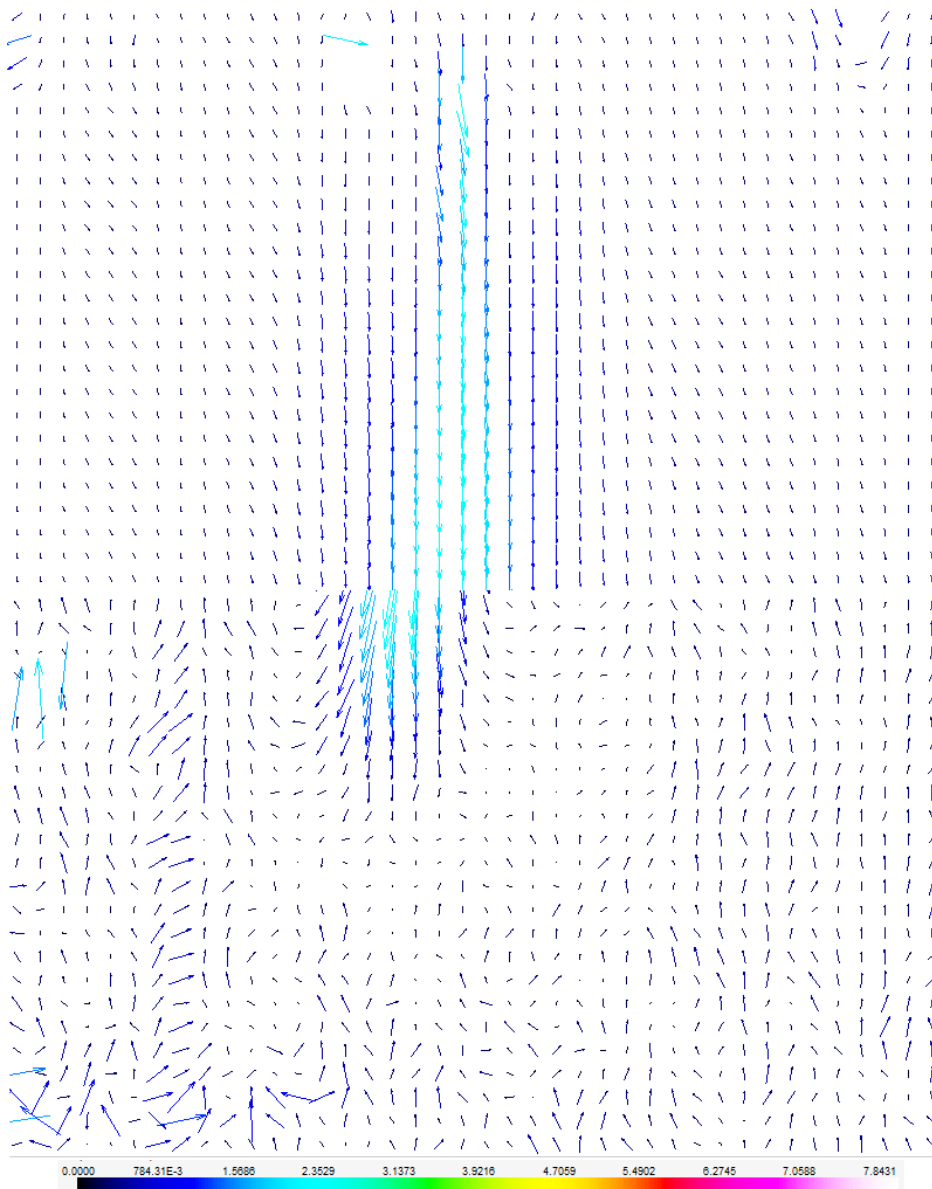


Figure 42: Velocity Field for Half Swirl and Velocity Ratio 4

5.2.3 Full Swirl

For the full-swirl setup, it was very difficult to obtain a meaningful and correct velocity field. The issue for the no-swirl measurements, that the smoke did not disperse properly, now inverted for the full-swirl setup. This was mainly due to the high amount of turbulent, swirling air which spread and dispersed the smoke particles almost immediately after the smoke left the centre tube. Figure 43 shows a typical particle distribution for the full-swirl setup. On the upper part of the image the centre tube can be seen in the middle with the outer tube around it. The bright white areas on the left and right side of the image are screws which are illuminated by the laser. The smoke vortices leaving the centre tube vanish already at around 2-3cm distance to the outlet. Inside this region the flow is highly turbulent and no real flow pattern of the particles is recognisable. The almost chaotic movement of particles during two frames makes the calculation of the displacement very difficult for the software. The highly swirling radial air coming from the outer tube rapidly takes away the axial movement of the smoke particles and turns it into a radial movement. It basically means that the particles also shift from an in-plane flow to an out-of-plane flow. This implies that the movement of the particles turns out of the plane of the laser sheet and particles can leave the illuminated area. Correct cross-correlation of particle pairs under these circumstances is very complex and intricate.

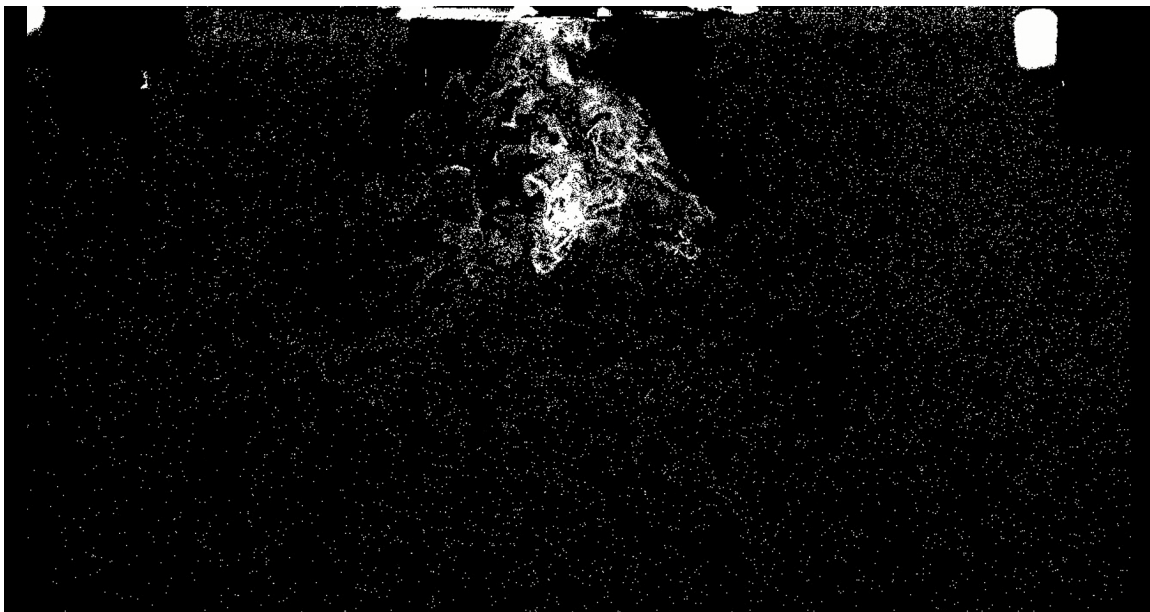


Figure 43: Smoke particles for the Full-Swirl Setup

Furthermore, the particles of figure 43 already show a relative strong movement to the right. This effect strongly reflects in the resulting vector fields in the following figures 44 to 47, especially for VRs 2 and 3. Due to the chaotic movement the averaged velocity fields for the lower velocities of VRs 1 and 4 also show very low magnitudes. The velocity fields for velocity ratios 2 and 3 have a more distinct pattern but turn immediately to the right.

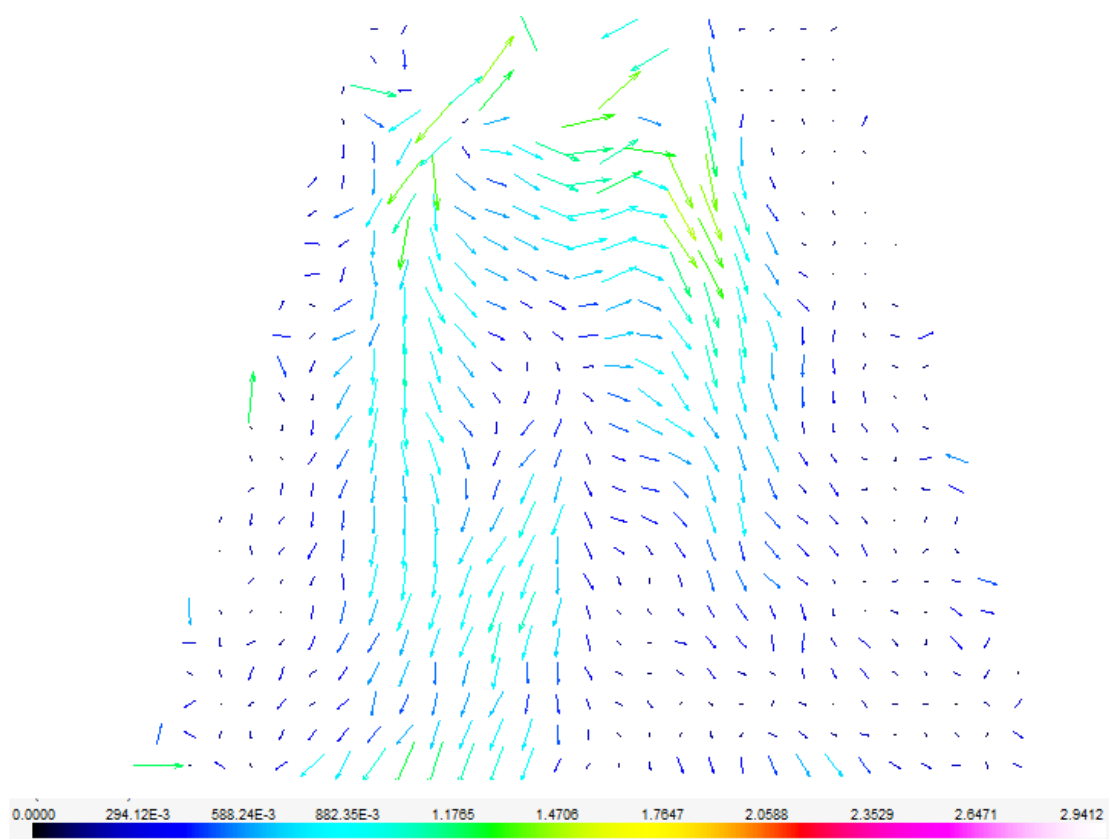


Figure 44: Velocity Field for Full Swirl and Velocity Ratio 1

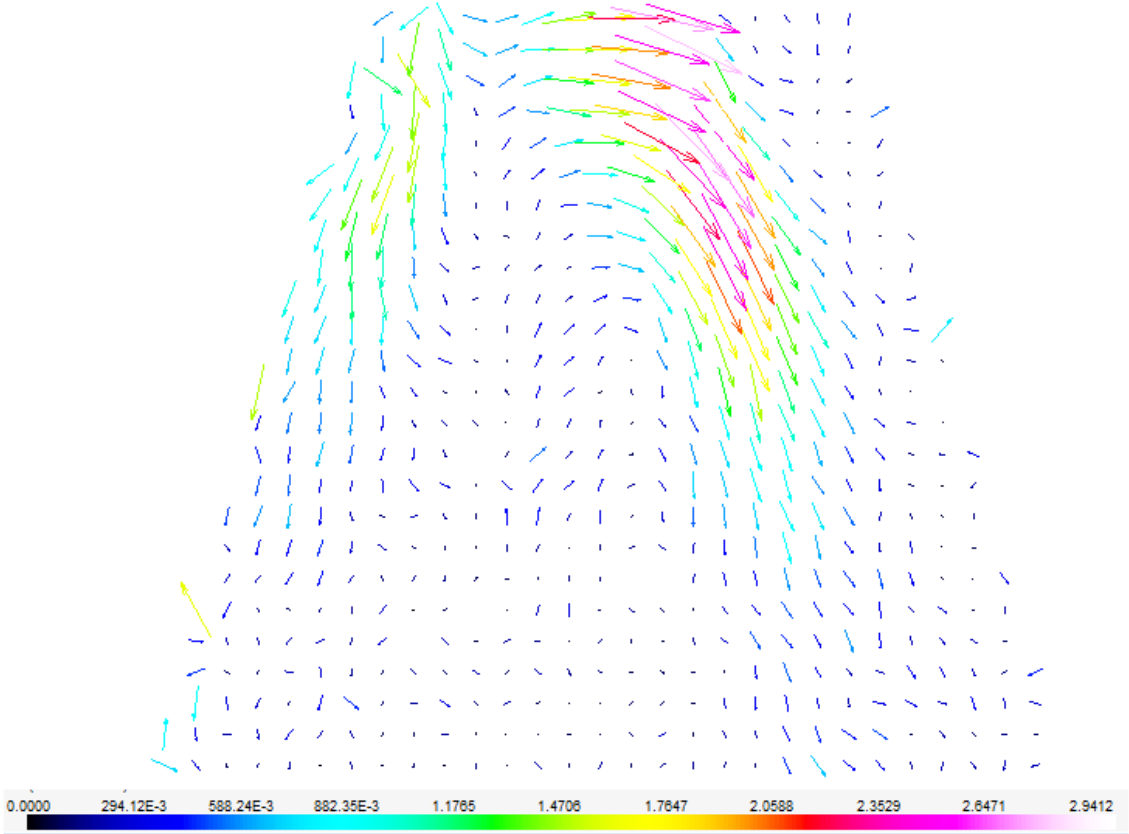


Figure 45: Velocity Field for Full Swirl and Velocity Ratio 2

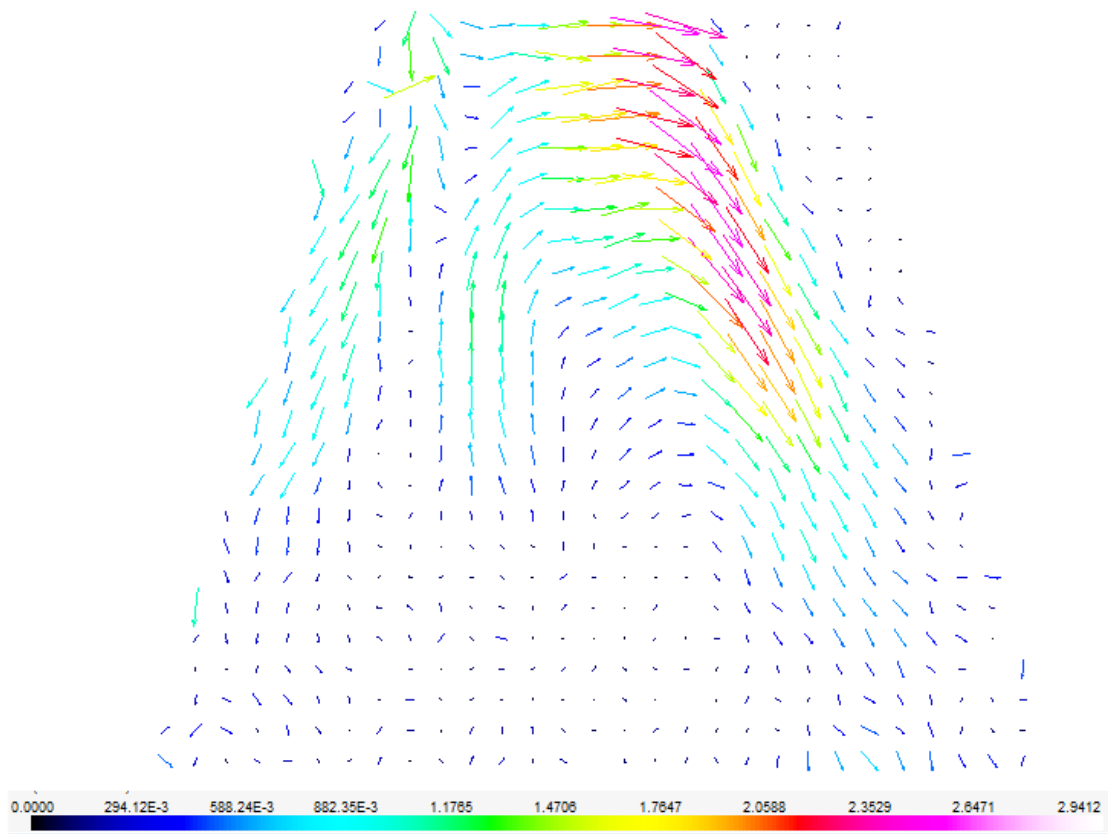


Figure 46: Velocity Field for Full Swirl and Velocity Ratio 3

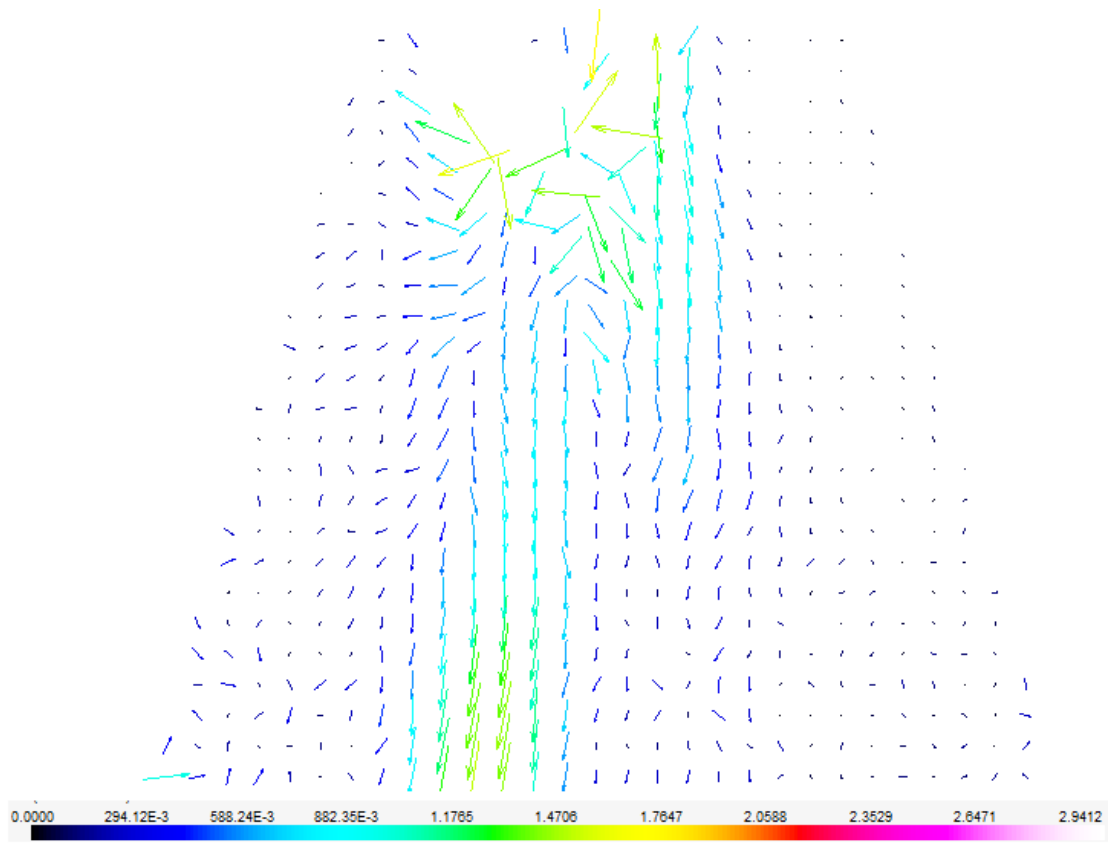


Figure 47: Velocity Field for Full Swirl and Velocity Ratio 4

5.3 Comparison of CFD and PIV Results

The comparison of the results of the CFD simulation and the PIV experiments is a part which evolved during the process of this thesis. As the construction and setup of the PIV experiment took longer than expected the focus was split and a numerical simulation was taken into account. The question regarding the comparison of CFD and PIV came up pretty early in the progress and a few possibilities were considered. One option would have been the simulation of multi-phase CFD simulation. The smoke particles would have been included as a second phase to the simulation. This would have allowed an almost accurate and close comparison. However, due to time limitations and lacking knowledge on multi-phase simulation this option was discarded. Especially turbulent multi-phase CFD simulation requires long-term experience and particular know-how which cannot be achieved during the process of a master thesis. Another option to compare the velocity fields was the idea to also seed the swirling air, coming from the outer tube during the PIV experiments. However, the smoke was so finely dispersed that it was not possible to detect single particles. The dispersion was probably the result of the perforated plate which was attached to the blocks of the swirler and therefore was not removable.

Hence, it was decided to compare the axial velocity of the simulation with the experiment. By extracting the values of the simulation along the centre line in the 'combustion chamber' and comparing it to the values of the experiment along the centre line in the glass tube, a comparison between CFD and PIV is possible. Figures 48 and 49 show the axial velocity along a vertical line for the for the no- and half-swirl setup. It includes the data points for the CFD simulation and the PIV experiment. As described in chapter 5.2.1 the poor dispersion of the smoke particles shortly after the outlet led to wrong or inaccurate vectors. This is also evident for the graph of the PIV experiment for both swirl setups. However, after around 2cm the data points of the graph get more stable. From that point on until around 10cm for the no-swirl and 8cm for the half-swirl setup in the 'combustion chamber', the values of the simulation and experiment are very similar. In this area the CFD and PIV show a high congruence. It is also noticeable that the velocity magnitude for the no- and half-swirl setup is not so different with only a slightly higher value for the no-swirl setup. Thereafter, the graphs differ for both swirl setups. For the no-swirl setup, the PIV graph decreases rapidly until it reaches around 1m/s at the end of position 3. The CFD simulation in comparison decreases a lot slower. Almost the same applies to the half-swirl setup. A comparison for the full-swirl setup was not reasonable due to the spurious values of the PIV experiment.

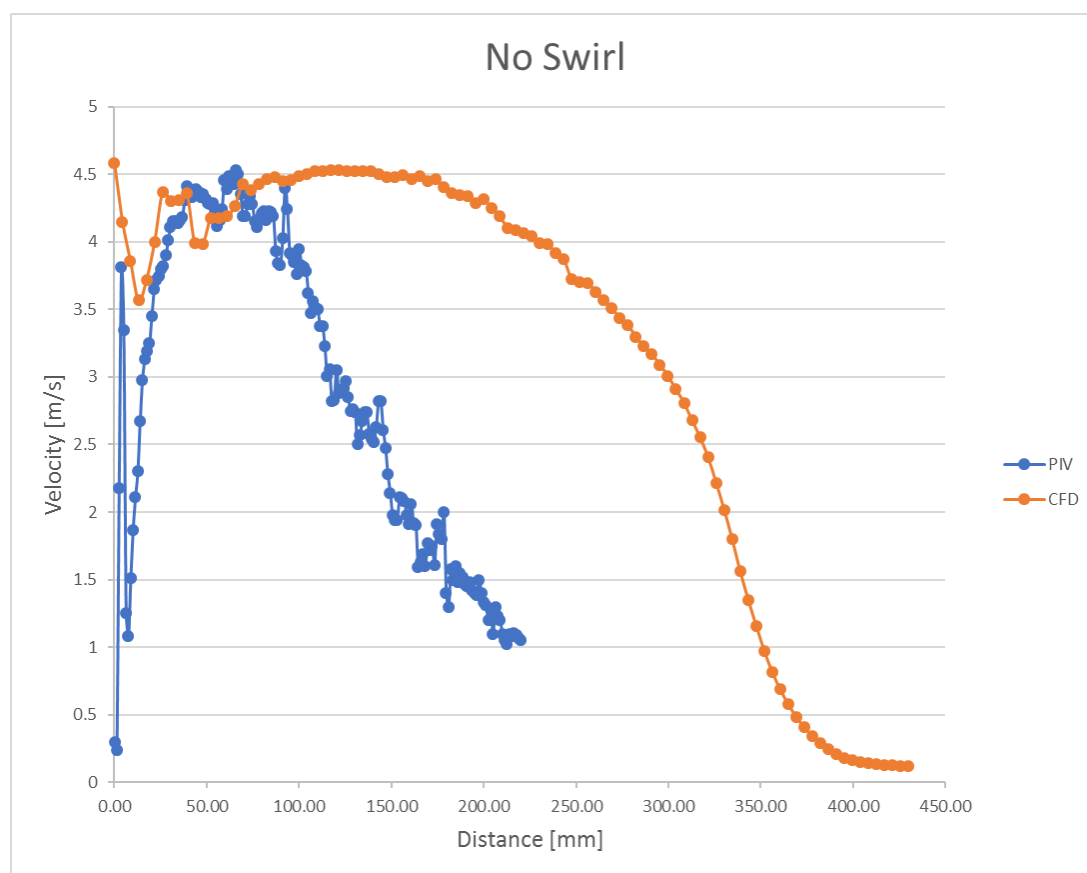


Figure 48: Comparison of CFD and PIV of the Axial Velocity for No Swirl Setup

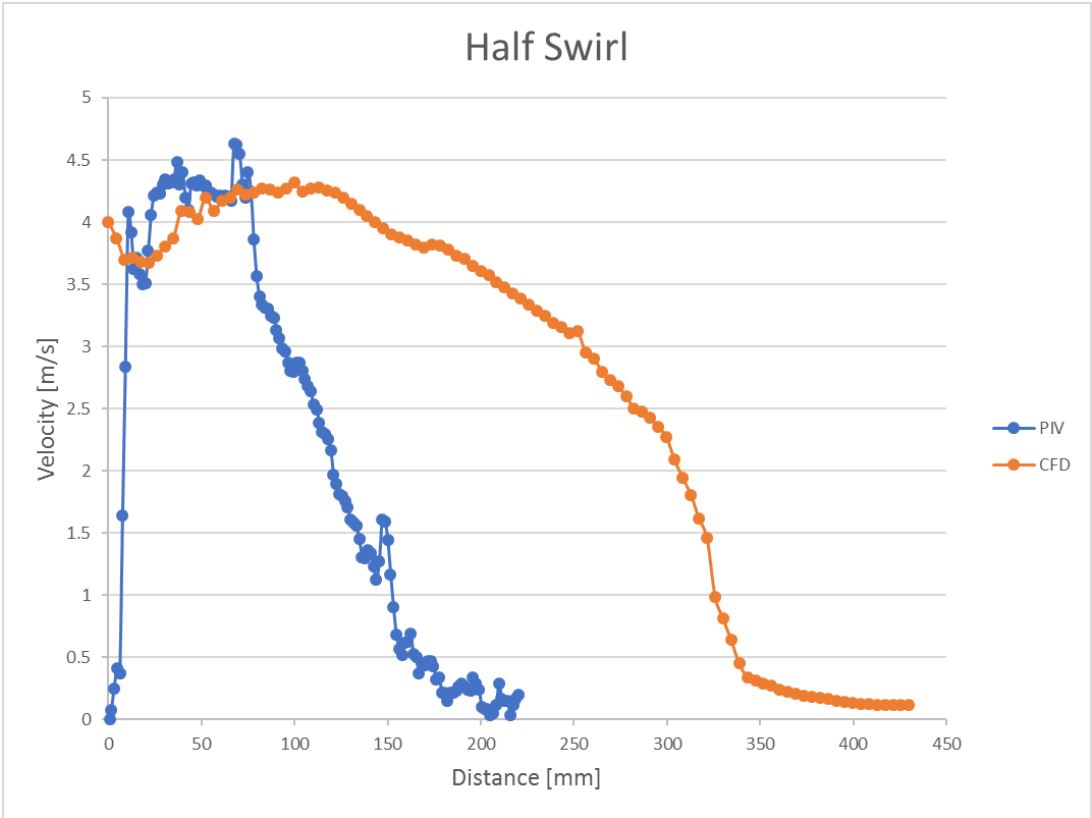


Figure 49: Comparison of CFD and PIV of the Axial Velocity for Half Swirl Setup

6 Conclusion

The objective of this thesis was to study of the influence of different burner designs on the flow field. In particular, the impact of a swirling motion caused by a swirler inlet was investigated and for this task, a PIV experiment and a CFD simulation were performed. It started with the construction and setup of the experiment and learning of the PIV technique and its components which were new in the university's laboratory. Before running the PIV experiments a validation check was performed and around 6% maximal deviation of the mean value was measured. This possible difference between each run was accepted as the components of the system reached their limits. Either a larger number of recorded images or a laser with a trigger frequency below 1000Hz would reduce the error between each run and would be recommended for further studies. For this experiment, the flow field for three different swirl settings- no-, half- and full-swirl- and four different velocity ratios were acquired. The flow rates were calculated as if biomass was burned in the 'real' burner. The resulting vector fields can be seen in chapter 5.2 which also includes the challenges faced during the runs. For each swirl-setup different issues occurred during the operation of the experiments. For the no-swirl setup, the low dispersion of the smoke particles especially shortly after the outlet posed a problem. The experiment with different particles such as titanium oxide with a seeding device would be interesting and worth an attempt. Especially as the flow field will also be examined under reaction conditions inside the burner in the upcoming stages of the project where smoke particles are ineligible and solid particles will be necessary. However, solid particles can easily agglomerate and lead to velocity lags inside the flow and therefore need special attention. For the full-swirl setup the opposite was the problem as the particles dispersed too fast. The movement inside the glass chamber turned from an axial into a radial movement which also meant that the movement was out of the plane of the laser sheet. This resulted in spurious vector velocity fields and a better understanding of particle movement for the full-swirl setup will be necessary for future work. The project plan states the prospective use of stereoscopic PIV which is two cameras recording a 2D velocity field but with three velocity components. For this method, the requirements and limitations for correct cross-correlation are even more important. In this context it has to be stated that Particle Image Velocimetry is a very challenging and complex technique with a long learning period. The particle flow field was unique for each swirl setting and each velocity ratio, therefore, it required different camera settings and acquisition techniques. In order to perfectly master and perform PIV it certainly would take more time than a treatise of a master thesis albeit this study gives a good guidance for future steps of the project as the experiments of the no- and half-swirl setup delivered reasonable and replicable resulting velocity fields for four different velocity ratios.

To validate the results of the PIV method it was decided to simulate the experiment with a CFD simulation. This was done during the downtime of the PIV setup as delays with the swirler components and the software occurred. Beyond that, it also offered a very good opportunity to compare the PIV and CFD results. The swirler assembly with the centre and outer tubes and the combustion chamber were modelled and simulated

with ANSYS - Fluent. For the turbulence model the realizable $k-\epsilon$ model was used which has a good reputation for the simulation of swirling flows with an acceptable calculation time. However, the model has its limitations and other turbulence models such as the Reynolds Stress Model (RSM) or the Large Eddy Simulation Model (LES) would deliver more accurate results. These models require a high expertise and experience in CFD simulation and the simulation time is considerably longer but may be an option for further studies. The validation of the CFD simulation was based on two methods: mesh validation and result validation. The mesh validation resulted in very good to perfect mesh elements and together with the result validation it can be confirmed that the results are based on a reasonable simulation procedure. The velocity fields show the obvious impact of the different swirl setups on the flow pattern. The axial and radial development of the flow field inside the combustion chamber are set side by side to highlight differences. The velocity fields show a strong dependence on length for the different swirl settings. In addition a comparison of the PIV and CFD results was performed where applicable. It confirmed good congruence for the distance 2-10cm after the outlet. Afterwards the velocity of the PIV experiment converged faster to lower values compared to the simulation. For further studies a CFD simulation with multiphase flows would be beneficial for a better comparison. The level of detail can be further increased by simulating flow of biomass particles or even including combustion reactions.

7 References

- [1] “Directive 2009/28/EC of the European Parliament and of the Council of 23 April 2009 on the promotion of the use of energy from renewable sources and amending and subsequently repealing Directives 2001/77/EC and 2003/30/EC”, *In OJ L140*, p. 16–62, 2009-06-05.
- [2] A. Camia, N. Robert, and J. K. et al., *Biomass production, supply, uses and flows in the European Union*. Publications Office of the European Union, 2018.
- [3] D. Lilley, “Swirl Flows in Combustion: A Review”, *AIAA Journal*, vol. 15, no. 8, pp. 1063–1078, 1977.
- [4] D. Tamburello and M. Amitay, “Active manipulation of a particle-laden jet”, *International Journal of Multiphase Flow*, vol. 34, pp. 829–851, 2008.
- [5] S. Candel, D. Durox, T. Schuller, J.-F. Bourgouin, and J. Moeck, “Dynamics of Swirling Flames”, *Annual Review of Fluid Mechanics*, vol. 46, pp. 147–173, 2014.
- [6] R. Hadeif and B. Lenze, “Measurements of droplets characteristics in a swirl-stabilized spray flame”, *Experimental Thermal and Fluid Science*, vol. 30, no. 2, pp. 117–130, 2005.
- [7] S. Leibovich, “The Structure of Vortex Breakdown”, *Annual Review of Fluid Mechanics*, vol. 10, pp. 221–246, 1978.
- [8] R. Jarpala, N. Burle, M. Voleti, and R. Sadanandan, “A Numerical Study of Swirl Effects on the Flow and Flame Dynamics in a Lean Premixed Combustor”, *International Journal of Heat and Technology*, vol. 34, no. 2, pp. 227–235, 2016.
- [9] S. Menon and R. Ranjan, “Spray combustion in swirling flow”, in *Coarse Grained Simulation and Turbulent Mixing*. Cambridge University Press, 2016, pp. 351–392.
- [10] R. Jarpala, N. Burle, M. Voleti, and R. Sadanandan, “Effect of Swirl on the Flame Dynamics and Pollutant Emissions in an Ultra-Lean Non-Premixed Model Gas Turbine Burner”, *Combustion Science and Technology*, vol. 189, no. 10, pp. 1832–1848, 2017.
- [11] M. Ishak and M. Jaafar, “The Effect of Swirl Number on Reducing Emissions from Liquid Fuel Burner System”, *Combustion Science and Technology*, no. 19, pp. 48–56, 2005.
- [12] J. Ferziger and M. Peric, *Computational Methods for Fluid Dynamics*. Springer-Verlag Berlin Heidelberg, 2002, pp. 265–300.
- [13] E. Laurien and H. Oertel, *Numerische Strömungsmechanik*. Vieweg + Teubner, Wiesbaden, 2009, pp. 25–88.
- [14] J. Ferziger and M. Peric, *Computational Methods for Fluid Dynamics*. Springer-Verlag Berlin Heidelberg, 2002, pp. 21–31.
- [15] D. Wilcox, *Turbulence Modelling for CFD*. DCW Industrie California, 1993, pp. 11–17.

- [16] M. Rieutord, *Fluid Dynamics*. Springer-Verlag Berlin Heidelberg, 2015, pp. 323–378.
- [17] ANSYS, INC., *ANSYS Fluent Theory Manual - Turbulent Flow*, ANSYS, Inc Southpointe, PA, USA, 2013, Release 15.0.
- [18] E. Laurien and H. Oertel, *Numerische Strömungsmechanik*. Vieweg + Teubner, Wiesbaden, 2009, pp. 161–186.
- [19] B. Launder and D. Spalding, “The numerical computation of turbulent flows”, *Computer Methods in Applied Mechanics and Engineering*, vol. 3, no. 2, pp. 269–289, 1974.
- [20] D. Wilcox, *Turbulence Modelling for CFD*. DCW Industrie California, 1993, pp. 73–90.
- [21] F. Marias, J. Puiggali, and M. Quintard, “Quality of CFD models for jet flow analysis for the design of burners and boilers”, *Korean Journal of Chemical Engineering*, vol. 19, no. 28, 2002.
- [22] G. K. Ntinias, X. S. Y. Wang, and G. Zhang, “Evaluation of CFD turbulence models for simulating external airflow around varied building roof with wind tunnel experiment”, *Building Simulation*, vol. 11, no. 1, pp. 115–123, 2018.
- [23] M. Raffel, C. Willert, S. Wereley, and J. Kompenhans, *Particle Image Velocimetry*. Springer-Verlag Berlin Heidelberg, 2017, pp. 15–47.
- [24] R. Zakaria and P. Bryanston-Cross, “Light scattering efficiency of oil smoke seeding droplets in PIV systems”, in *2012 Photonics Global Conference (PGC)*. IEEE, 2012.
- [25] C. Zeng, S. Vasilevskis, and B. Kozłowski, *Particle Image Velocimetry - User Guide*. University of Aalborg - Department of Civil Engineering, 2018.
- [26] W. Leuckel, *Swirl Intensities, Swirl Types and Energy Losses of Different Swirl Generating Devices: Symbols, Definition, Derivations of Formulas-figures*. International Flame Research Foundation IFRF, 1967.
- [27] N. Khaldi, Y. Chouari, H. Mhiri, and P. Bournot, “CFD investigation on the flow and combustion in a 300 MWe tangentially fired pulverized-coal furnace”, *Heat and Mass Transfer*, vol. 52, no. 9, pp. 1881–1890, 2015.
- [28] Z. Driss, B. Necib, and H.-C. Zhang, *CFD Techniques and Energy Applications*. Springer International Publishing AG, 2018, pp. 179–199.
- [29] ANSYS, INC., *ANSYS Fluent Meshing User’s Guide*. ANSYS, Inc Southpointe, PA, USA, 2013, Release 15.0.
- [30] Y. Chouari, W. Kriaa, H. Mhiri, and P. Bournot, “CFD investigation on mixing in a rapidly mixed tubular flame burner”, *Meccanica*, vol. 52, no. 15, pp. 3615–3627, 2017.
- [31] ANSYS, INC., *ANSYS Fluent Tutorial Manual*. ANSYS, Inc Southpointe, PA, USA, 2013, Release 15.0.

- [32] A. Melling, “Tracer particles and seeding for particle image velocimetry”, *Measurement Science and Technology*, vol. 8, no. 12, pp. 1406–1416, 1997.
- [33] *LDY-PIV User Manual*. Litron Lasers Ltd, 2014, pp. 15–47.
- [34] *DyanmicStudio Manual*. Dantec Dynamics A/S, 2016.

8 List of Figures

1	Characteristic flow pattern in a combustion chamber for dual swirl injector [6]	4
2	Experimental arrangement for a typical PIV system [23]	12
3	Time response of oil particles with different diameters [23]	14
4	Cross-section geometry of swirl generator	16
5	Cross-section geometry of the swirl generator	17
6	Swirl number as function of angle ξ	19
7	Flow Rate and Velocity Ratios for the Experiment	21
8	Procedure of CFD Simulation	22
9	CAD-Model	23
10	Mesh for Full-Swirl Setup	25
11	Skewness Definition	26
12	Skewness Distribution	27
13	Orthogonal Quality Definition	27
14	Orthogonal Quality Distribution	28
15	Convergence of Residuals for Full Swirl Simulation	30
16	Position of Monitor Points	31
17	Velocity over Iterations for the Monitor Points	31
18	Monitor Points for Grid Independence Study	33
19	Setup of PIV Experiment - left) view from the laser, right) view from the camera	34
20	Connection Setup of Synchronizer with Camera and Laser	35
21	SpeedSense VEO 410	36
22	Litron Laer LDY303 PIV Laser	37
23	PIV Experiment Procedure	38
24	Measure Scale Factor for Calibration of the Camera	39
25	Particle Density in the Interrogation Windows	40
26	Timing Diagram	41
27	PIV reproducibility tests with 500, 2000 and 4000 images	44
28	Velocity Fields for No, Half and Full Swirl	45
29	Velocity Profile at different Positions after the exit for No, Half and Full Swirl	46
30	Radial Velocity at different Positions after the exit for Half and Full Swirl .	48
31	Radial Velocity at different Positions after the exit for Half and Full Swirl .	49
32	Radial Velocity Distribution at different Positions after the exit for Full and Half Swirl	50
33	No Swirl Image for Ratio 3 and 1st Position	52
34	Velocity Field for No Swirl and Velocity Ratio 1	54
35	Velocity Field for No Swirl and Velocity Ratio 2	55
36	Velocity Field for No Swirl and Velocity Ratio 3	56
37	Velocity Field for No Swirl and Velocity Ratio 4	57
38	Smoke vortices for two different time points a) and b) at Position 3	58

39	Velocity Field for Half Swirl and Velocity Ratio 1	59
40	Velocity Field for Half Swirl and Velocity Ratio 2	60
41	Velocity Field for Half Swirl and Velocity Ratio 3	61
42	Velocity Field for Half Swirl and Velocity Ratio 4	62
43	Smoke particles for the Full-Swirl Setup	63
44	Velocity Field for Full Swirl and Velocity Ratio 1	64
45	Velocity Field for Full Swirl and Velocity Ratio 2	65
46	Velocity Field for Full Swirl and Velocity Ratio 3	66
47	Velocity Field for Full Swirl and Velocity Ratio 4	67
48	Comparison of CFD and PIV of the Axial Velocity for No Swirl Setup . . .	68
49	Comparison of CFD and PIV of the Axial Velocity for Half Swirl Setup . .	69

9 List of Tables

1	Angle ξ and swirl number S	19
2	Details and Sizing of the Mesh	24
3	Number of Nodes and Elements	25
4	Details and Sizing of the finer Mesh	32
5	Technical Specifications of the Camera	36
6	Settings for recording, camera and laser	41